A STUDY OF AN ASYMMETRIC CASSEGRAIN FEED SYSTEM AND ITS APPLICATIONS TO I WAVE RADIO-ASTRONOMICAL OBSER

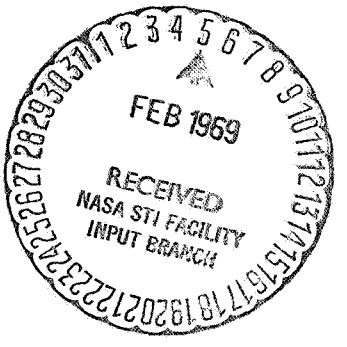

JET PROPULSION LABORATORY
CALIFORNIA INSTITUTE OF TECHNOLOGY
PASADENA, CALIFORNIA

December 1968

USCEE Report 321

UNIVERSITY OF SOUTHERN CALIFORNIA

A STUDY OF AN ASYMMETRIC CASSEGRAINIAN-ANTENNA FEED SYSTEM AND ITS APPLICATIONS TO MILLIMETER-WAVE RADIO-ASTRONOMICAL OBSERVATIONS

S. D. Slobin

Contract No. JPL 952 210

Prepared for

JET PROPULSION LABORATORY
PASADENA, CALIFORNIA

ELECTRONIC SCIENCES LABORATORY

USC Engineering

December 1968 USCEE Report 321

A STUDY OF AN ASYMMETRIC CASSEGRAINIAN-ANTENNA FEED SYSTEM AND ITS APPLICATIONS TO MILLIMETER-WAVE RADIO-ASTRONOMICAL OBSERVATIONS

S. D. Slobin

Contract No. JPL 952 210

Prepared for

JET PROPULSION LABORATORY
PASADENA, CALIFORNIA

This work was performed for the Jet Propulsion Laboratory, California Institute of Technology, sponsored by the National Aeronautics and Space Administration under Contract NAS7-100.

ACKNOWLEDGMENT

I would like to gratefully acknowledge the help of several of the many individuals who provided much needed assistance during the period of my graduate studies.

Mr. Charles Stelzried, of the Jet Propulsion Laboratory, has been the mainstay of the millimeter-wave radio-astronomy project for the past several years. He has provided invaluable assistance with regard to equipment development and procurement, data reduction and analysis, and guidance through the many stages of the experimental investigations. Miss Lois Busch of JPL carried out much of the computer analysis of the lunar eclipse and atmospheric study results. Dr. Takeshi Sato, Mr. Philip Potter, and Mr. Gerald Levy, all of JPL, gave their valuable support to the USC millimeter-wave project and participated in many pertinent discussions regarding the project. Mr. Robert Gardner of JPL and Mr. Donald Oltmans of USC assisted in radiometer and antenna development, testing, and maintenance, and also aided in several observations of lunations and lunar eclipses. The Western Data Processing Center at UCLA provided the computer facilities by which the lengthy computations of electromagnetic-wave scattering from the tilted hyperboloidal subreflector were carried out.

Dr. Zohrab A. Kaprielian, Chairman of the USC Electrical Engineering Department, and Dr. John Nodvik of the Physics Department gave their much needed support during the many years of my graduate study. Dr. Willard Van Tuyl Rusch, chairman of my guidance committee, has given most freely of his time, technical guidance, moral support, and friendship during my long association with him. It has been an illuminating and rewarding experience working with Dr. Rusch.

Finally, I would like to particularly thank my parents, whose unfailing support made it possible for me to obtain my education.

TABLE OF CONTENTS

ABSTRACT

The goals of this study are the design, analysis, and evaluation of a nodding hyperboloidal subreflector in a Cassegrainian antenna system used for radio-astronomical investigations.

A theoretical analysis of spherical electromagnetic wave scattering from a tilted hyperboloid is carried out using methods of vector diffraction theory. Theoretical expressions for the amplitude and phase of the resultant fields are given; but these expressions are of such complexity that digital computer solution using numerical integration techniques is necessary. The resultant fields in the two principal planes are compared to scattered fields in the symmetric hyperboloid case; and it is found that the patterns are similar, except for a shift of the peak in the plane of tilt. Diffraction theory results are obtained for the three cases in which the hyperboloid D/λ ratios equal 59.54 (the nodding subdish system), 24, and 10. Comparison is made with the geometrical optics reflected field for the identical geometry and feed function. The amplitudes of all cases agree to within one dB. Computation of the cross-polarized component of the scattered field indicates that the power in these fields is low compared to that in the normally polarized fields. The electric field of the cross-polarized component is at least 52-dB below the normally

polarized component.

Determination of the phase center of the scattered field is carried out using various techniques. Two of the methods depend on an accurate knowledge of the phase and amplitude of the scattered field; and the others are derived from geometry and geometrical optics considerations. In addition, a study of the caustic curves associated with the virtual rays in the asymmetric geometry is carried out utilizing the methods of differential geometry. A discussion of the advantages and disadvantages of each method is given. Plots of the phase of the scattered field on circles (in the plane of tilt) around the symmetric focus and around the best-fit phase centers are presented. A fifteen-fold decrease in phase variation around the best-fit phase center is seen, compared to the phase variation around the symmetric focus. Phase center determinations for the three cases $D/\lambda = 59.54$, 24, and 10 indicate that the best-fit phase center positions, based on diffraction theory analyses, are independent of the values of D/λ, for the small number of cases considered and $D/\lambda \geq 10$.

A complete description of the nodding subdish system is given, including the RF and electronic system used in processing received signals. A discussion of the mechanical and electronic considerations associated with this particular nodding subdish system is made; and a

discussion of low frequency switching problems in general is carried out, based upon a series of radiometer noise and gain change measurements made as a function of subdish switching frequency. A unique method of signal calibration is discussed, with primary emphasis on radio-astronomical applications.

Antenna patterns taken with the hyperboloidal subreflector in one of its off-axis positions show that grossly distorted patterns do not result due to asymmetry; although slight beam broadening in the plane normal to the plane of tilt does result.

The use of the nodding subdish system in the investigation of lunar temperature changes during a total lunar eclipse indicates that the system can be used in an operational field situation. Results of data taken during the October 18, 1967, total lunar eclipse are given.

Chapter 1

INTRODUCTION

The goals of this study are the design, analysis, and evaluation of a "nodding" hyperboloidal subreflector in a Cassegrainian antenna system used for radio-astronomical investigations.

Among the major problems plaguing radio-astronomical investigators are signal detection limitations imposed by a generally very low signal-to-noise ratio. This, combined with receiver noise and gain fluctuations, variable atmospheric attenuation, antenna pointing inaccuracies, and gain and beamwidth measurement problems, makes accurate data acquisition at all times a very difficult procedure.

Basic to most radio-astronomy systems utilizing relatively high-noise receivers at millimeter wavelengths is the use of the Dicke system of synchronous signal detection (1,2).

The Dicke system was one of the first departures from a straight total-power detection system. It utilizes a waveguide switch which enables one to receive signals alternately from the source (as seen by the antenna) and from a reference waveguide termination. The difference signal is synchronously detected; and knowledge of the reference temperature and a zero-reference point

enables one to determine the source temperature. The switching rate might be on the order of 100 cycles per second; thus, system gain changes occurring at a frequency somewhat less than the switching rate will essentially be cancelled out, particularly if the reference temperature is approximately equal to the source temperature.

A disadvantage of the Dicke system, involving a waveguide switch, is that the switch introduces an insertion loss directly into the signal line (due to the properties of the switch itself) which further reduces the magnitude of the already weak signal. Typically, the loss at a frequency of 90-GHz might be as high as one dB.

Instead of using a waveguide termination as a reference in the Dicke system, one might also use a second feedhorn looking at the "cold sky", or, in the case of a Cassegrainian antenna system, a second feedhorn illuminating the hyperboloidal subreflector, thus giving a second antenna beam looking at the "cold sky". However, in each of these cases, a waveguide switch of some kind must be used, and a signal loss is thus introduced into the system. To eliminate the waveguide switch in a synchronous detection system, one must switch the antenna beam itself, rather than any signal that is already within a waveguide. This becomes a mechanical rather than an electronic problem. In a Cassegrainian system, one beam-switching method is to tilt the hyperboloidal subreflector periodically, thus giving two different antenna beams--one of which may be used to receive signals

from a radio source and the atmosphere, and the other to receive background and atmospheric contributions from a position in the sky near the source.

The USC-JPL radio astronomy project (3-5) utilizes a Cassegrainian type antenna system, presently using a nodding hyperboloidal subreflector to attain the beam-switching mode of operation. From 1964 to 1967 the system had been a normal Cassegrainian type antenna system, utilizing a 60-inch diameter paraboloidal reflector and a 7.8-inch diameter hyperboloidal subreflector, coaxial with the paraboloid. A ferrite waveguide switch was used to switch between the source signal and a reference waveguide termination. With time, the insertion loss of the ferrite switch increased, the isolation became quite unpredictable, and system performance was degraded. It became clear that a new concept in Cassegrainian antenna systems would have to be developed.

Thus, a project to design, analyze, and evaluate a beam-switching system was initiated. This system would involve the use of a "nodding", or periodically tilting, hyperboloidal subreflector. Several other investigators had analyzed beam-switching by means of tilted subreflectors, off-axis feeds, and dual feedhorns (6-10), but none had developed a "nodding" hyperboloidal subreflector in a synchronous detection system. Also, analyses had been of a

geometrical optics nature, and no vector diffraction theory analysis of the tilted hyperboloid system had been carried out.

The nodding hyperboloidal subreflector creates an off-axis beam in each of its two tilted positions. Thus, one beam may be used to track a source such as the sun or moon, and the other may be used as the "cold sky" reference beam in the synchronous detection scheme. The same radiometer and electronic system may be used as in the normal Dicke system utilizing a waveguide switch; but in the beam switching system, no deleterious effects from the switch insertion loss are obtained.

Experimentally, there are several advantages in using a beam-switching system. Not only can one avoid the problems inherent in the use of a ferrite waveguide switch, but one can, to some extent, eliminate the effects of the atmosphere with respect to variable thermal noise contributions due to short-term (minutes) changes in water vapor content in the atmosphere. Problems associated with varying atmospheric properties have been examined by several investigators (11-15); and preliminary work indicates that the nodding subdish system may be particularly useful in future studies of atmospheric variability.

There is no way to completely eliminate the two atmospheric effects of antenna temperature contribution and source attenuation. One problem associated with atmospheric variations is that long-term

(one hour) changes in water vapor content yield unpredictable and variable source temperature measurements (5). A beam-switching system eliminates the short term scintillations and contributions of the atmosphere by a differencing method whereby the net detected signal is the difference between the signals seen in each of the two antenna beams (thus subtacting out the atmospheric temperature contribution, but not the attenuation). Problems of long-term atmospheric variation will be more nearly overcome when the properties of the atmosphere itself are accurately known during the period of an astronomical observation.

The nodding subdish system thus lends itself quite well to in-depth studies of radio-astronomical and atmospheric problems in particular. The ultimate value of the system will depend upon the degree to which refinements in the equipment, observational techniques, and data reduction methods are carried out.

Chapter 2

SCATTERING FROM A TILTED HYPERBOLOIDAL REFLECTOR

2.1 Introduction

Scattering from an asymmetric (tilted) hyperboloidal reflector has been investigated previously in the literature using the techniques of geometrical optics (7, 9). In order to obtain more accurate expressions for important diffraction effects, the problem of electromagnetic wave scattering from a tilted hyperboloid is solved in this chapter using the methods of vector diffraction theory.

2.2 Theoretical Analysis

Figure 2-1 indicates the geometry of a symmetric (untilted) Cassegrainian antenna system. Points F and Q are the two geometrical foci of the hyperboloid; point F is also the prime focus of the paraboloid. Point Q need not be at the vertex of the paraboloid; it is placed there to correspond to the source position in the nodding subdish system. The basic operation of the two-reflector antenna system can be described by geometrical optics. In the transmit mode, for example, a spherical wave emerging from Q will, upon reflection from the hyperboloid, be transformed into a wave having a spherical surface of constant phase centered at F. It appears, then, that

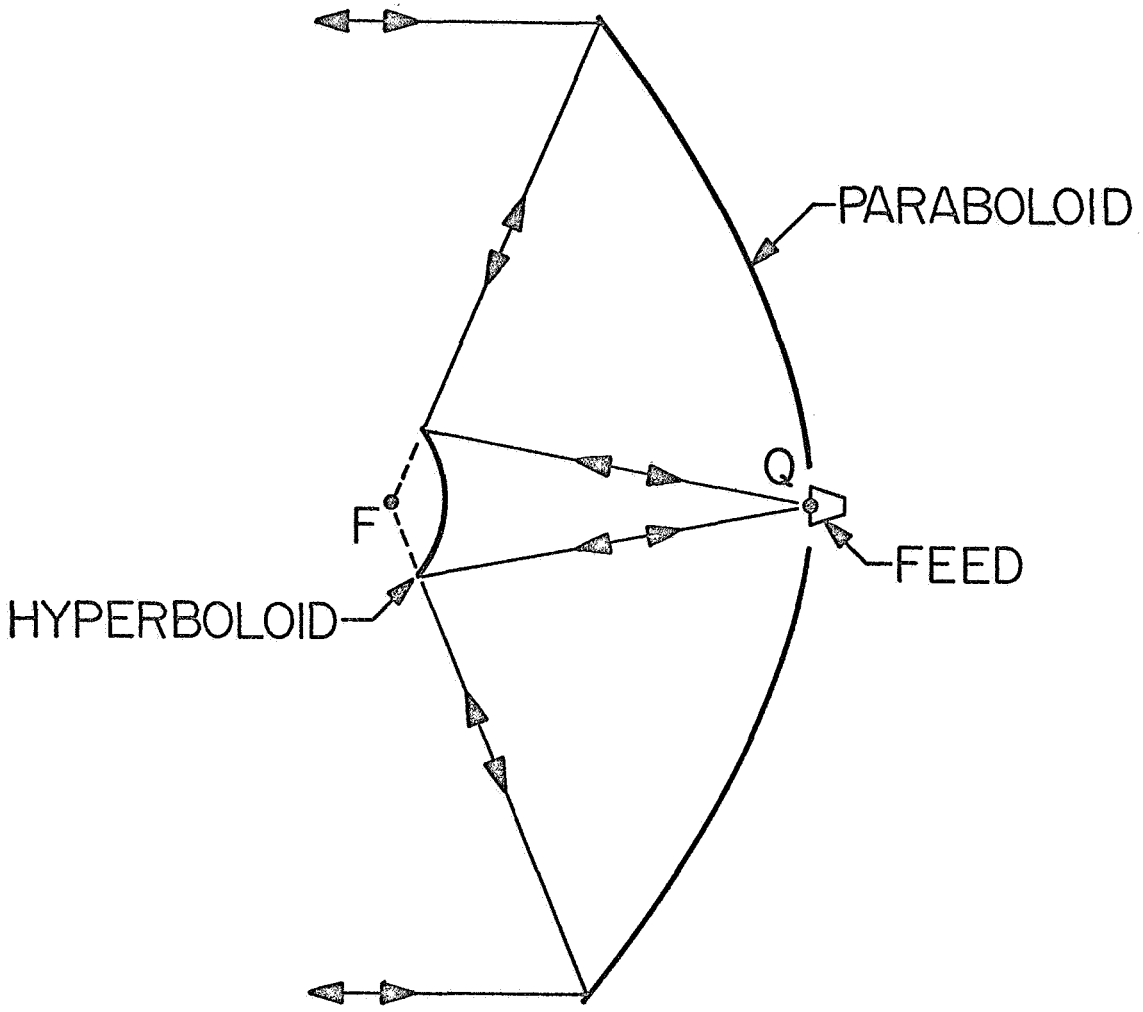

Figure 2-1. Geometry of a two-reflector Cassegrainian antenna system with a symmetrically positioned hyperboloid.

spherical waves emanate from F, the virtual focus of the hyperboloid. Upon reflection from the paraboloidal surface, spherical waves from F are transformed into plane waves propagating in a direction parallel to the axes of the hyperboloid and paraboloid. Every ray emerging from Q and undergoing reflection from the subreflector travels the same distance to any spherical surface centered at F (provided the radius of the sphere is less than $\overline{FQ}$). Thus F is the geometrical-optics phase center of the rays reflected from the hyperboloid. The receive mode reverses the above series of events.

The initial source of spherical waves at Q is not an isotropic radiator, but has a feed pattern determined by a waveguide horn structure or other type of feed system, i.e., $E_i = f(\theta,\varphi)$. A very complete vector diffraction theory study of scattering from a symmetric hyperboloid in a Cassegrainian antenna system has been carried out by Rusch (16).

Figure 2-2 indicates the geometry of the tilted hyperboloid system. Points F' and F'' are the two geometrical foci of the hyperboloid. Point F is the origin of the X_2- Z_2 coordinate system in which the scattered field is measured. The Z_2-axis is colinear with the axis of symmetry of the paraboloid. Point T represents the end view of the axis about which the hyperboloid is tilted. α is the tilt angle. The primary field emanates from Q (the origin of the X_1-Z_1

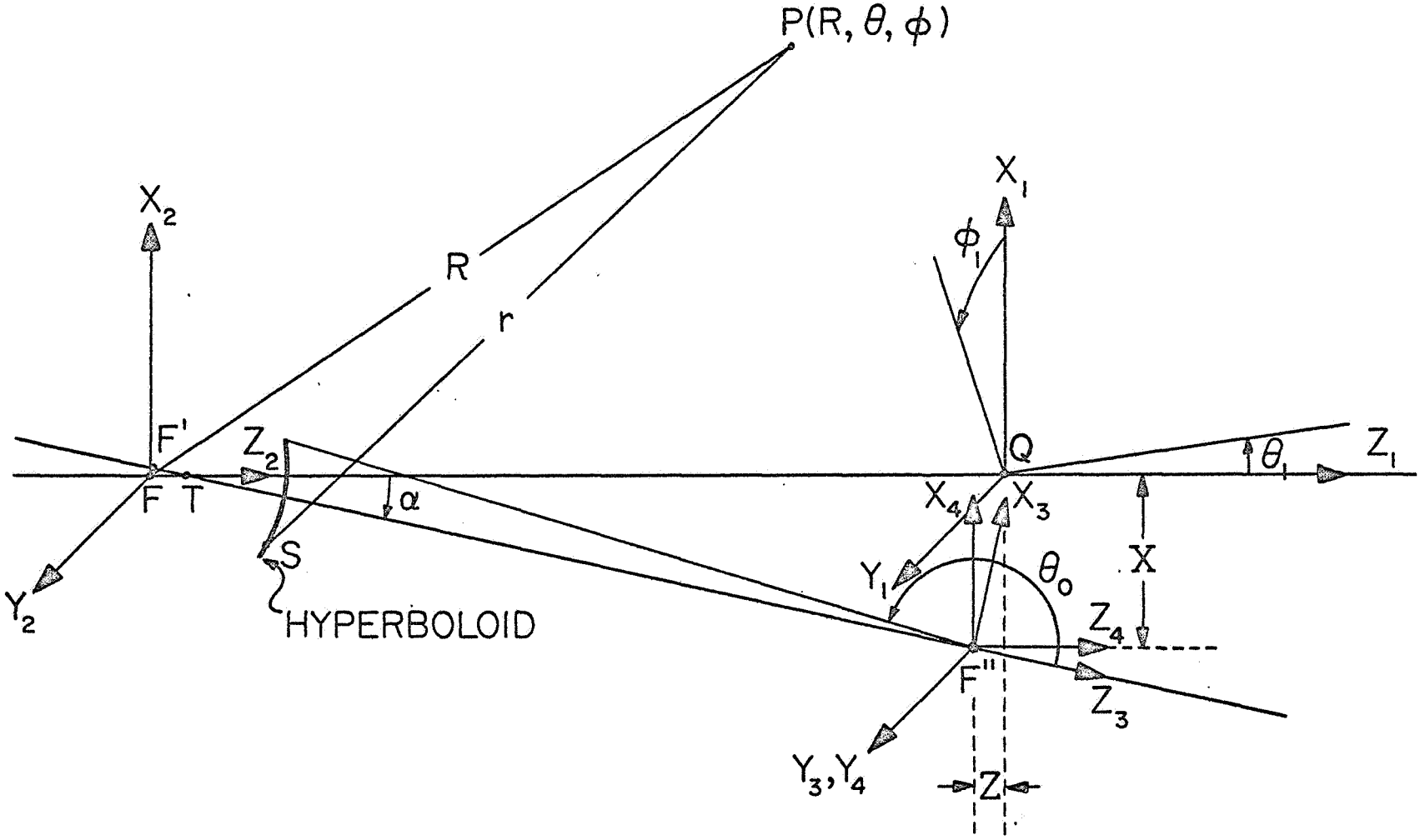

Figure 2-2.
Geometry of the tilted hyperboloid system.

system) in the form of a spherical wave and impinges on the hyperboloid.

A complete analysis of the two-reflector problem (including the paraboloidal main reflector) can be carried out by using the field scattered from the hyperboloid as the illumination on the paraboloid (17).

The analysis of scattering from the hyperboloidal surface is carried out from a general solution to the electromagnetic field equations, as in Silver (18, Chapters 3 and 5). The particular physical-optics analysis in Silver uses the angular distribution of the point-source illumination to calculate the currents induced on the hyperboloid. The currents at each point are calculated from plane-wave reflection formulas so that the method is restricted to dimensions and radii of curvature of wavefront and hyperboloid that are large relative to a wavelength. The scattered field at any point is then determined by integrating over the transverse components of the induced surface currents. This technique has achieved remarkably accurate results in the determination of the electromagnetic properties of microwave reflector antennas (16, 17). It will be initially assumed that the incident field is polarized in the plane of the tilt. Because of the symmetry of the geometry and the illumination, the scattered field will be symmetrical about the plane of tilt

and the phase center of the scattered field will lie in the plane of the tilt.

Consider the case of a region V (as indicated in Figure 2-3) which is unbounded and in which the sources (currents) of the electromagnetic field are confined to a region of finite extent. The source point is determined by the vector $\bar{\rho}(\rho, \theta, \varphi)$. O is the origin, P is the field point, and S is the source point. The source point S is not the source of incident illumination, but represents the position of currents induced by the illuminating field. As the induced currents on the reflecting surface are confined to the hyperboloid, the volume distribution of current becomes a surface distribution over this illuminated surface.

For the case of the field point P located at a large distance from both the source and the origin ($r, R \gg |\rho|$), the following approximations are valid:

$$\text{phase:} \quad r = R - \bar{\rho} \cdot \bar{R}_1$$

$$\text{amplitude:} \quad r = R$$

$$\text{unit vectors:} \quad \hat{r}_1 = \hat{R}_1$$

The scattered field intensity in the far field is (18, Equation 5.70):

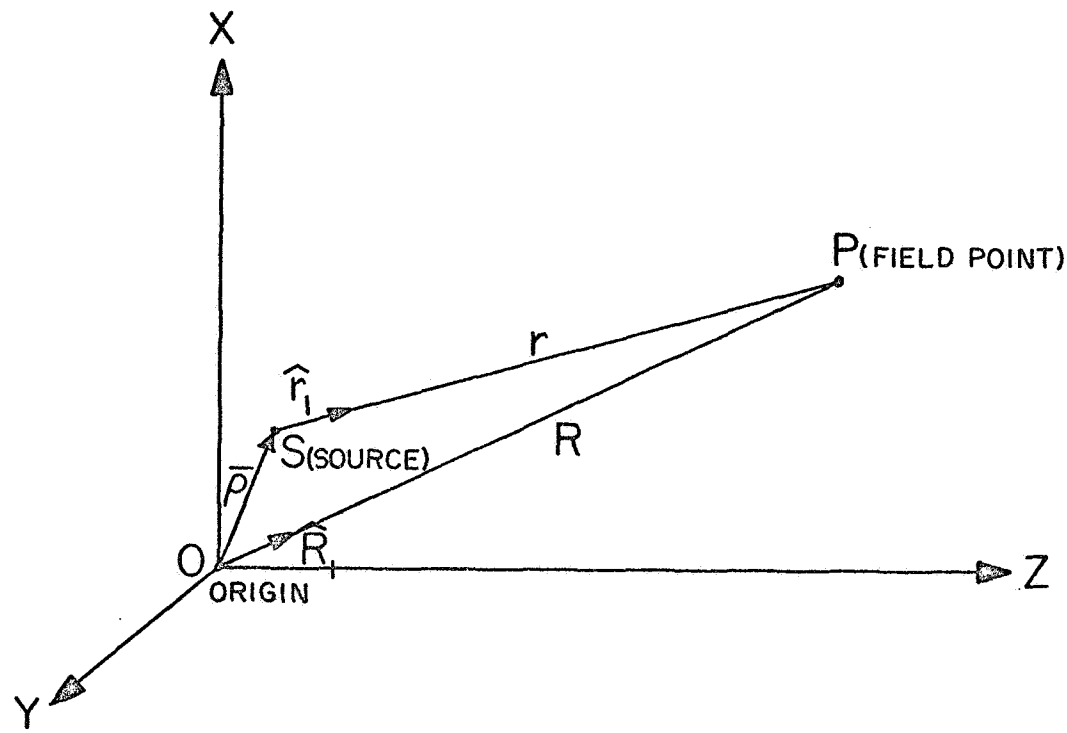

Figure 2-3. Geometry of the scattering problem relating sources of the electromagnetic field (currents), origin, and field point.

$$\bar{E}(P) = \frac{-j\omega\mu}{2\pi R} e^{-jkR} \int_S \left\{ (\hat{n}\times\bar{H}_i) - [(\hat{n}\times\bar{H}_i)\cdot\hat{R}_1]\hat{R}_1 \right\} e^{+jk\bar{\rho}\cdot\hat{R}_1} dS \quad (2\text{-}1)$$

where $(\hat{n}\times\bar{H}_i) = \bar{K}/2$ and $\bar{K}$ = induced surface current density on the hyperboloid. $\bar{H}_i$ is the incident magnetic field.

The magnetic field is given by the far-zone relationship

$$\bar{H}(P) = \sqrt{\frac{\epsilon}{\mu}} \cdot [\hat{R}_1 \times \bar{E}(P)] \quad (2\text{-}2)$$

The term $[(\hat{n}\times\bar{H}_i)\cdot\hat{R}_1]\hat{R}_1$ is the longitudinal vector component of the induced surface current in the direction of $\hat{R}_1$. Thus it can be seen that subtraction of this term from $(\hat{n}\times\bar{H}_i)$ yields fields that are always transverse to $\hat{R}_1$ in the case of the above far-field approximations.

Using different notation for the term in brackets { }, the far-zone scattered field intensity becomes

$$\bar{E}(P) = \frac{-j\omega\mu}{2\pi} \frac{e^{-jkR}}{R} \int_S \{\hat{n}\times\bar{H}_i\}_{transverse} e^{+jk\bar{\rho}\cdot\hat{R}_1} dS \quad (2\text{-}3)$$

where $\bar{H}_i$ is the incident magnetic field evaluated at the hyperboloidal reflecting surface, and $\hat{n}$ is the unit vector normal to the surface. The integration is carried out over the illuminated front of the reflector. To account for the current discontinuity between the front

and back of the reflector, a line of charge has been postulated to lie along the rim of the reflector. When the electromagnetic field approximations used in conjunction with the vector Kirchhoff equations are discontinuous and the resulting integrations are over open surfaces, it can be shown that the Kirchhoff equations intrinsically include the boundary-line charge contributions (19). The effects of this line charge are incorporated in Equation (2-3).

Following Figure 2-2 and Equation (2-3), the X_3-Z_3 coordinate system is chosen as the system in which the integration will be carried out. In this system, the hyperboloid is symmetric, and he ranges of integration are φ: 0 to 2π, and θ: θ_o to π. All vectors, distances, and feed functions contained in the integrand must be expressed in terms of the X_3-Z_3 coordinates. The X_3-Z_3 system is obtained by translating and rotating the X_1-Z_1 system. All angles φ are measured clockwise in the X-Y plane from the X-axis toward the Y-axis. All angles θ are measured from the +Z-axis.

The hyperboloid is axially symmetric in the X_3-Z_3 system. The equation for its surface in this system is

$$\rho_3 = \frac{-ep}{1 + e \cos \theta_3} \qquad (2\text{-}4)$$

where

$$p = c\left(1 - \frac{1}{e^2}\right),$$

e = eccentricity, > 1

$c = \frac{1}{2}\overline{FQ} = \frac{1}{2}\overline{F'F''}$

$\theta_o < \theta_3 < \pi$ (for the geometry shown in Figure 2-2)

In terms of rectangular coordinates, the transformations from the X_1-Z_1 system to the X_3-Z_3 system are

(1) a translation:

$$\begin{aligned} x_4 &= x_1 + X \\ y_4 &= y_1 \\ z_4 &= z_1 + Z \end{aligned} \tag{2-5}$$

and (2) a rotation

$$\begin{aligned} x_3 &= x_4 \cos\alpha + z_4 \sin\alpha \\ y_3 &= y_4 \\ z_3 &= -x_4 \sin\alpha + z_4 \cos\alpha \end{aligned} \tag{2-6}$$

Simplifying these expressions, we obtain the following sets of transformations:

(1)
$$\begin{cases} x_1 = x_3 \cos\alpha - z_3 \sin\alpha - X \\ y_1 = y_3 \\ z_1 = x_3 \sin\alpha + z_3 \cos\alpha - Z \end{cases} \tag{2-7}$$

$$(2)\quad \begin{cases} x_3 = x_1 \cos\alpha + Z_1 \sin\alpha + (X\cos\alpha + Z\sin\alpha) \\ y_3 = y_1 \\ z_3 = -x_1 \sin\alpha + Z_1 \cos\alpha - (X\sin\alpha - Z\cos\alpha) \end{cases} \tag{2-8}$$

The unit vector transformations then become:

$$(1)\quad \begin{cases} \hat{a}_{x1} = \hat{a}_{x3}\cos\alpha - \hat{a}_{z3}\sin\alpha \\ \hat{a}_{y1} = \hat{a}_{y3} \\ \hat{a}_{z1} = \hat{a}_{x3}\sin\alpha + \hat{a}_{z3}\cos\alpha \end{cases} \tag{2-9}$$

$$(2)\quad \begin{cases} \hat{a}_{x3} = \hat{a}_{x1}\cos\alpha + \hat{a}_{z1}\sin\alpha \\ \hat{a}_{y3} = \hat{a}_{y1} \\ \hat{a}_{z3} = -\hat{a}_{x1}\sin\alpha + \hat{a}_{z1}\cos\alpha \end{cases} \tag{2-10}$$

Referring to Equation (2-3) and Figures 2-2 and 2-3 we may identify

$$\begin{aligned} \bar{\rho} &= \rho_2 \hat{a}_{\rho 2} \quad &&\text{(in the } X_2\text{-}Z_2 \text{ system where} \\ \bar{R}_1 &= \hat{a}_R \quad &&\text{we measure the scattered field at a point } P(R,\theta,\varphi)) \end{aligned} \tag{2-11}$$

$$\hat{a}_{\rho 2} = \hat{a}_{x2}\sin\theta_2\cos\varphi_2 + \hat{a}_{y2}\sin\theta_2\sin\varphi_2 + \hat{a}_{z2}\cos\theta_2$$

$$\hat{a}_R = \hat{a}_{x2}\sin\theta\cos\varphi + \hat{a}_{y2}\sin\theta\sin\varphi + \hat{a}_{z2}\cos\theta \tag{2-12}$$

Thus, in Equation (2-3),

$$\bar{\rho} \cdot \hat{R}_1 = \rho_2 \hat{a}_{\rho 2} \cdot \hat{a}_R$$

$$= \rho_2 [\sin\theta \sin\theta_2 \cos(\varphi - \varphi_2) + \cos\theta \cos\theta_2] \qquad (2\text{-}13)$$

Equation (2-3) becomes

$$\bar{E}(P) = \frac{-j\omega\mu}{2\pi} \frac{e^{-jkR}}{R} \int_S \{\hat{n} \times \bar{H}_i\}_{\text{transverse}} e^{+jk\rho_2[\sin\theta \sin\theta_2 \cos(\varphi-\varphi_2) + \cos\theta\cos\theta_2]} dS \qquad (2\text{-}14)$$

Now consider the factor $\{\hat{n} \times \bar{H}_i\}_{\text{transverse}}$. Since we are considering a non-symmetric geometry, the orientation of the incident field $\bar{H}_i$ is extremely important.

Two major cases to consider are $E_i \parallel X_1 - Z_1$ plane and $\bar{E}_i \perp X_1 - Z_1$ plane. Consider the analysis for the first case, $\bar{E}_i$ in the $X_1 - Z_1$ plane (plane of tilt of the hyperboloid). The results for the second case ($E_i \perp X_1 - Z_1$ plane) will be given later.

In conventional vector notation,

$$\bar{E}_i = A(\theta_1) \frac{e^{-jk\rho_1}}{\rho_1} \left[-\cos\varphi_1 \hat{a}_{\theta 1} - \sin\varphi_1 \hat{a}_{\varphi 1}\right] \qquad (2\text{-}15)$$

where $A(\theta_1)$ is the feed horn pattern, which is regarded as a function of θ_1 only (i.e., no variation of feed horn pattern as a function of φ_1).

The incident magnetic field is then:

$$\bar{H}_i = \sqrt{\frac{\varepsilon}{\mu}}\ \hat{a}_{\rho 1} \times \bar{E}_i$$

$$= \sqrt{\frac{\varepsilon}{\mu}}\ A(\theta_1)\ \frac{e^{-jk\rho_1}}{\rho_1}\left[\sin\varphi_1\ \hat{a}_{\theta 1} - \cos\varphi_1\ \hat{a}_{\varphi 1}\right] \qquad (2\text{-}16)$$

These incident fields are centered at Q, the origin of the X_1-Z_1 system.

For calculation of the cross-product $(\hat{n} \times \bar{H}_i)$, the incident field and the normal must be expressed in rectangular coordinates, as the unit vectors in a spherical coordinate system are not constant but vary as a function of position.

$$\hat{a}_{\varphi 1} = -\hat{a}_{x1} \sin\varphi_1 + \hat{a}_{y1} \cos\varphi_1$$

$$\hat{a}_{\theta 1} = \hat{a}_{x1} \cos\theta_1 \cos\varphi_1 + \hat{a}_{y1} \cos\theta_1 \sin\varphi_1 - \hat{a}_{z1} \sin\theta_1 \qquad (2\text{-}17)$$

Thus, in a rectangular coordinate system,

$$\bar{E}_i = A(\theta_1)\ \frac{e^{-jk\rho_1}}{\rho_1}\left[\hat{a}_{x1}(\sin^2\varphi_1 - \cos^2\varphi_1 \cos\theta_1) + \hat{a}_{y1}(1+\cos\theta_1)\cdot\right.$$

$$\left.\cdot(-\sin\varphi_1\cos\varphi_1) + \hat{a}_{z1}(\sin\theta_1\cos\varphi_1)\right]$$

$$\bar{H}_i = \sqrt{\frac{\varepsilon}{\mu}}\ A(\theta_1)\ \frac{e^{-jk\rho_1}}{\rho_1}\left[\hat{a}_{x1}(1+\cos\theta_1)\sin\varphi_1\cos\varphi_1 + \hat{a}_{y1}(\cos\theta_1\cdot\right.$$

$$\left.\cdot\sin^2\varphi_1 - \cos^2\varphi) + \hat{a}_{z1}(-\sin\theta_1\sin\varphi_1)\right]$$

(2-18)

For an hyperboloidal surface described by

$$\rho_3 = \frac{-ep}{1 + e \cos \theta_3} \quad , \tag{2-19}$$

the normal to this surface in the $X_3 - Z_3$ coordinate system is

$$\hat{n}_1 = \frac{(1 + e \cos \theta_3)\, \hat{a}_{\rho 3} - (e \sin \theta_3)\, \hat{a}_{\theta 3}}{m(\theta_3)} \tag{2-20}$$

where

$$m(\theta_3) = \left[(1 + e \cos \theta_3)^2 + (e \sin \theta_3)^2 \right]^{1/2}$$

$\hat{n}_1$ is a vector away from the origin of the $X_3 - Z_3$ coordinate system. For computation of $(\hat{n} \times \hat{H}_i)$, we require the normal <u>toward</u> the $X_3 - Z_3$ system, which is $\hat{n}_2 = -\hat{n}_1$.

Utilizing the following coordinate transformation expressions

$$\begin{aligned} \hat{a}_{\rho 3} &= \hat{a}_{x3} \sin \theta_3 \cos \varphi_3 + \hat{a}_{y3} \sin \theta_3 \sin \varphi_3 + \hat{a}_{z3} \cos \theta_3 \\ \hat{a}_{\theta 3} &= \hat{a}_{x3} \cos \theta_3 \cos \varphi_3 + \hat{a}_{y3} \cos \theta_3 \sin \varphi_3 - \hat{a}_{z3} \sin \theta_3 \end{aligned} \tag{2-21}$$

and Equations (2-10), the outward normal $\hat{n}_2$ becomes (in the $X_1 - Z_1$ coordinate system):

$$\hat{n}_2 = \frac{-1}{m(\theta_3)}\Big[\hat{a}_{x1}(\cos\alpha \sin\theta_3 \cos\varphi_3 - \sin\alpha\cos\theta_3 - e\sin\alpha) +$$

$$+\hat{a}_{y1}(\sin\theta_3 \sin\varphi_3) +$$

$$+\hat{a}_{z1}(\sin\alpha \sin\theta_3 \cos\varphi_3 + \cos\alpha\{e + \cos\theta_3\})\Big] \quad (2\text{-}22)$$

This may be rewritten as

$$\hat{n}_2 = \left(\frac{-1}{m(\theta_3)}\right)\Big[C(\theta_3,\varphi_3)\hat{a}_{x1} + D(\theta_3,\varphi_3)\hat{a}_{y1} + E(\theta_3,\varphi_3)\hat{a}_{z1}\Big] \quad (2\text{-}23)$$

where

$$C(\theta_3,\varphi_3) = \cos\alpha(\sin\theta_3\cos\varphi_3) - \sin\alpha(e + \cos\theta_3)$$

$$D(\theta_3,\varphi_3) = \sin\theta_3 \sin\varphi_3$$

$$E(\theta_3,\varphi_3) = \sin\alpha(\sin\theta_3\cos\varphi_3) + \cos\alpha(e + \cos\theta_3)$$

The incident magnetic field $\bar{H}_i$ is rewritten as

$$\bar{H}_i = \sqrt{\frac{\epsilon}{\mu}}\, A(\theta_1)\frac{e^{-jk\rho_1}}{\rho_1}\Big[F(\theta_1,\varphi_1)\hat{a}_{x1} + G(\theta_1,\varphi_1)\hat{a}_{y1} + H(\theta_1,\varphi_1)\hat{a}_{z1}\Big] \quad (2\text{-}24)$$

where

$$F(\theta_1,\varphi_1) = (1 + \cos\theta_1)\sin\varphi_1\cos\varphi_1$$

$$G(\theta_1,\varphi_1) = \cos\theta_1 \sin^2\varphi_1 - \cos^2\varphi_1$$

$$H(\theta_1,\varphi_1) = -\sin\theta_1 \sin\varphi_1$$

The surface current density $(\hat{n}_2 \times \bar{H}_i)$ becomes

$$(\hat{n}_2 \times \bar{H}_i) = \left[\frac{-1}{m(\theta_3)}\sqrt{\frac{\epsilon}{\mu}}\, A(\theta_1)\, \frac{e^{-jk\rho_1}}{\rho_1}\right] \cdot \left[(DH-EG)\hat{a}_{x1} + (EF-CH)\hat{a}_{y1} + (CG-DF)\hat{a}_{z1}\right] \qquad (2\text{-}25)$$

The transverse components of $(\hat{n}_2 \times \bar{H}_i)$ must be determined. Since the scattered field is measured in the X_2- Z_2 system, the spherical coordinate unit vectors transverse to R can be expressed in terms of the rectangular unit vectors:

$$\hat{a}_\theta = \hat{a}_{x2} \cos\theta \cos\varphi + \hat{a}_{y2} \cos\theta \sin\varphi - \hat{a}_{z2} \sin\theta$$

$$\hat{a}_\varphi = -\hat{a}_{x2} \sin\varphi + \hat{a}_{y2} \cos\varphi \qquad (2.26)$$

The transverse components of $(\hat{n}_2 \times \bar{H}_i)$ become

$$(\hat{n}_2 \times \bar{H}_i)_{transverse} = \left[(\hat{n}_2 \times \bar{H}_i)\cdot(\hat{a}_\theta)\right]\hat{a}_\theta + \left[(\hat{n}_2 \times \bar{H}_i)\cdot(\hat{a}_\varphi)\right]\hat{a}_\varphi$$

$$= \left[\hat{n}_2 \times \bar{H}_i\right]_\theta \hat{a}_\theta + \left[\hat{n}_2 \times \bar{H}_i\right]_\varphi \hat{a}_\varphi \qquad (2.27)$$

where

$$\left[\hat{n}_2 \times \bar{H}_i\right]_\theta = \left[\frac{-1}{m(\theta_3)}\sqrt{\frac{\epsilon}{\mu}}\, A(\theta_1)\, \frac{e^{-jk\rho_1}}{\rho_1}\right] \cdot \left[(DH-EG)\cos\theta\cos\varphi + (EF-CH)\cos\theta\sin\varphi + (CG-DF)(-\sin\theta)\right]$$

$$= \left[\frac{-1}{m(\theta_3)}\sqrt{\frac{\epsilon}{\mu}}\, A(\theta_1)\, \frac{e^{-jk\rho_1}}{\rho_1}\right] \cdot \left[M(\theta_1, \varphi_1, \theta_3, \varphi_3, \theta, \varphi\right]$$

and,

$$\left[\hat{n}_2 \times \bar{H}_i\right]_{\varphi} = \left[\frac{-1}{m(\theta_3)}\sqrt{\frac{\epsilon}{\mu}}\, A(\theta_1)\, \frac{e^{-jk\rho_1}}{\rho_1}\right] \cdot \left[(DH-EG)(-\sin\varphi) + (EF-CH)(\cos\varphi)\right]$$

$$= \left[\frac{-1}{m(\theta_3)}\sqrt{\frac{\epsilon}{\mu}}\, A(\theta_1)\, \frac{e^{-jk\rho_1}}{\rho_1}\right] \cdot \left[N(\theta_1,\varphi_1,\theta_3,\varphi_3,\theta,\varphi)\right]$$

Thus,

$$(\hat{n}_2 \times \bar{H}_i)_{\text{transverse}} = \left[\frac{-1}{m(\theta_3)}\sqrt{\frac{\epsilon}{\mu}}\, A(\theta_1)\, \frac{e^{-jk\rho_1}}{\rho_1}\right] \cdot \left[M\hat{a}_{\theta} + N\hat{a}_{\varphi}\right] \qquad (2\text{-}28)$$

The differential surface element dS on the surface of the hyperboloid is calculated as seen from F'', the origin of the X_3 - Z_3 coordinate system. Figure 2-2 indicates the geometry of the situation. dS is the actual infinitesimal surface area, not the projection on a plane normal to $\hat{a}_{\rho 3}$.

$$dS = \frac{\rho_3^2 \sin\theta_3\, d\theta_3\, d\varphi_3}{(\hat{n}_1 \cdot \hat{a}_{\rho 3})} \qquad (2\text{-}29)$$

Utilizing expressions for $\hat{n}_1$ and ρ_3, this becomes:

$$dS = \frac{\rho_3(-eP)}{(1 + e\cos\theta_3)^2} \cdot m(\theta_3) \sin\theta_3\, d\theta_3\, d\varphi_3 \qquad (2\text{-}30)$$

Combining all computed factors of Equation (2-3) we obtain

$$\bar{E}(P) = \frac{-j\omega\mu}{2\pi}\,\frac{e^{-jkR}}{R}\int_S \left[\frac{-1}{m(\theta_3)}\sqrt{\frac{\epsilon}{\mu}}\,A(\theta_1)\,\frac{e^{-jk\rho_1}}{\rho_1}\right]\left[M\,\hat{a}_\theta + N\,\hat{a}_\varphi\right]\cdot$$

$$\cdot e^{+jk\rho_2[\sin\theta\sin\theta_2\cos(\varphi-\varphi_2)+\cos\theta\cos\theta_2]}\cdot$$

$$\cdot\frac{\rho_3(-ep)}{(1+e\cos\theta_3)^2}\,m(\theta_3)\sin\theta_3\,d\theta_3\,d\varphi_3 \qquad (2\text{-}31)$$

Rewriting, with $\omega\mu\sqrt{\frac{\epsilon}{\mu}} = k$,

$$\bar{E}(P) = E_\theta(P)\,\hat{a}_\theta + E_\varphi(P)\,\hat{a}_\varphi \qquad (2\text{-}32)$$

where

$$E_\theta(P) = \frac{-j(kep)}{2\pi}\,\frac{e^{-jkR}}{R}\int_{\theta_o}^{\pi}\frac{\sin\theta_3}{(1+e\cos\theta_3)^2}\left\{\int_o^{2\pi}\frac{\rho_3}{\rho_1}\,A(\theta_1)M(\theta_3,\varphi_3)\cdot\right.$$

$$\left.\cdot\, e^{-jk\rho_1}\cdot e^{jk\rho_2[K]}\,d\varphi_3\right\}d\theta_3$$

$$E_\varphi(P) = \frac{-j(kep)}{2\pi}\,\frac{e^{-jkR}}{R}\int_{\theta_o}^{\pi}\frac{\sin\theta_3}{(1+e\cos\theta_3)^2}\left\{\int_o^{2\pi}\frac{\rho_3}{\rho_1}\,A(\theta_1)N(\theta_3,\varphi_3)\cdot\right.$$

$$\left.\cdot\, e^{-jk\rho_1}\cdot e^{jk\rho_2[K]}\,d\varphi_3\right\}d\theta_3$$

and

$$[K] = [\sin\theta \sin\theta_2 \cos(\varphi-\varphi_2) + \cos\theta \cos\theta_2]$$

$$M(\theta_3,\varphi_3) = (DH-EG)\cos\theta\cos\varphi + (EF-CH)\cos\theta\sin\varphi + (CG-DF)(-\sin\theta)$$

$$N(\theta_3,\varphi_3) = (DH-EG)(-\sin\varphi) + (EF-CH)(\cos\varphi)$$

$$C = \cos\alpha(\sin\theta_3\cos\varphi_3) - \sin\alpha(e+\cos\theta_3)$$

$$D = \sin\theta_3\sin\varphi_3$$

$$E = \sin\alpha(\sin\theta_3\cos\varphi_3) + \cos\alpha(e+\cos\theta_3)$$

$$F = (1+\cos\theta_1)\sin\varphi_1\cos\varphi_1$$

$$G = \cos\theta_1\sin^2\varphi_1 - \cos^2\varphi_1$$

$$H = -\sin\theta_1\sin\varphi_1$$

For the second case of incident illumination, where $\bar{H}_i$ is in the X_1-Z_1 plane (plane of tilt of the hyperboloid) an entirely parallel analysis may be carried out.

The incident fields are written as

$$\bar{E}_i = B(\theta_1)\frac{e^{-jk\rho_1}}{\rho_1}\left(-\sin\varphi_1\,\hat{a}_{\theta 1} + \cos\varphi_1\,\hat{a}_{\varphi 1}\right)$$

and

$$\bar{H}_i = \sqrt{\frac{\epsilon}{\mu}}\,\hat{a}_{\rho 1} \times \bar{E}_i = \sqrt{\frac{\epsilon}{\mu}}\,B(\theta_1)\frac{e^{-jk\rho_1}}{\rho_1}\left(-\sin\varphi_1\,\hat{a}_{\varphi 1} - \cos\varphi_1\,\hat{a}_{\theta 1}\right) \qquad (2\text{-}33)$$

The scattered electric field at the field point P is then (for

$\bar{H}_i$ in the X_1-Z_1 plane):

$$\bar{E}(P) = E_\theta(P)\,\hat{a}_\theta + E_\varphi(P)\,\hat{a}_\varphi \tag{2-34}$$

where

$$E_\theta(P) \quad \frac{-jkep}{2\pi}\,\frac{e^{-jkR}}{R}\int_{\theta_o}^{\pi}\frac{\sin\theta_3}{(1+e\cos\theta_3)^2}\left\{\int_o^{2\pi}\frac{\rho_3}{\rho_1}\,B(\theta_1)M'(\theta_3,\varphi_3)\,e^{-jk\rho_1}\cdot\right.$$

$$\left.\cdot\, e^{jk\rho_2[K]}\,d\varphi_3\right\}d\theta_3$$

$$E_\varphi(P) = \frac{-jkep}{2\pi}\,\frac{e^{-jkR}}{R}\int_{\theta_o}^{\pi}\frac{\sin\theta_3}{(1+e\cos\theta_3)^2}\left\{\int_o^{2\pi}\frac{\rho_3}{\rho_1}\,B(\theta_1)N'(\theta_3,\varphi_3)\,e^{-jk\rho_1}\cdot\right.$$

$$\left.\cdot\, e^{jk\rho_2[K]}\,d\varphi_3\right\}d\theta_3$$

and

$$[K] = [\sin\theta\sin\theta_2\cos(\varphi-\varphi_2) + \cos\theta\cos\theta_2]$$

$$M'(\theta_3,\varphi_3) = (DH'-EG')\cos\theta\cos\varphi + (EF'-CH')\cos\theta\sin\varphi + (CG'-DF')\cdot$$
$$\cdot(-\sin\theta)$$

$$N'(\theta_3,\varphi_3) = (DH'-EG')(-\sin\varphi) + (EF'-CH')(\cos\varphi)$$

$$C = \cos\alpha(\sin\theta_3\cos\varphi_3) - \sin\alpha(e+\cos\theta_3)$$

$$D = \sin\theta_3\sin\varphi_3$$

$$E = \sin\alpha(\sin\theta_3\cos\varphi_3) + \cos\alpha(e+\cos\theta_3)$$

$$F' = \sin^2\varphi_1 - (\cos\theta_1)(\cos^2\varphi_1)$$

$$G' = -(1 + \cos\theta_1)\sin\varphi_1\cos\varphi_1$$

$$H' = \cos\varphi_1 \sin\theta_1$$

Equations (2-32) may be initially analyzed to determine several things about their character. In the $\varphi = 0$ plane, no φ component of the scattered field is expected since the incident wave is polarized in the $X_1 - Z_1$ plane, i.e., the $\varphi = 0$ plane. This is true for the untilted case also. All elements of the E_φ equation may be checked for evenness or oddness as a function of φ_3, and it is found that $N(\theta_3,\varphi_3) = -N(\theta_3, 2\pi - \varphi_3)$, i.e., N is an odd function of φ_3 for $\varphi = 0$. The exponents of the E_φ equation are even. Hence, the entire integrand of the φ_3 integral, $I_{\varphi_3}(\varphi_3)$ is such that $I(\varphi_3) = -I(2\pi - \varphi_3)$. Therefore, the φ_3 integration from 0 to π is exactly cancelled by the integration from π to 2π, and $E_\varphi = 0$ when $\varphi = 0$.

Similarly, consider the plane $\varphi = \pi/2$, where in the untilted case one finds that $E_\theta = 0$. From previously, everything other than $M(\theta_3,\varphi_3)$ is even, and $M(\theta_3,\varphi_3)$ must be tested for evenness or oddness as a function of φ_3. It is found that $M(\theta_3,\varphi_3)$ is even and this term does not integrate to zero over the φ_3 range of integration. If the tilt angle α goes to zero, it is found that the E_θ integral goes to zero for the axially symmetric case ($\alpha = 0$). Therefore, E_θ in the $\varphi = \pi/2$ plane is the cross-polarized component of the scattered field for the asymmetric geometry.

Examination of the expressions for $E_\theta(P)$ and $E_\varphi(P)$ (Equations 2-32) show that in the given form, variables in several coordinate systems are used. Thus, specifications for computer transformations of coordinate systems must be made to carry out the integration in the X_3-Z_3 coordinate system. Evaluation of the expressions for $E_\theta(P)$ and $E_\varphi(P)$ is carried out using a Simpson's Rule method of numerical integration. The field of integration, defined by the limits of integration, is divided into rings, each of which is $\Delta\theta_3$ wide, and segments of the ring, each of which is $\Delta\varphi_3$ in length. The integrand (I_n) is evaluated at each of the very small regions $\Delta\theta_3\Delta\varphi_3$. The value of the integral for each ring is calculated using the following rule:

$$I = \frac{\Delta\varphi_3}{3}\left[I_1 + 4I_2 + 2I_3 + \ldots + 2I_{N-2} + 4I_{N-1} + I_N\right] \qquad (2\text{-}35)$$

where N is the total number of φ_3 segments. As the contributions from the rings are added up, moving from $\theta = \theta_o$ to $\theta = \pi$, the number of segments of length $\Delta\varphi_3$ is reduced, until at the center of the hyperboloid, only four segments remain.

Specifying a particular value of θ_3 and φ_3 allows one to calculate all the elements of Equations (2-32) by the following rules:

(1) $$k\rho_1 = \sqrt{(kx_1)^2 + (ky_1)^2 + (kz_1)^2}$$

where $$kx_1 = kx_3 \cos\alpha - kz_3 \sin\alpha - kX$$

$$ky_1 = ky_3$$

$$kz_1 = kx_3 \sin\alpha + kz_3 \cos\alpha - kZ$$

and $$kx_3 = k\rho_3 \sin\theta_3 \cos\varphi_3$$

$$ky_3 = k\rho_3 \sin\theta_3 \sin\varphi_3$$

$$kz_3 = k\rho_3 \cos\theta_3$$

$$k\rho_3 = \frac{-kep}{1 + e\cos\theta_3}$$

(2) $$\theta_1 = \pi - \arctan\left\{\frac{[(kx_1)^2 + (ky_1)^2]^{\frac{1}{2}}}{|kz_1|}\right\}$$

(3) $$\varphi_1 = \arccos\left\{\frac{kx_1}{[(kx_1)^2 + (ky_1)^2]^{\frac{1}{2}}}\right\},$$

with specifications made for sign conventions and quadrant location.

(4) $$k\rho_2 = \sqrt{(kx_2)^2 + (ky_2)^2 + (kz_2)^2}$$

where $$kx_2 = kx_3 \cos\alpha - kz_3 \sin\alpha - kX$$

$$ky_2 = ky_3$$

$$kz_2 = kx_3 \sin\alpha + kz_3 \cos\alpha - kZ - k\overline{OF}$$

(5) $$\theta_2 = \arctan\left\{\frac{[(kx_2)^2 + (ky_2)^2]^{\frac{1}{2}}}{|kz_2|}\right\}$$

(6) $$\varphi_2 = \varphi_1$$

(7) $A(\theta_1)$ is given as an input function

(8) $M(\theta_3,\varphi_3)$ and $N(\theta_3,\varphi_3)$ are given in Equations (2-32)

A complete description of the computer program utilized in solving Equations (2-32) is given in Appendix A.

2.3 The Feed Function

The primary source feed function, $A(\theta_1)$, is given by the following expression from Love (20) for a diagonal feedhorn:

$$A(\theta_1) = \frac{\sin\left(\frac{\pi d}{\lambda\sqrt{2}}\sin\theta_1\right)\cos\left(\frac{\pi d}{\lambda\sqrt{2}}\sin\theta_1\right)}{\left(\frac{\pi d}{\lambda\sqrt{2}}\sin\theta_1\right)\left(1-\frac{2d^2}{\lambda^2}\sin^2\theta_1\right)} \qquad (2\text{-}36)$$

where d = side dimension of diagonal horn aperture

λ = free space wavelength

θ_1 = angle measured in the X_1-Z_1 system

Feedhorn pattern measurements show that this theoretical expression is experimentally correct. The 3-dB beamwidth of the horn pattern was measured to be 9.5°. A 13-dB illumination taper was measured at the edges of the illuminated hyperboloid (angular diameter is 19°).

2.4 Diffraction Theory Results

For the tilted hyperboloid system (with $\overline{E}_i$ in the X_1-Z_1 plane and a tilt angle of 2.06^o) a series of computer computations based on numerical integration of Equations (2-32) was undertaken. Diffraction theory results were obtained for the three cases in which D/λ = 59.54 (the nodding subdish system), 24, and 10. Figure 2-4 shows schematically the geometry and geometrical values upon which the computations are based. A computer listing of the complete FORTRAN IV computational program, including subroutines for calculating the phase of the scattered field and calculating the feed horn pattern is shown in Appendix A. A page of sample computer output, with pertinent results, is shown in Figure 2-5. Since each set of computations required a great deal of computer time (approximately 1.3 minutes for each field point, using an IBM 360/75 digital computer), the calculations were broken up into groups of about eighteen field points to limit computer time to less than one-half hour for each set.

Figure 2-6 shows the computed results for the field scattered from the tilted hyperboloid in the nodding subdish system (D/λ = 59.54). Both the normally polarized and cross-polarized components of the scattered field are indicated. The cross-polarized component is at least 52-dB below the normally polarized component. It can be

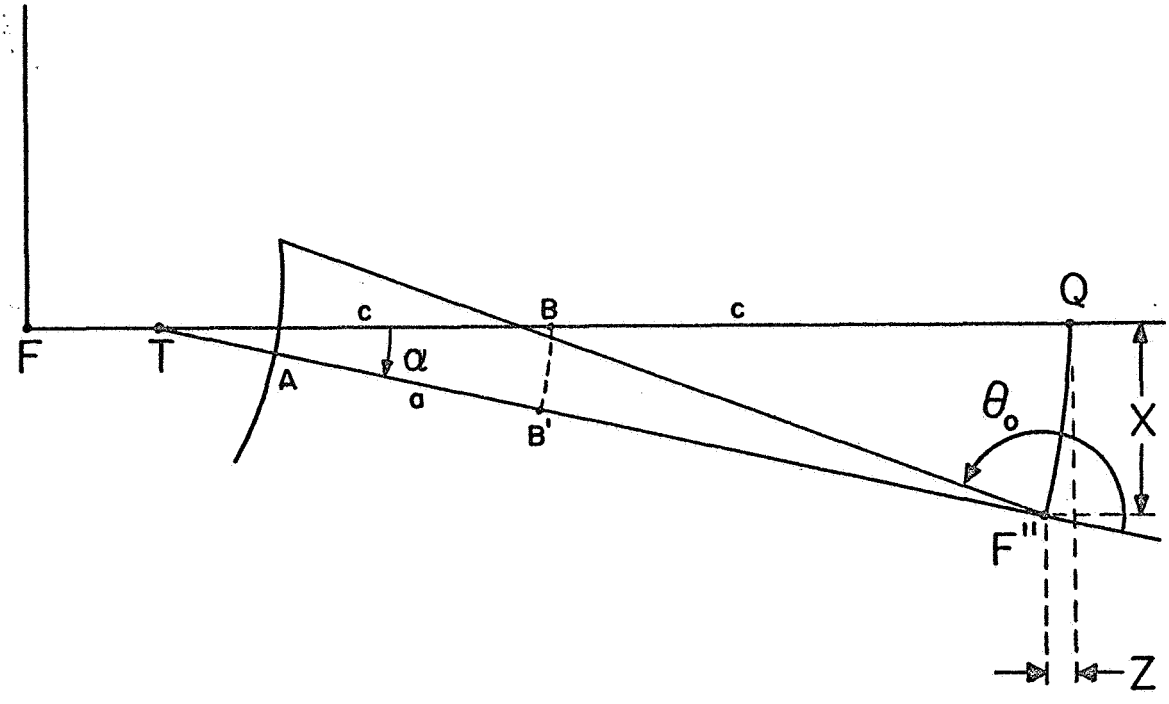

Radius of hyperboloid = 3.900" (99.06mm)
Distance between foci = FQ = 2c = 25.600" (650.24mm)
a = AB' = 9.63107" (244.63mm)
c = FB = BQ = 12.800" (325.12mm)
e = c/a = 1.32903
TA = 0.600" (15.24mm)
FA (untilted) = c-a = 3.16893" (80.49mm)
depth of hyperboloid = 0.981" (24.92mm)
$\alpha = 2.06^{o}$
X = 0.82762" (21.02mm)
Z = 0.01488" (0.38mm)
$\theta_o = 170.54^{o}$
$k = 2\pi/\lambda = 1886.26022 \text{ meter}^{-1}$ (for $D/\lambda = 59.54$)
$f = 90.0 \times 10^{9}$ Hz (for $D/\lambda = 59.54$)
Q = symmetric focus, source position
F" = tilted focus
F = paraboloid prime focus

Figure 2-4. Schematic view of geometry and geometrical values.

ALPHA = 2.06 90 GC FORTRAN 4 COMPLETE RUN TILTED HYPER

INPUT PARAMETERS AND CONTROL CONSTANTS

THETA= 1.00000 DEGREES INCREMENT= 2.00000
PHI= 180.00000 DEGREES INCREMENT= 180.00000

THETA(J)= 173.53999 KEP = 353.60693 E = 1.32903 ALPHA = 2.06000
<X = 39.65221 <Z = 0.71282 KOF = 1226.52539

OUTER INTEGRAL STEP= 0.00129 RADIANS = 0.07391 DEGREES

PHI= 3.14159 RADIANS= 179.99994 DEGREES

THETA	E THETA				E PHI			
DEGREES	REAL	IMAGINARY	MAGNITUDE	PHASE	REAL	IMAGINARY	MAGNITUDE	PHASE
1.000	-0.00197988	0.00133791	0.00238954	145.951	-0.00000000	0.00000000	0.00000000	141.234
3.000	-0.00120721	0.00191923	0.00226733	122.170	-0.00000000	0.00000000	0.00000000	133.489
5.000	-0.00052201	0.00238776	0.00244418	102.332	-0.00000000	0.00000000	0.00000000	143.583
7.000	0.00011976	0.00237876	0.00238714	85.199	0.00000000	0.00000000	0.00000000	82.440
9.000	0.00070162	0.00210458	0.00234824	63.668	-0.00000000	0.00000000	0.00000000	100.628
11.000	0.00117000	0.00163680	0.00236470	43.803	0.00000000	0.00000000	0.00000000	71.294
13.000	0.00151601	0.00102863	0.00259966	25.382	0.00000000	0.00000000	0.00000000	35.780
15.000	0.00233972	0.00028931	0.00240717	6.903	0.00000000	-0.00000000	0.00000000	350.350
17.000	0.00236260	-0.00051155	0.00241754	347.784	0.00000000	0.00000000	0.00000000	8.515
19.000	0.00203103	-0.00133604	0.00243107	326.662	0.00000000	-0.00000000	0.00000000	315.686
21.000	0.00137970	-0.00197617	0.00241179	304.894	0.00000000	-0.00000000	0.00000000	288.596
23.000	0.00053225	-0.00225615	0.00231808	283.274	0.00000000	-0.00000000	0.00000000	280.621
25.000	-0.00020320	-0.00220124	0.00221060	264.726	0.00000000	-0.00000000	0.00000000	284.290
27.000	-0.00088106	-0.00202701	0.00219866	247.210	-0.00000000	-0.00000000	0.00000000	252.977
29.000	-0.00152240	-0.00162732	0.00222842	226.938	-0.00000000	-0.00000000	0.00000000	206.643
31.000	-0.00189039	-0.00093947	0.00211096	206.426	-0.00000000	-0.00000000	0.00000000	208.081
33.000	-0.00204414	-0.00033213	0.00207095	189.229	-0.00000000	-0.00000000	0.00000000	181.410
35.000	-0.00203331	0.00045011	0.00208254	167.518	-0.00000000	0.00000000	0.00000000	147.993

IHC217I

TRACEBACK FOLLOWS- ROUTINE ISN REG. 14

IBCOM 82006300

MAIN 00005FA8

ENTRY POINT= 00000820

Figure 2-5. Sample computer output, tilted hyperboloid scattering.

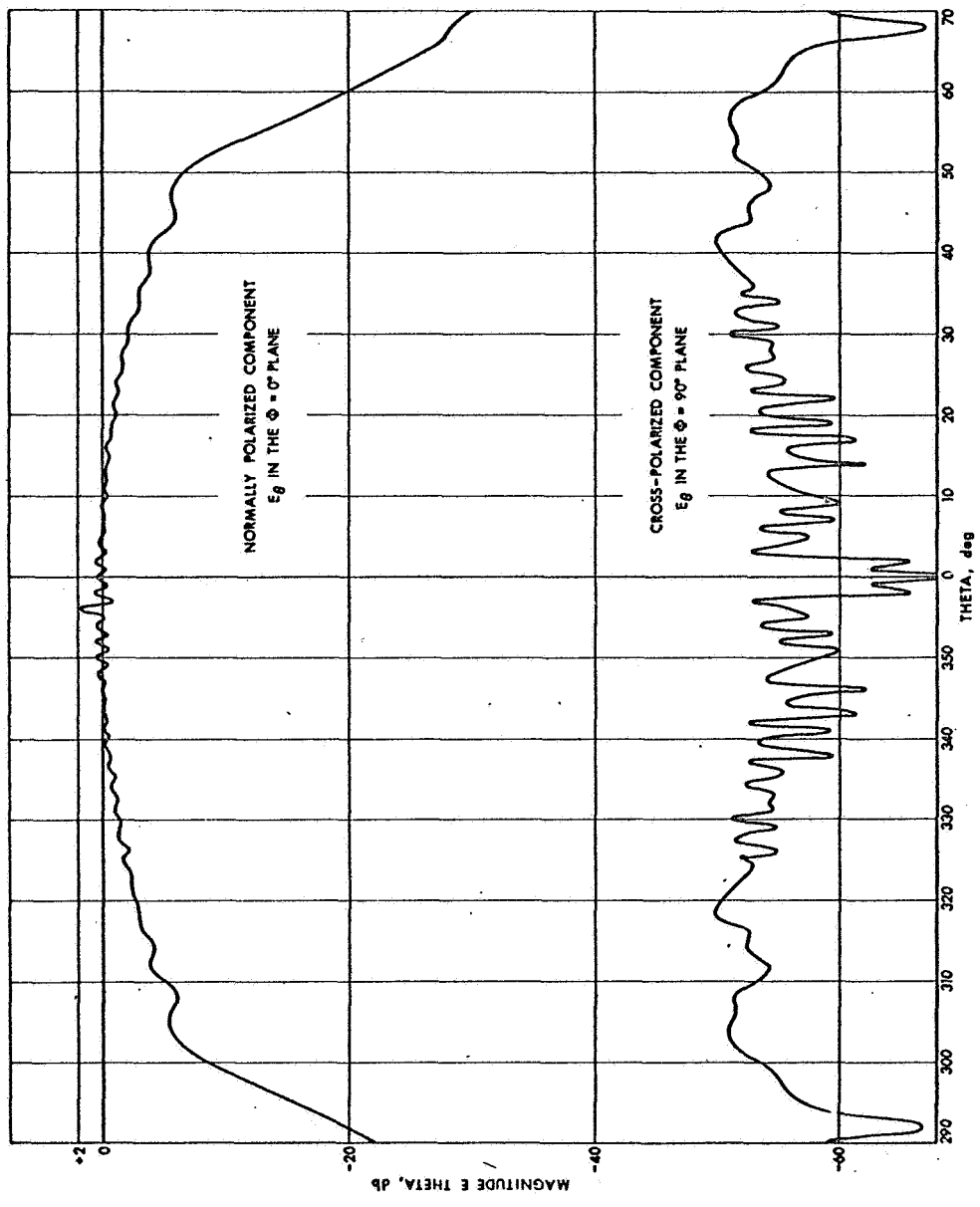

Figure 2-6. Normal and cross-polarized components of the field scattered from the tilted hyperboloid ($D/\lambda = 59.54$).

seen from the figure that the scattered field retains its symmetrical characteristic, although it is displaced approximately 4^{o} from its symmetric position. This corresponds to the optical situation in which the deviation of a reflected light beam is twice the angular movement of the mirror. Figure 2-7 shows diffraction theory scattering results for the three cases $D/\lambda = 59.54$, 24, and 10.

2.5 Geometrical Optics Field

In addition to the diffraction theory results shown in Figure 2-7, the geometrical optics field is also plotted for the identical geometry and feed function. The geometrical optics field is determined following the method given in Silver (18, p. 114). The magnitude of the field amplitude $|E_p|$ at a distance p along the reflected ray from a given point on the reflector is given as

$$|E_p| = |E_r| \cdot \left| \frac{R_1 R_2}{(R_1 + p)(R_2 + p)} \right|^{\frac{1}{2}} \qquad (2\text{-}37)$$

where $|E_r|$ = magnitude of the field amplitude at the point of reflection

R_1, R_2 = principal radii of curvature of the reflected wavefront at the point of reflection

p = distance along the reflected ray from a given point on the reflector

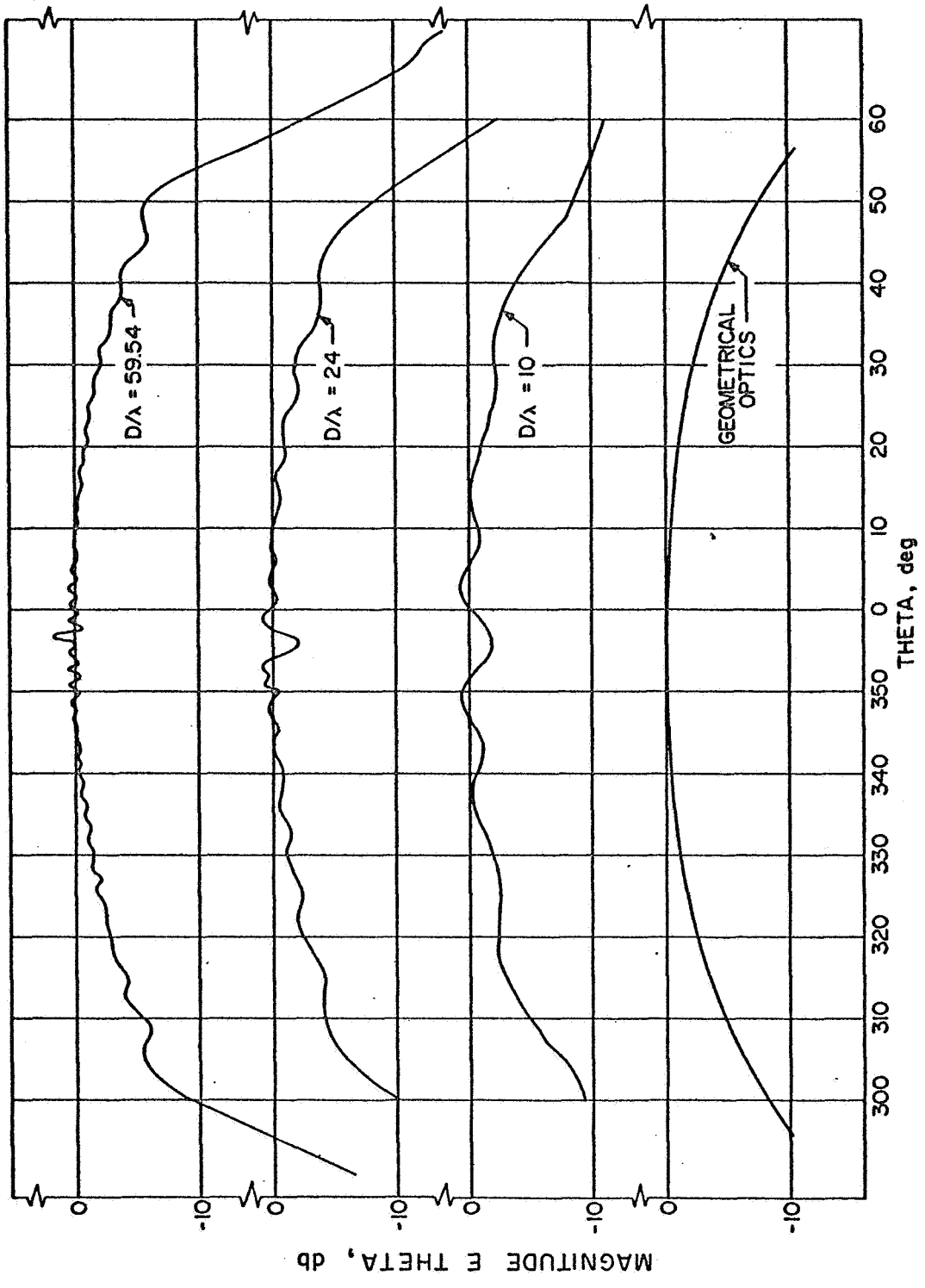

Figure 2-7. Diffraction theory and geometrical optics fields, tilted hyperboloid.

$(R_1+p), (R_2+p)$ = principal radii of curvature of the reflected wavefront at the field point

For distances far from the hyperboloid, where $p \gg R_1$ and R_2, Equation (2-37) reduces to

$$|E_p| = |E_r| \cdot \frac{|R_1 R_2|^{\frac{1}{2}}}{p} \tag{2-38}$$

It will be shown in Chapter 3 (caustic determination based on geometrical optics) that R_1 and R_2 are the radii of curvature of the virtual rays at the point of reflection (hyperboloid surface) since the caustic curves are the loci of intersections and phase centers of the virtual rays. R_1 and R_2 are computed in Section 3.3.1 for many reflected rays in the asymmetric system.

The magnitude of the field amplitude at the point of reflection ($|E_r|$) is the product of the feedhorn pattern $A(\theta_1)$ and a space-taper function, since the hyperboloid surface is not a constant distance from the source Q. If 1/QS is the space-taper function (where QS is the distance between the source Q and a point S on the hyperboloid surface, calculated by the method Section 3.3.1), the geometrical optics field becomes

$$|E_p| = A(\theta_1) \cdot (1/QS) \cdot (R_1 R_2)^{\frac{1}{2}} \cdot (\text{scaling constant}) \tag{2-39}$$

The geometrical optics field $|E_p|$ [cf. Equation (2-39) and Appendix C, page 179], is plotted in Figure 2-7. It may be seen that the amplitudes of the three diffraction theory cases and the geometrical optics case agree very well.

Chapter 3

DETERMINATION OF THE PHASE CENTER OF THE SCATTERED FIELD

3.1 Introduction

This chapter deals with various methods for finding the phase center of the electromagnetic field scattered from a tilted hyperboloidal subreflector in a Cassegrainian antenna system. With suitable alterations to the concepts presented here, the methods given are applicable to nontilted subreflectors with off-axis point-source feeds. Both geometrical optics and diffraction theory (physical optics) analyses are used in the phase center determinations. The diffraction theory methods depend on an accurate knowledge of the phase and amplitude of the scattered field, and are based upon the previously given scattering analysis (cf. Chapter 2). The geometrical optics methods require only a knowledge of the geometry of the problem and the nature of the incident fields. A discussion of the advantages, disadvantages, and accuracy of each method will also be given.

All calculations of the phase center position are carried out for the nodding subdish system in particular with a hyperboloid diameter of 7.9 inches (198.12 mm), a hyperboloid tilt angle of

2.06^{o}, $\lambda = 3.33$ mm, and $D/\lambda = 59.54$. In addition, phase center determinations for the identical geometry with $D/\lambda = 24$ and 10 are also carried out. Calculations may be easily extended to other specific geometries and wavelengths as well; however, the results presented are not universal and should be generalized for use in other systems only with care.

3.2 Introductory Concepts and Geometry.

3.2.1 Symmetric Geometry

Figure 3-1 shows the geometry of the symmetric (untilted) hyperboloid used in a Cassegrainian antenna system. The axis of symmetry of the hyperboloid is colinear with the axis of symmetry of the paraboloid. Both the point-source Q and the virtual focus of the hyperboloid F are on this axis. Q and F are the geometrical foci of the hyperboloid. The virtual focus of the hyperboloid is identical with the prime focus of the paraboloid. It should be noted that for the nodding subdish system in particular the source Q is placed at the vertex of the paraboloid (as shown in Figure 3-1). For a general Cassegrainian antenna system the source and subdish may be placed anywhere along the symmetric axis (between Q and F), subject only to basic geometrical constraints concerning subdish curvature and feedhorn and subdish blockage (6, 21).

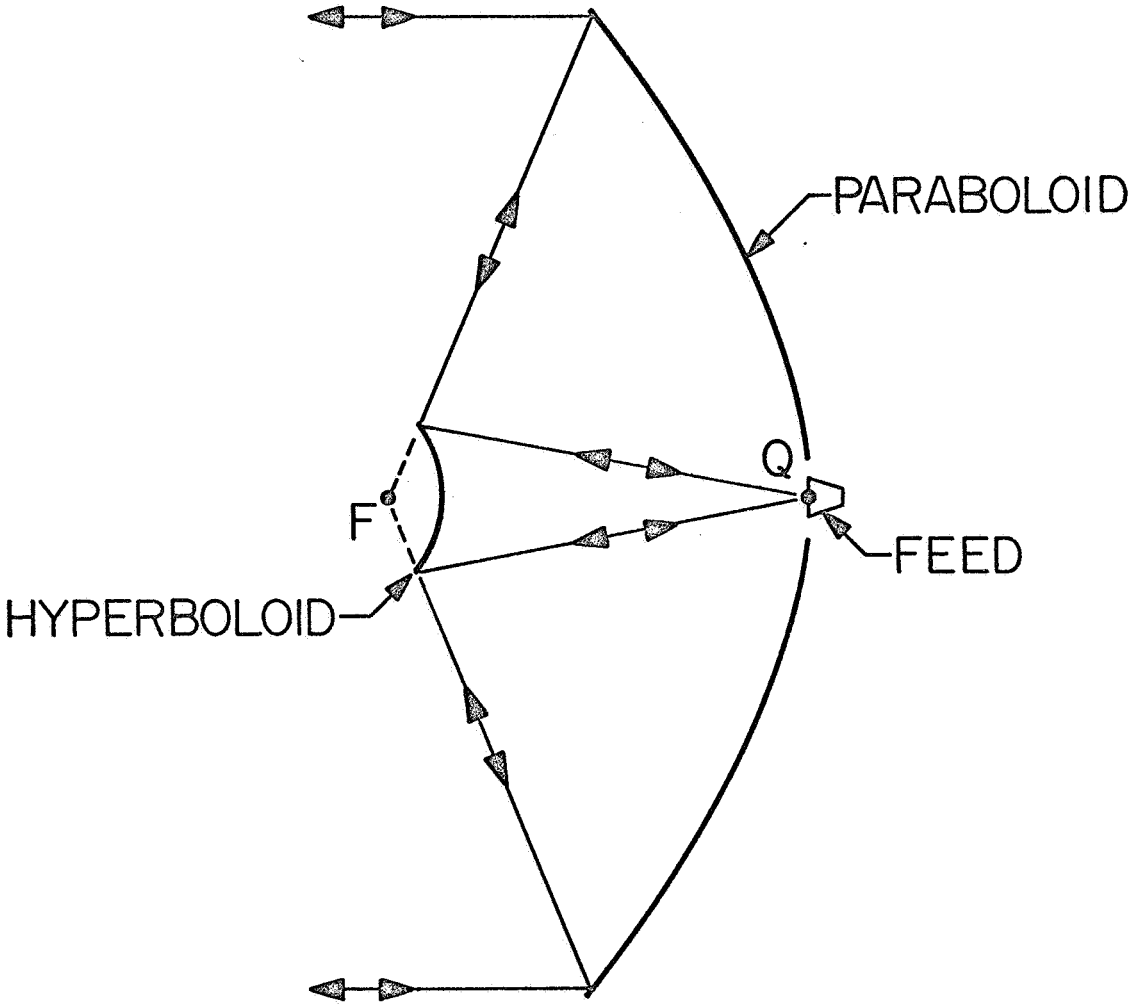

Figure 3-1. Geometry of a two-reflector Cassegrainian antenna system with a symmetrically positioned hyperboloid.

As discussed in Chapter 2, spherical waves emerging from Q will, upon reflection from the hyperboloid, be transformed into waves having spherical wavefronts of nearly constant phase centered at F. Thus, it appears that spherical waves emanate from F, the symmetric focus of the hyperboloid. A geometrical-optics analysis based upon the law of equal path length of reflected rays indicates that the focus F of the hyperboloid is the phase center of the reflected rays in the system indicated in Figure 3-1. All rays which emanate from Q and are reflected from the hyperboloid travel the same distance to any spherical surface centered at F.

A diffraction theory analysis of the symmetric phase center position has been carried out by Rusch (22), and results of that study indicate that the virtual focus of the hyperboloid is also the best-fit phase center (within 1/20 wavelength) of the scattered field in the symmetric case for diameters as small as 10 wavelengths. Experimental data confirm these results. For the range of wavelengths over which the assumptions of physical optics are valid, it is felt that a diffraction-theory analysis of the asymmetric phase center position will give accurate results also. In general, this will cover the range $D/\lambda \geq 10$. For smaller D/λ, the physical-optics assumptions that the diameter and radius of curvature of the reflecting surface are much greater than a wavelength are no longer valid.

However, experimental data indicate that the far-field diffraction theory results may be quite accurate in this range also.

3.2.2 Asymmetric Geometry

Figure 3-2 indicates the geometry of the asymmetric (tilted) hyperboloid system. The hyperboloid is tilted downward 2.06° so that the source Q is no longer located on the hyperboloid axis F'F". The virtual rays do not meet at a point such as F in the nontilted geometry. There is no specific geometrically exact point of intersection of the virtual rays. There is, rather, an envelope of points known as a "caustic", or focal surface, which indicates the "intersections" of all the virtual rays.

A more detailed view of the geometrical quantities may be seen in Figure 3-3. The hyperboloid is shown tilted with respect to the symmetric axis FQ. The axis of rotation is T, perpendicular to the plane of tilt of the hyperboloid (plane of the paper). Point F represents the position of the hyperboloid focus in the untilted situation. The source Q remains unchanged from its position in the symmetric case. The geometrical foci of the tilted hyperboloid are at the points F' and F". Neither the geometrical focus F' nor the symmetric focus F may be regarded as the phase center of the scattered field for the tilted geometry. Three virtual rays are

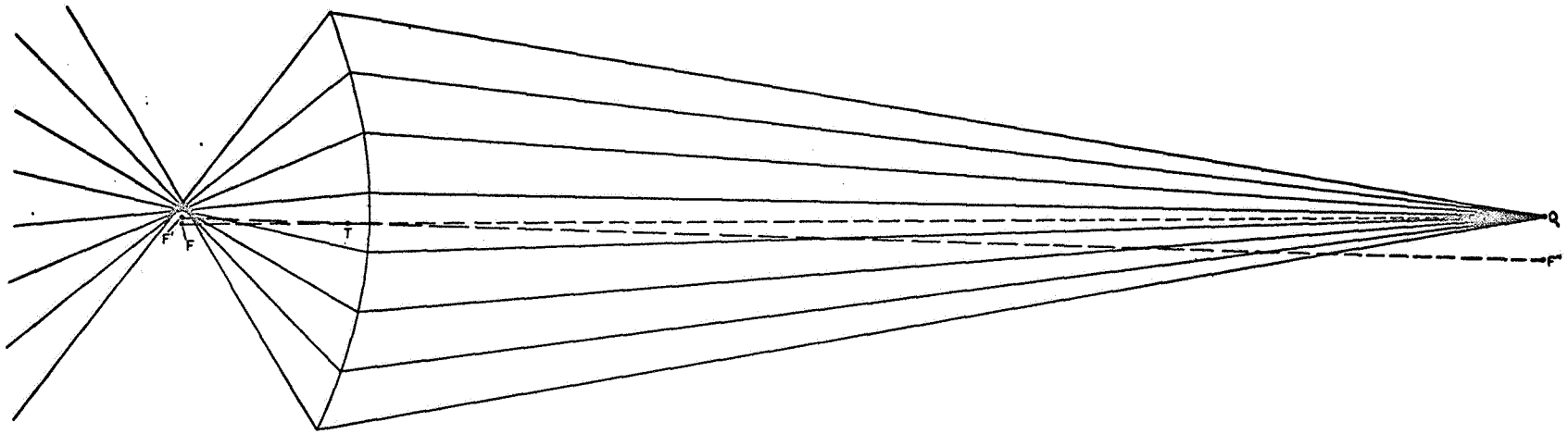

Figure 3-2. Geometry of an asymmetric Cassegrainian antenna system. The axis of symmetry of the hyperboloid is $\overline{F'F''}$. The axis of symmetry of the paraboloid is $\overline{FQ}$.

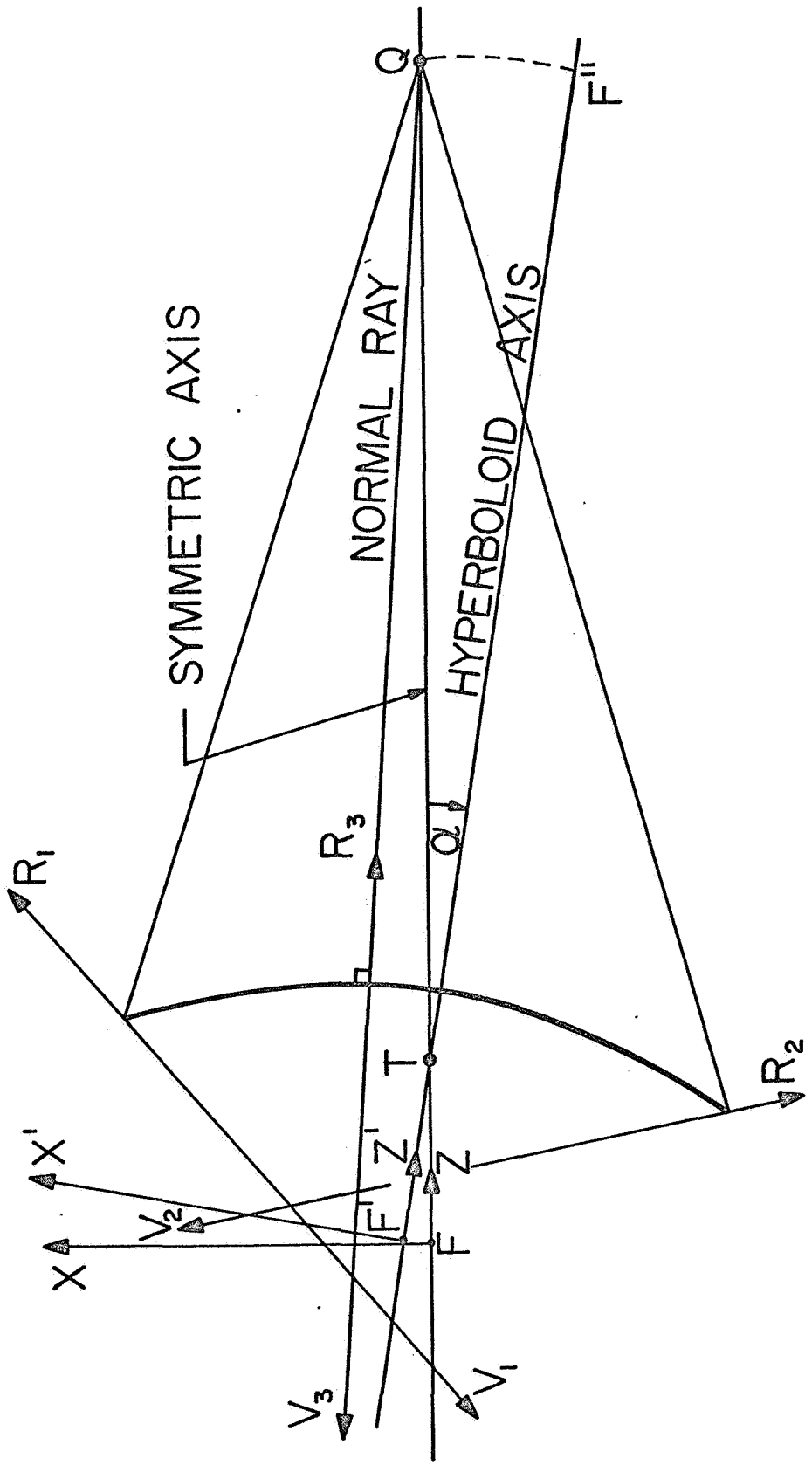

Figure 3-3. Detailed view of the asymmetric geometry.

indicated as V_1, V_2, and V_3.

3.3 Methods of Phase Center Determination

3.3.1 Caustic Curve Determination Based on Geometrical Optics

Analyses of ray tracings (such as Figure 3-2) and the discussion by Holt (23) indicate that the caustic, or focal surface, in the region of the symmetric focus is an approximate position of the asymmetric phase center. In particular, the central portion of the caustic curve might be regarded (to a first approximation) as the position of the phase center of the scattered field.

It can be shown (cf. Appendix B), by a simple geometrical analysis, that both the intersection and the phase center of adjacent reflected rays are identical points in the limit of very close incident and reflected rays. The caustic curve is the locus of the intersections of adjacent scattered rays. The intersection of adjacent rays is the center of curvature of the localized wavefront; and since it is shown that the center of curvature and the phase center of the localized scattered field (in the plane of tilt) are identical points and lie on the caustic curve, one may say, conversely, that the caustic represents the locus of phase centers of sets of adjacent rays.

A simplified view of the ray optics geometry is seen in Figure 3-4. A single caustic curve is indicated in the figure. In

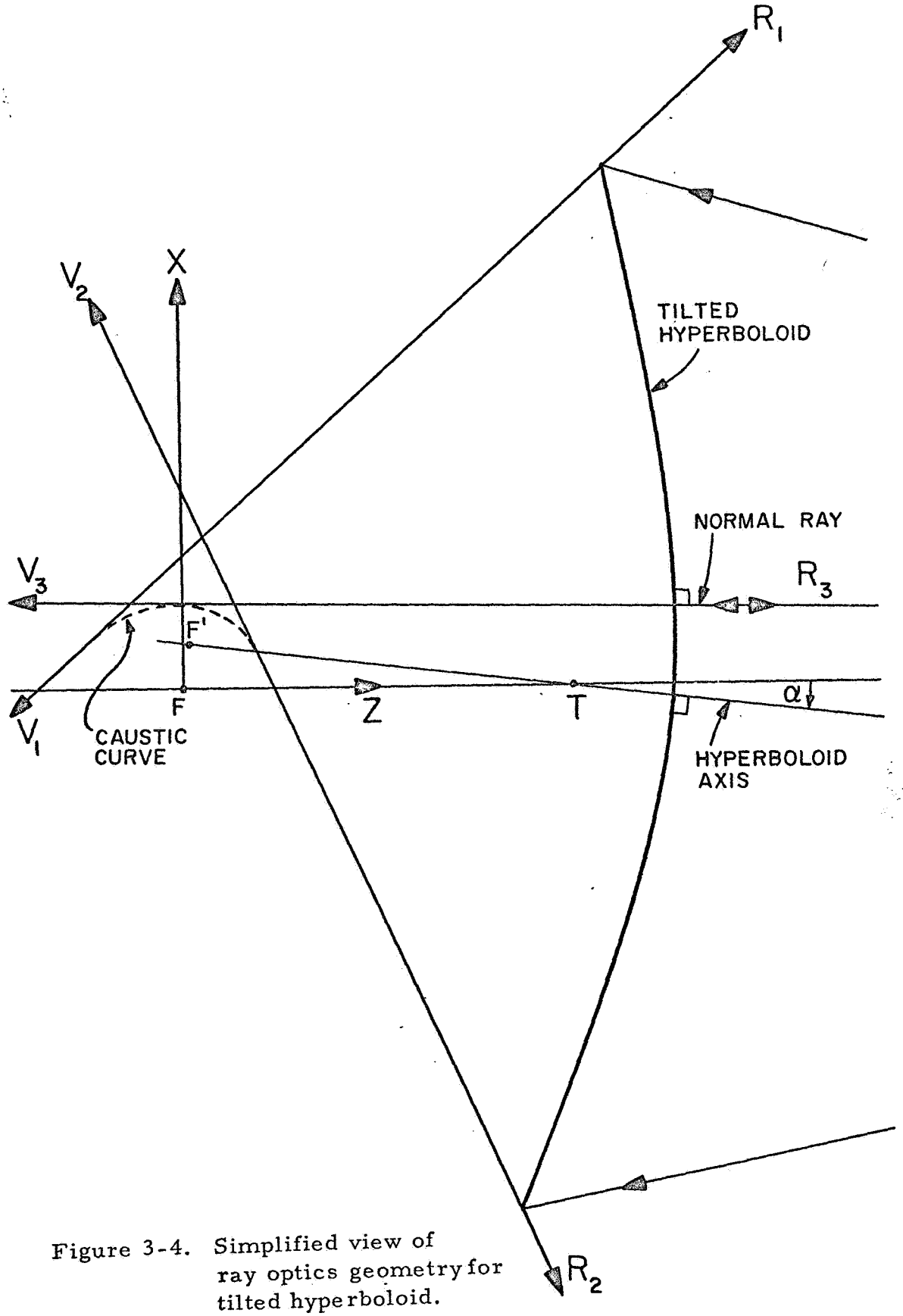

Figure 3-4. Simplified view of ray optics geometry for tilted hyperboloid.

general, there will exist a pair of caustic curves resulting from the asymmetric geometry, each of which corresponds to the loci of the two principal centers of curvature for each point of the reflected wavefront. Consider a particular reflected ray in the X-Z plane extended so as to intersect the wavefront. At the point of intersection, the wavefront will have two principal radii of curvature, one for the curvature in the X-Z plane, and the other for the curvature perpendicular to the X-Z plane. Thus, for every point on the wavefront there is associated a pair of centers of curvature on the virtual extension of the ray through that point. In general, the totality of these points constitute two caustic surfaces. The intersection of these surfaces and the plane of tilt (X-Z plane) yields the double-branched caustic curve. The ray-tracing construction in Figure 3-2 yielded only the lower branch, since only the intersections of rays in the plane of tilt could be plotted.

Knowledge of the geometry and incident wave description in the tilted hyperboloid scattering problem enables one to compute the ray congruence of the scattered field. The ray congruence is specified by giving the ray direction at each point on a reference surface—the reference surface not necessarily being a wavefront.

Following Figure 3-5, the reference surface V will be taken as the hyperboloid surface itself. For ease of computation, a

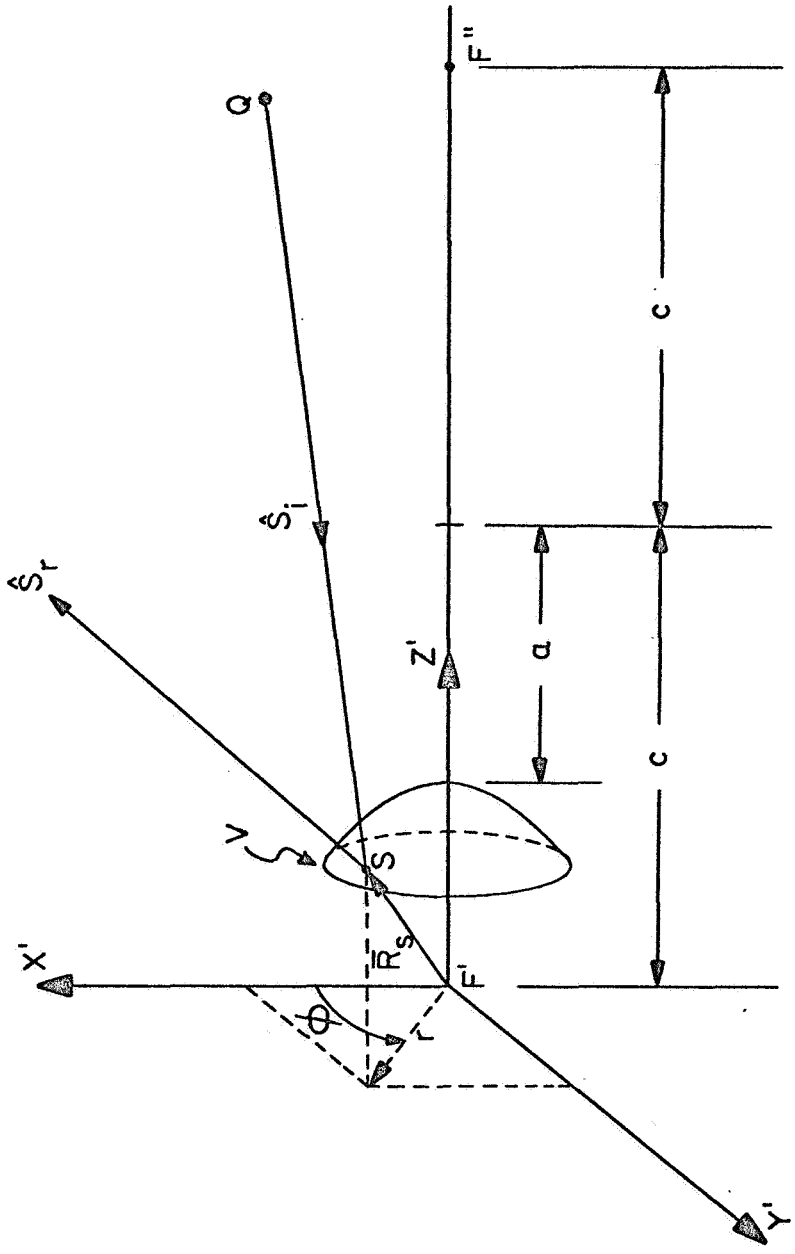

Figure 3-5. Geometry for determination of caustic curves for the tilted geometry.

coordinate system (X'-Z') will be chosen such that the hyperboloid is symmetric with respect to the Z'-axis of that system. The geometric focus F' of the hyperboloid lies at the origin of the system. The source Q is not on the axis of symmetry of the hyperboloid because of the tilted geometry of the problem. Following the determination of the focal surface, a coordinate transformation will be made so that these surfaces may be described in the symmetric coordinate system (X-Z), i.e., that system in which the paraboloid is symmetric and in which the hyperboloid appears to be tilted (cf. Figure 3-3).

The reference surface V in Figure 3-5 may be described as (dropping all primes):

$$\bar{R}_S = x(u,v)\,\hat{a}_x + y(u,v)\,\hat{a}_y + z(u,v)\,\hat{a}_z \qquad (3\text{-}1)$$

where u and v are curvilinear coordinates on V and $\bar{R}_S$ is a vector from the origin to a point S on V.

The reflected ray directions on V are specified by the unit vector $\hat{s}_r(u,v)$ where $\hat{s}_r$ is, by Snell's law

$$\hat{s}_r = \hat{s}_i - 2(\hat{s}_i \cdot \hat{n})\,\hat{n} \qquad (3\text{-}2)$$

and $\hat{s}_i$ = unit vector in the direction of the incident ray

$\hat{n}$ = unit vector normal (outward) to the reflecting surface in the X'-Z' plane.

The distances β_1 and β_2 from S along the reflected ray to the caustic surfaces are given by the solutions to the quadratic equation (23):

$$(EG-F^2)\beta^2 + (Eg-2Ff+Ge)\beta + (eg-f^2) = 0 \qquad (3-3)$$

β_1 and β_2 represent the radii of curvature of the reflected wavefront at V (cf. Figure 3-6).

The elements of Equation (3-3) are:

$$E = \frac{\partial \hat{s}_r}{\partial u} \cdot \frac{\partial \hat{s}_r}{\partial u} \qquad e = \frac{\partial \bar{R}_S}{\partial u} \cdot \frac{\partial \hat{s}_r}{\partial u}$$

$$F = \frac{\partial \hat{s}_r}{\partial u} \cdot \frac{\partial \hat{s}_r}{\partial v} \qquad f = \pm \frac{\partial \bar{R}_S}{\partial u} \cdot \frac{\partial \hat{s}_r}{\partial v} = \frac{\partial \bar{R}_S}{\partial v} \cdot \frac{\partial \hat{s}_r}{\partial u}$$

$$G = \frac{\partial \hat{s}_r}{\partial v} \cdot \frac{\partial \hat{s}_r}{\partial v} \qquad g = \frac{\partial \bar{R}_S}{\partial v} \cdot \frac{\partial \hat{s}_r}{\partial v} \qquad (3-4)$$

The caustic points on the reflected (or virtual) ray will then be

$$\bar{Q}_1 = \bar{R}_S + \beta_1 \hat{s}_r$$
$$\bar{Q}_2 = \bar{R}_S + \beta_2 \hat{s}_r \qquad (3-5)$$

As $\bar{R}_S$ ranges over V, the above formulas determine the caustic surfaces.

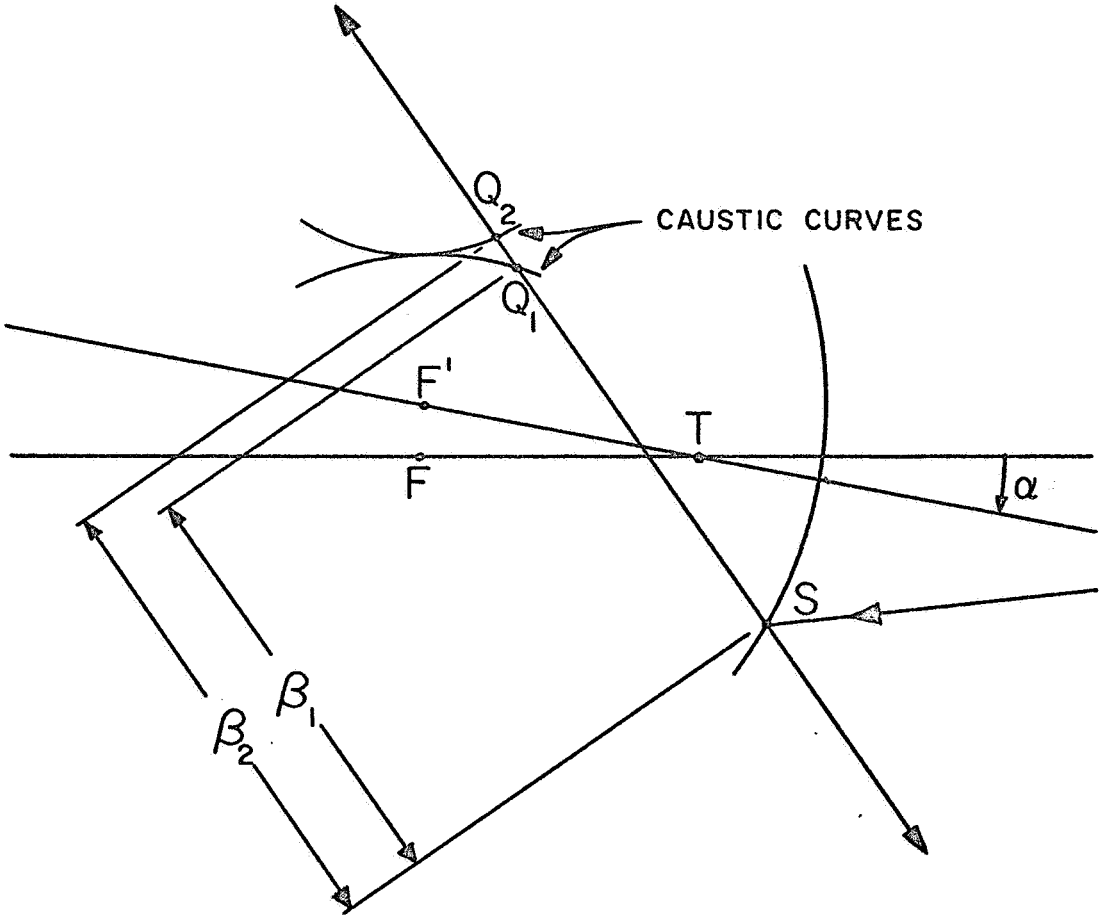

Figure 3-6. Relationship between focal points Q_1 and Q_2, virtual ray, and caustic curves.

Along each reflected ray, two caustic points Q_1 and Q_2 will be found. This indicates that the scattered wavefront has two principal radii of curvature corresponding to the two principal lines of curvature at some localized portion of the reference surface. One line of curvature will be in the plane of tilt, and the other will be perpendicular to the plane of tilt. It can be seen that the loci of the totality of pairs of focal points in the plane of tilt will yield two caustic curves (cf. Figure 3-6).

For the specific case of scattering from a hyperboloid with an off-axis source (cf. Figure 3-5), the following development is carried out utilizing the hyperboloid surface as the ray congruence reference surface.

On the surface of the hyperboloid,

$$\begin{aligned} x_S &= r\cos\varphi \\ y_S &= r\sin\varphi \\ z_S &= c - a\left(1 + \frac{r^2}{c^2-a^2}\right)^{\frac{1}{2}} \end{aligned} \tag{3-6}$$

Therefore,

$$\begin{aligned} \bar{R}_S &= r\cos\varphi\,\hat{a}_x + r\sin\varphi\,\hat{a}_y + \left[c-a\left(1 + \frac{r^2}{c^2-a^2}\right)^{\frac{1}{2}}\right]\hat{a}_z \\ &= R_x\hat{a}_x + R_y\hat{a}_y + R_z\hat{a}_z \end{aligned} \tag{3-7}$$

The incident rays are

$$\hat{s}_i = \frac{(x_S - x_Q)\hat{a}_x + (y_S - y_Q)\hat{a}_y + (z_S - z_Q)\hat{a}_z}{m(\hat{s}_i)} \tag{3-8}$$

where x_S, y_S, z_S are the coordinates of a point on the hyperboloid

$x_Q, y_Q\ z_Q$ are the coordinates of the source point

$$m(\hat{s}_i) = \left[(x_S - x_Q)^2 + (y_S - y_Q)^2 + (z_S - z_Q)^2 \right]^{\frac{1}{2}}$$

The outward normal to the hyperboloid is

$$\hat{n} = \frac{\left(\frac{2x_S}{c^2-a^2}\right)\hat{a}_x + \left(\frac{2y_S}{c^2-a^2}\right)\hat{a}_y + \left(\frac{2}{a^2}\right)\left(c - z_S\right)\hat{a}_z}{m(\hat{n})} \tag{3-9}$$

where $m(\hat{n}) = \left[\left(\frac{2x_S}{c^2-a^2}\right)^2 + \left(\frac{2y_S}{c^2-a^2}\right)^2 + \frac{4}{a^4}\left(c - z_S\right)^2\right]^{\frac{1}{2}}$

The reflected ray then becomes (from Equation (3-2))

$$\hat{s}_r = \hat{s}_i - 2(\hat{s}_i \cdot \hat{n})\hat{n} = \alpha_x \hat{a}_x + \alpha_y \hat{a}_y + \alpha_z \hat{a}_z \tag{3-10}$$

where

$$\alpha_x = \frac{1}{m(\hat{s}_i)}\left[(x_S - x_Q) - \frac{8x_S}{(c^2-a^2)^2} \cdot \left(\frac{1}{m(\hat{n})}\right)^2 \cdot (G_1)\right]$$

$$\alpha_y = \frac{1}{m(\hat{s}_i)}\left[(y_S - y_Q) - \frac{8y_S}{(c^2-a^2)^2}\cdot\left(\frac{1}{m(\hat{n})}\right)^2\cdot(G_1)\right]$$

$$\alpha_z = \frac{1}{m(\hat{s}_i)}\left[(z_S - z_Q) - \frac{8(z_S-c)}{a^2(a^2-c^2)}\left(\frac{1}{m(\hat{n})}\right)^2(G_1)\right]$$

and

$$(G_1) = x_S^2 + y_S^2 - x_S x_Q - y_S y_Q + \left(\frac{a^2-c^2}{a^2}\right)\cdot\left(z_S^2 - z_S z_Q - z_S c + z_Q c\right)$$

Identifying the curvilinear coordinates u and v with r and φ respectively, Equations (3-4) become:

$$E = \frac{\partial \hat{s}_r}{\partial r}\cdot\frac{\partial \hat{s}_r}{\partial r} \qquad e = \frac{\partial \bar{R}_S}{\partial r}\cdot\frac{\partial \hat{s}_r}{\partial r}$$

$$F = \frac{\partial \hat{s}_r}{\partial r}\cdot\frac{\partial \hat{s}_r}{\partial \varphi} \qquad f = \pm\frac{\partial \bar{R}_S}{\partial r}\cdot\frac{\partial \hat{s}_r}{\partial \varphi} = \frac{\partial \bar{R}_S}{\partial \varphi}\cdot\frac{\partial \hat{s}_r}{\partial r}$$

$$G = \frac{\partial \hat{s}_r}{\partial \varphi}\cdot\frac{\partial \hat{s}_r}{\partial \varphi} \qquad g = \frac{\partial \bar{R}_S}{\partial \varphi}\cdot\frac{\partial \hat{s}_r}{\partial \varphi} \qquad (3\text{-}11)$$

For each particular point S, solutions β_1 and β_2 to Equation (3-3) are found. The caustic curves are determined by allowing S to range over the line determined by the intersection of the hyperboloid surface and the plane of tilt (X'-Z'), thus yielding families of points Q_1 and Q_2 defined by Equation (3-5).

A computer program solving Equations (3-1) through (3-11) has been developed to determine the caustic curves associated with reflections from a tilted hyperboloid. A listing of the program is given in Appendix C. Figure 3-7 shows the caustic curves determined from the computer calculations. Both the untilted (F) and tilted (F') coordinate systems are indicated in the figure. It is determined that the position of intersection of the caustic curves in the untilted coordinate system is at the point:

$R_{ci} = 5.321$ mm (= 1.598 λ for λ = 3.33 mm in the nodding subdish system)

$\theta_{ci} = 88.755^{o}$ (measured from the Z-axis)

$\varphi_{ci} = 0.0^{o}$ (measured from the X-axis)

The above caustic intersection point is shown in Figure 3-7. It will be shown later that the caustic intersection point is approximately one-tenth wavelength from the positions of the geometrical optics phase center and the diffraction theory phsse center for the nodding subdish system in particular (λ = 3.33 mm, D/λ = 59.54). The caustic intersection point is approximately 0.9λ (for λ = 3.33 mm) from the position of the hyperboloid geometric focus (point F', Figures 3-3 and 3-7).

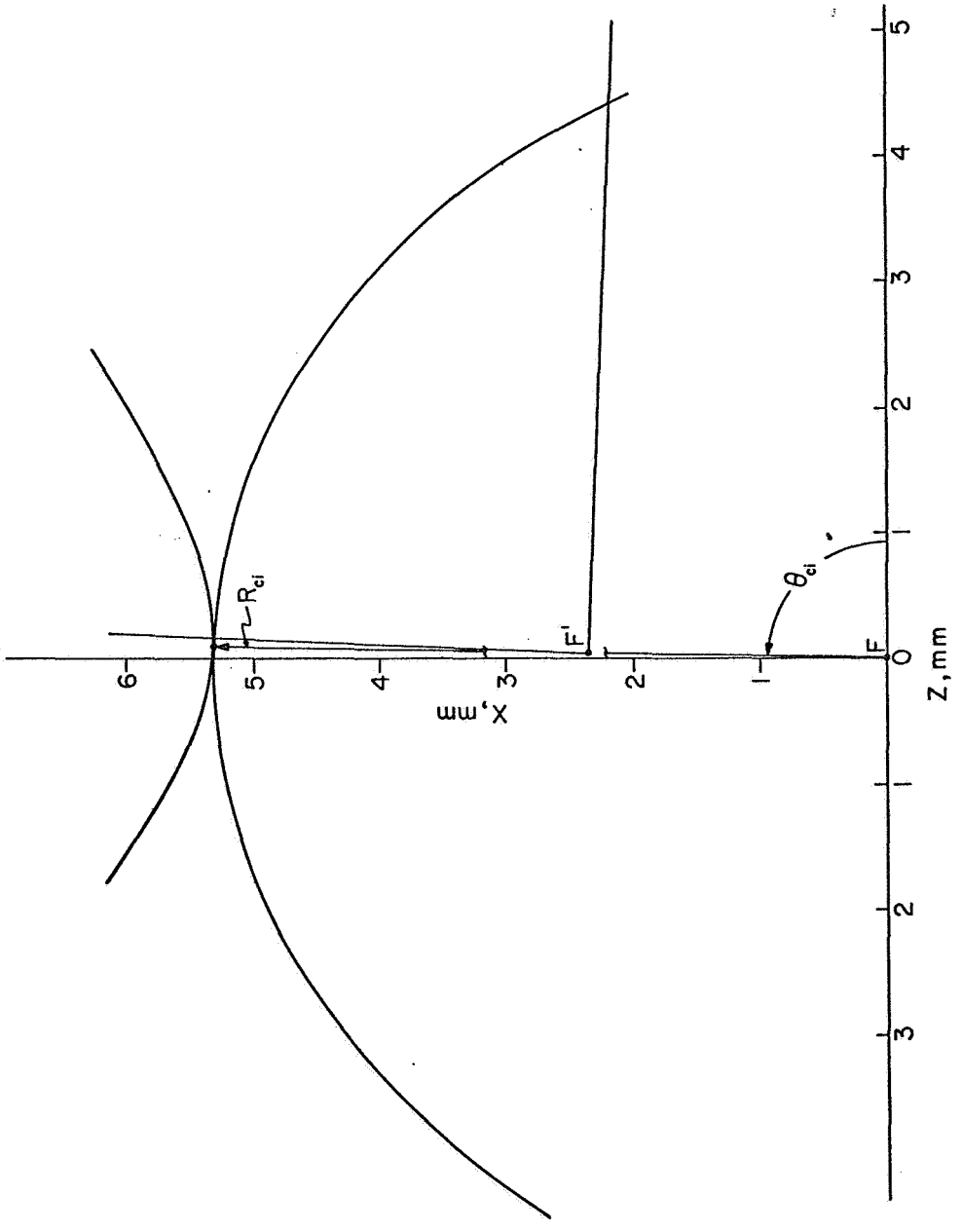

Figure 3-7. Double-branched caustic curve associated with the reflected rays for a specific asymmetric geometry.

3.3.2 Best-fit Phase Center - Geometrical Optics

A geometrical-optics analysis of phase center position was undertaken to determine the possible agreement between the diffraction theory results and geometrical optics results in the case of a tilted hyperboloid geometry. Figure 3-8 shows that ray tracing from the source Q to various points on the hyperboloid, and then by reflection to points P on a very large circle (S') centered at F' (the origin of the tilted coordinate system) will allow one to determine the phase of the scattered field on the large circle. In terms of path length, with $\theta_2 \approx \theta_1$ for large R,

$$\text{path length} = \overline{QS} + R' \cong \overline{QS}\left[R - \rho \cos(\theta_2 - \theta_3)\right]$$

$$\cong \overline{QS} + \left[R - \rho \cos(\theta_1 - \theta_3)\right] \qquad (3\text{-}12)$$

The problem of finding a new phase center in the tilted coordinate system is a problem of determining the point 0 which is the center of concentric circles (S'') upon which the reflected field has approximately constant phase, in a specific sense.

The phase at point P measured from 0 is (kr - c), where c is quasi-constant.

The actual path length description of phase at point P is, from Equation (3-12),

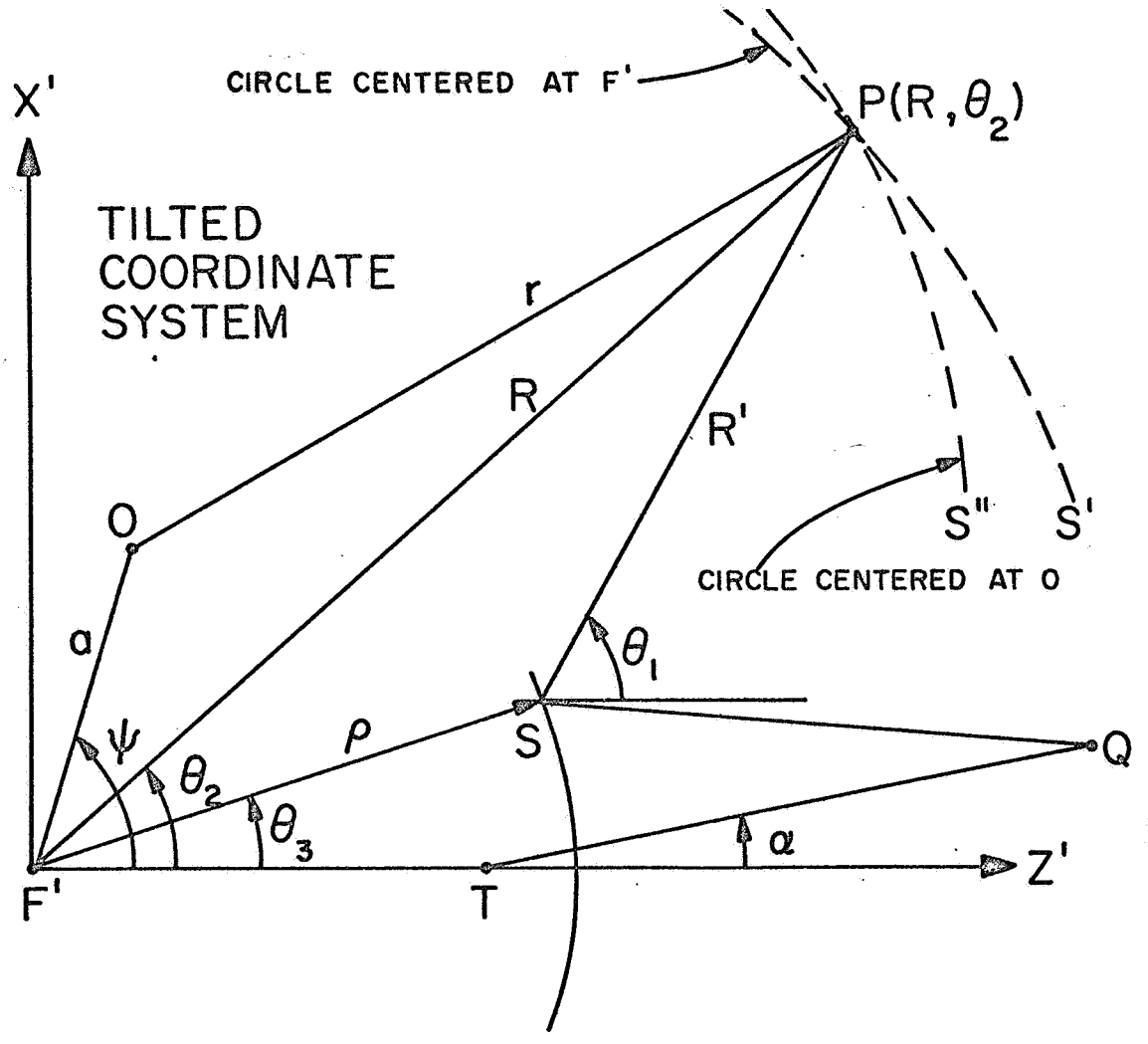

Figure 3-8. Phase center geometry, tilted hyperboloid, tilted coordinate system.

$$\text{path length phase} = k\left[\overline{QS} + R - \rho \cos(\theta_1 - \theta_3)\right] .$$

The difference between the phase at point P measured from 0 (the desired constant phase) and the path length phase (the actual phase) is:

$$\Delta = k\left[\overline{QS} + R - \rho\cos(\theta_1 - \theta_3)\right] - (kr - c) .$$

But $r = R - a\cos(\psi - \theta_2)$, for $R, r \gg a$, from Figure 3-8.

The phase difference then becomes, for $\theta_2 \approx \theta_1$,

$$\Delta = k\overline{QS} - k\rho\cos(\theta_1 - \theta_3) + ka\cos(\psi - \theta_1) + c .$$

If we define $k\left[\overline{QS} - \rho\cos(\theta_1 - \theta_3)\right]$ as $-\Phi(\theta_1)$, the phase difference becomes

$$\Delta = c + ka\cos(\psi - \theta_1) - \Phi(\theta_1) . \qquad (3\text{-}13)$$

The 180° phase shift undergone by all incident rays upon reflection from the hyperboloid surface need not be considered in this analysis. Since the phase difference Δ is minimized in a least squares sense, the addition or subtraction of a constant, c', to the value of Δ ($\Delta \pm c'$) cannot affect the parameters (ka and ψ) of Equation (3-13).

For a constant R, the phase may also be defined as

$$-\Phi(\theta_1)_{\text{degrees}} = (\text{path length} - R) \cdot \frac{360^\circ}{\lambda}$$

$$= \left[\overline{QS} - \rho \cos(\theta_1 - \theta_3)\right] \cdot \frac{360^\circ}{\lambda} \qquad (3\text{-}14)$$

where λ is the wavelength, or an arbitrary constant. The expression for $\Phi(\theta_1)$ in Equation (3-14) is used in Equation (3-13) to give the phase on the circle centered at F'.

A computer program (cf. Appendix C) was written to determine the geometrical optics phase, $\Phi(\theta_1)$, in Equation (3-14) for rays emanating from Q and reflected from the hyperboloid. This program utilizes the geometrical relationships needed to determine the caustic curves in the preceding section; and the solution of Equation (3-14) is included in that program as a specific addition for determining the phase of the reflected geometrical optics field. Knowing this phase on the arbitrary circle centered at the origin of the tilted coordinate system (F') enables one to determine the phase center by a least squares fit method. The quantity Δ, which represents the difference between the theoretically constant phase on the circle S'' (cf. Figure 3-8) and the actual non-constant phase $\Phi(\theta_1)$ on the circle S' is minimized in a least squares sense. Equation (3-14) must be solved for ka, ψ, and c to minimize the variance of the differences between

the two descriptions of phase.

$\Phi(\theta_1)$ as a function of θ_1 is known from Equation (3-14); but since the phase $\Phi(\theta_1)$ of the reflected rays changes rapidly and monotonically, the best-fit phase center will be a function of the range of θ_1 considered.

For accurate comparison with an experimental determination of the phase center, the theoretical calculations should be made using only those values of θ_1 which are experimentally significant, i.e., only those values which arise from actual physical reflections from the hyperboloid surface, at radii of less than 3.9 inches (for the nodding subdish system).

The computed phase $\Phi(\theta_1)$ is a series of discrete values determined by computer solutions of Equation (3-14). This computed phase must be written as $\Phi_i(\theta_{1i})$.

Thus, the phase difference equation to be solved becomes

$$\Delta_i = c + ka \cos(\psi - \theta_{1i}) - \Phi_i(\theta_{1i}) \qquad (3\text{-}15)$$

The variance of the difference between the postulated phase $[c + ka \cos(\psi - \theta_{1i})]$ and the actual phase $[\Phi_i(\theta_{1i})]$ is

$$\sigma^2 = \sum_{i=1}^{N} \Delta_i^2 = \sum_{i=1}^{N} \left[c + ka \cos(\psi - \theta_{1i}) - \Phi_i(\theta_{1i}) \right]^2 \qquad (3\text{-}16)$$

The unknown ψ must be "separated" from the term $\cos(\psi - \theta_{1i})$ in order to determine a solution for ka, ψ, and c by minimizing σ^2 with respect to these variables. Utilizing the identity

$$\cos(\psi - \theta_{1i}) = \cos\psi \cos\theta_{1i} + \sin\psi \sin\theta_{1i}$$

we obtain

$$\sigma^2 = \sum_{i=1}^{N} \left[c + ka \cos\psi \cos\theta_{1i} + ka \sin\psi \sin\theta_{1i} - \Phi(\theta_{1i}) \right]^2 \qquad (3\text{-}17)$$

Applying the minimization conditions

$$(1) \quad \frac{\partial \sigma^2}{\partial c} = 0$$

$$(2) \quad \frac{\partial \sigma^2}{\partial (ka \cos\psi)} = 0 \qquad (3\text{-}18)$$

$$(3) \quad \frac{\partial \sigma^2}{\partial (ka \sin\psi)} = 0$$

we obtain three homogeneous equations which may be solved for c, ψ, and ka.

Equation (3-17) does not take into consideration the fact that the amplitude of the scattered field varies with θ_{1i}, hence a weighting factor must be introduced to give a more accurate phase center determination. A weight can be assigned to each particular value of the actual phase, $\Phi_i(\theta_{1i})$, in direct proportion to the power level of

the scattered field at each corresponding θ_{1i}. Thus, with weighting considered, the variance is expressed as

$$\sigma^2 = \sum_{i=1}^{N} w_i (\Delta_i)^2 \tag{3-19}$$

where w_i are the weights for each value of phase, proportional to E_θ^2.

Rewriting the variance relation in the form of Equation (3-16), we obtain

$$\sigma^2 = \sum_{i=1}^{N} w_i \left[c + ka \cos (\psi - \theta_{1i}) - \Phi_i(\theta_{1i}) \right]^2 \tag{3-20}$$

Applying the minimization conditions, we obtain the following homogeneous equations to be solved for ka, ψ, and c.

$$\begin{aligned}
&\sum_{i=1}^{N} 2w_i \left[c + ka \cos\psi \cos\theta_{1i} + ka \sin\psi \sin\theta_{1i} - \Phi_i(\theta_{1i}) \right] = 0 \\
&\sum_{i=1}^{N} 2w_i \left[c + ka \cos\psi \cos\theta_{1i} + ka \sin\psi \sin\theta_{1i} - \Phi_i(\theta_{1i}) \right] \left[\cos\theta_{1i} \right] = 0 \\
&\sum_{i=1}^{N} 2w_i \left[c + ka \cos\psi \cos\theta_{1i} + ka \sin\psi \sin\theta_{1i} - \Phi_i(\theta_{1i}) \right] \left[\sin\theta_{1i} \right] = 0
\end{aligned} \tag{3-21}$$

A determination of the geometrical optics phase center, with weighting of each phase equal to 1.0 ($w_i = 1.0$, the non-weighted case) yields the best-fit phase center point (0) at

$$a = 5.884 \text{ mm} \quad (= 1.767\lambda \quad \text{for } \lambda = 3.33 \text{ mm})$$

$$\psi = 87.262^{\circ}$$

measured in the untilted coordinate system, after a coordinate transformation.

Weighting of each phase is done following the method given in Chapter 2 for determining the magnitude of the field amplitude in the geometrical optics scattering determination (Chapter 2, Equation 2-39). With weighting considered, the best-fit geometrical optics phase center was determined to be at the point

$$a = 5.714 \text{ mm} \quad (= 1.716\lambda \quad \text{for } \lambda = 3.33 \text{ mm})$$

$$\psi = 87.148^{\circ}$$

measured in the untilted coordinate system. The weighted phase center point is approximately 0.17 mm closer to the caustic intersection point than is the unweighted phase center. As can be seen from Figure 3-4, virtual rays from the edges of the hyperboloid contribute to phase center points at the extremes of the caustic curve. Weighting reduces the effects of reflections from the edges of the hyperboloid. The effect on phase center position is rather small, however.

3.3.3 Best-fit Phase Center - Physical Optics

The phase center determination in this section is based upon an extension of the method used by Rusch (22) to determine the phase center of the scattered field in a symmetric hyperboloid geometry. Since accurate, experimentally verified results are obtained for the symmetric phase center determination, it is felt that the use of this method in the non-symmetric case will also yield correct results.

The phase and amplitude of the scattered field are obtained from a diffraction-theory (physical optics) analysis of scattering from a tilted hyperboloid. The method used is restricted to the case where the dimensions and radii of curvature of the wavefront and hyperboloid are large relative to a wavelength. Since the technique includes the vector nature of the field, it has been assumed that the incident field from Q is polarized in the plane of the tilt. Because of the symmetry of the geometry and the illumination, the scattered field will be symmetrical about the plane of tilt, and the phase center of the scattered field will lie in the plane of the tilt.

The determination of the phase center in the diffraction-theory case is carried out in a manner quite similar to that in the geometrical-optics case. The differences are: (1) the calculation in the diffraction theory case is carried out in the untilted coordinate system, and (2) the phase is determined from the scattered field

found by a diffraction theory analysis, rather than from a ray tracing procedure. A variance relation similar to Equation (3-16) is obtained in the diffraction theory analysis also.

The electric field scattered from the hyperboloid is given as

$$E_s \sim \frac{e^{-jkR}}{R} \left[\text{Re } E + j \text{ Im } E \right] \tag{3-22}$$

$$= |E| \cdot \frac{e^{-jkR}}{R} \cdot e^{+j\Phi(\theta)} \tag{3-23}$$

$$= |E| \cdot \frac{e^{-jkR}}{R} \left[\cos \Phi(\theta) + j \sin \Phi(\theta) \right] \tag{3-24}$$

where

$$\Phi(\theta) = \tan^{-1}\left(\frac{\text{Im } E}{\text{Re } E} \right) \tag{3-25}$$

and E has been computed by the methods of Chapter 2. The phase of the scattered field is computed from Equation (3-25). Consider the geometry shown in Figure 3-9. This figure differs from Figure 3-8 in that Figure 3-9 represents the untilted coordinate system and Figure 3-8 represents the tilted coordinate system. The problem of finding a new equivalent phase center is again a problem of determining a point 0 which is the center of concentric circles (S'') upon which the scattered field has approximately constant phase, in a specific sense.

If the scattered field is measured from F, then we may write

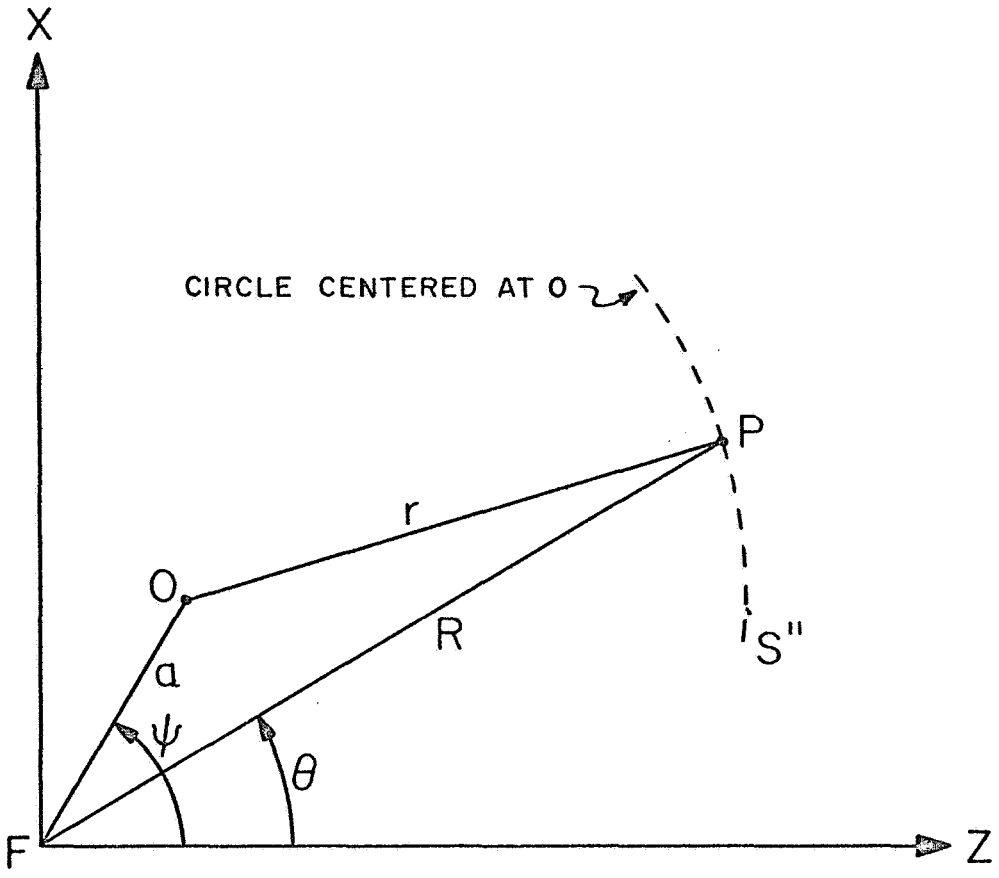

Figure 3-9. Phase center geometry, tilted hyperboloid, untilted coordinate system.

for the scattered field at P:

$$E_s \sim |E| \cdot \frac{e^{-jkR}}{R} \cdot e^{+j\Phi(\theta)} \tag{3-26}$$

If the scattered field is measured from 0, then the scattered field at P is

$$E_s \sim |E| \frac{e^{-j(kr-c)}}{r} \tag{3-27}$$

where the surface r = constant is required to be a surface of constant or nearly constant phase, and c is quasi-constant.

Since the field point P is independent of the coordinate system, then the phases measured in both systems must be equal. However, due to variations in $\Phi(\theta)$ a truly spherical equiphase surface S" centered at 0 may not exist. Nevertheless, a point 0 may be defined such that it yields the "best" nearly constant phase circles (intersections of spheres and the plane of tilt) in a least squares sense. Consequently, to determine the position of 0

Δ = (computed phase at P) - (phase on circle of constant radius)

is minimized in a least squares sense. This difference is (from Equations 3-26 and 3-27)

$$\Delta = [kR - \Phi(\theta)] - [kr-c] \tag{3-28}$$

But $R = r + a \cos(\psi - \theta)$ for $R, r \gg a$.

Therefore,

$$\Delta = [kr + ka \cos(\psi - \theta) - \Phi(\theta)] - [kr - c] \tag{3-29}$$

and

$$\Delta = c + ka \cos(\psi - \theta) - \Phi(\theta) \tag{3-30}$$

Equation (3-30) must be solved for ka, ψ, and c to minimize the variance of the differences between the computed phase at P and the phase on a circle of constant radius passing through P and centered at 0.

Since $\Phi(\theta)$ as a function of θ is known (from Equation 3-25), there must exist some values of a and ψ which will minimize the variance of Δ. This is precisely the identical situation as in the geometrical optics phase center determination (Section 3.3.2).

Since the phase $\Phi(\theta)$ of the scattered field changes rapidly and monotonically, the best-fit phase center will again be a function of the range of θ considered. For accurate comparison with experimental determination of the phase center, the theoretical calculations should be made using only those values of θ which are experimentally significant, i.e., only those values which will "illuminate" the paraboloid with the scattered field. The paraboloid in the nodding

subdish system subtends an angle of 60^{o} from center to edge as viewed from the focus; and values of θ are confined to that range.

The incident spherical wave illuminates the subreflector symmetrically in φ_1; $E_i(+\varphi_1) = E_i(-\varphi_1)$ (cf. Figure 2-2). The phase center will thus move only in the plane of tilt, i.e., only in the plane $\varphi_1 = 0, \pi$.

The computed phase $\Phi(\theta)$ is a series of discrete values as determined by a computer output of E_θ vs. θ. This computed phase must be written as $\Phi_i(\theta_i)$.

Thus, the equation to be solved becomes

$$\Delta_i = c + ka \cos(\psi - \theta_i) - \Phi_i(\theta_i) \quad . \tag{3-31}$$

This is identical to Equation (3-15).

Minimization of the weighted variance of Δ_i leads to equations similar to Equations (3-21). ka and ψ represent the radial and angular positions of the best-fit phase center. The weight of each phase $\Phi_i(\theta_i)$ is made proportional to the square of the electric field strength (E_θ^2).

In conjunction with the geometrical optics and diffraction theory scattering studies carried out in Chapter 2, a series of phase center analyses were carried out to investigate the effect of various

hyperboloid diameter/wavelength ratios upon the position of the phase centers of the scattered field.

The three diffraction theory cases with D/λ equal to 59.54 (the nodding subdish system), 24, and 10 yield the following values for weighted and unweighted values of phase center position (where "a" is the radial distance from the origin of the untilted coordinate system):

No.	D/λ	λ (mm)	a(λ)	a(mm)	ψ
1	59.54, unweighted	3.33	1.754λ	5.841	89.604°
2	59.54, weighted	3.33	1.707λ	5.684	88.107°
3	24, unweighted	8.26	0.704λ	5.818	90.727°
4	24, weighted	8.26	0.689λ	5.691	89.373°
5	10, unweighted	19.83	0.288λ	5.711	90.526°
6	10, weighted	19.83	0.289λ	5.731	94.041°

Table 3-1

"Unweighted" refers to a weighting value of 1.00000 for each phase point. "Weighted" refers to weighting proportional to E_θ^2. In each of the above cases, there is less than 1/20 wavelength difference between the weighted and unweighted phase center positions. Of

particular interest in Table 3-1 is the column labeled "a(mm)", giving the radial value (in millimeters) of the phase center position for the nodding subdish system geometry. When the values "a(mm)" and "ψ" are considered together, it may be seen that the best-fit phase center positions, based on diffraction theory analyses, are "independent" of the value of D/λ. With the exception of the $D/\lambda = 10$ (weighted) point, all the diffraction theory phase centers lie within 0.1 mm of each other. It must be pointed out that although the radial positions differ markedly when compared in terms of wavelengths, the positions are almost identical when compared in terms of distance in millimeters from the origin of the untilted coordinate system.

Following Equation (3-30), the phase difference expression may be rewritten as

$$\Phi(\theta) - ka \cos(\theta - \psi) = \text{CONSTANT}(\theta) \qquad (3\text{-}32)$$

Since the diffraction theory scattering analysis yields values of $\Phi(\theta)$ vs. θ, a CONSTANT may be determined for each $\Phi_i(\theta_i)$ and θ_i for given values of ka and ψ. The variation of CONSTANT is equivalent to a variation of phase on circles centered at the specific points specified by ka and ψ. For D/λ ratios of 59.54 (the nodding subdish system), 24, and 10, the phases (CONSTANTs) determined by diffraction theory analyses were determined around the best-fit phase

center, around the origin, and around the caustic intersection point. Table 3-2 shows the values pertinent to the analyses, along with the rms phase error in degrees (RMSDEL) around each of the three points for each of the three cases. It can be seen that the rms phase error around the best-fit phase center for each case is substantially lower than around either of the other two points. The phase variation around the caustic intersection point is determined because of its proximity to the position of the best-fit phase center. Figures 3-10 through 3-12 show the phase plotted around the origin of the untilted coordinate system (F) and around the best-fit phase center (0) for each of the three D/λ cases. In the $D/\lambda = 59.54$ case, for example, the phase measured from the origin varies over more than 1100° with a 344.44° rms phase error; while around the best-fit weighted phase center (as determined by a and ψ in Table 3-1) the phase varies by less than 80° over the entire range and by less than 30° over about 80% of the range, with an rms phase error of 17.634°. a and ψ for each point correspond to the results determined in the weighted cases.

The diffraction theory phase centers for the three different D/λ ratios lie within 1/10 wavelength, or less, of each other for D/λ as small as 10. The diffraction theory results agree quite well with the weighted geometrical optics best-fit phase center position ($a = 5.714$ mm, $\psi = 87.148^{\circ}$), which is located approximately 0.1 mm

D/λ	Around	KA	PSI	Radius (λ)	Radius (mm)	RMSDEL
59.54 (nodding subdish system λ = 3.33mm)	Best-fit	614.570	88.107°	1.707λ	5.684 mm	17.634°
	Origin	000.000	88.107°	0.000λ	0.000 mm	344.44°
	Caustic	575.280	88.755°	1.598λ	5.321 mm	34.006°
24 λ = 8.26mm	Best-fit	248.060	89.373°	0.689λ	5.691 mm	6.736°
	Origin	000.000	89.373°	0.000λ	0.000 mm	138.23°
	Caustic	231.890	88.755°	0.644λ	5.321 mm	13.250°
10 λ =19.83mm	Best-fit	103.960	94.041°	0.289λ	5.731 mm	4.655°
	Origin	000.000	94.041°	0.000λ	0.000 mm	56.751°
	Caustic	96.621	88.755°	0.268λ	5.321 mm	6.025°

Table 3-2

Phase Center Analyses Based Upon Diffraction Theory Results (cf. Figures 3-10, 11, 12)

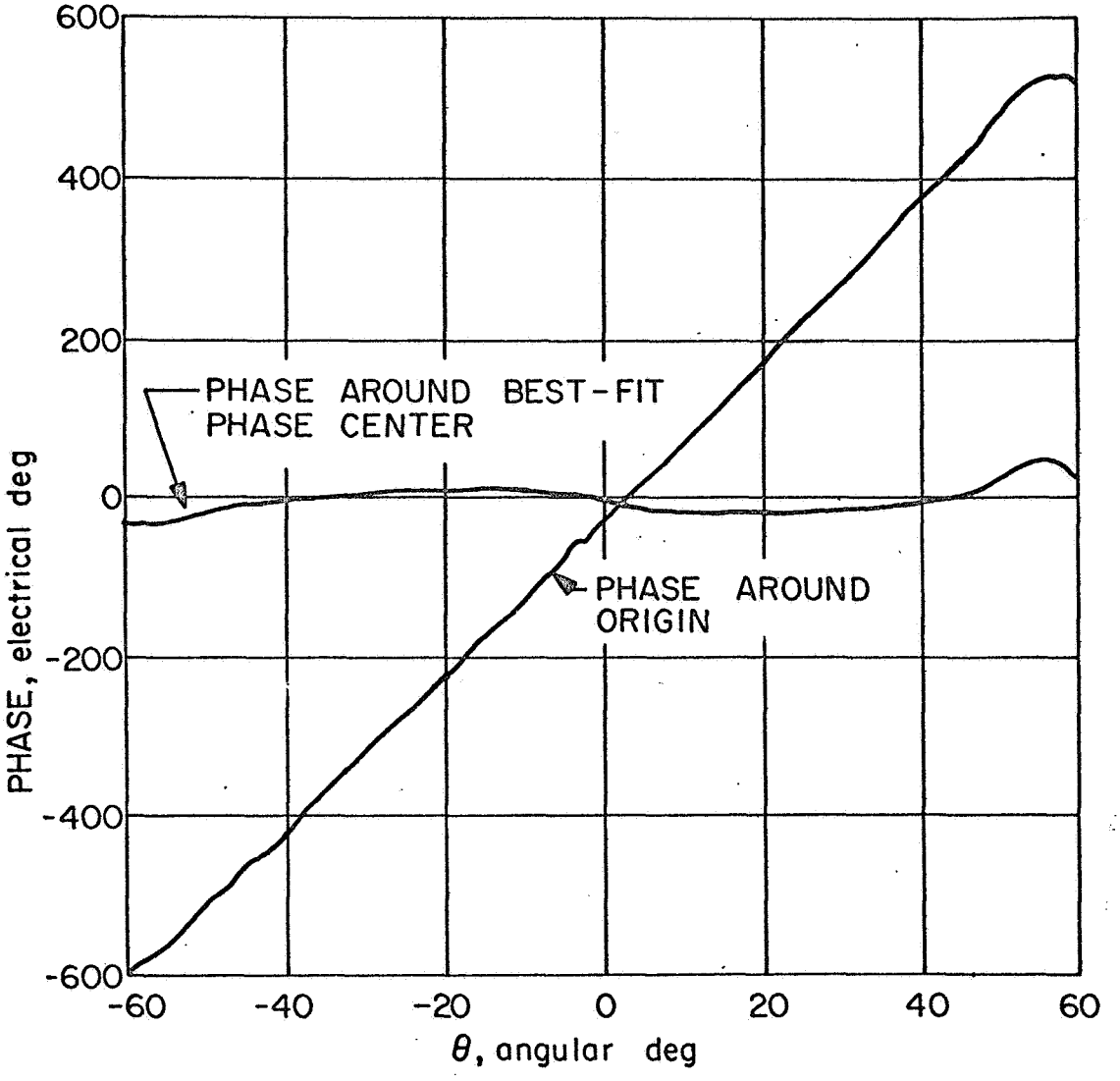

Figure 3-10. Physical optics phase function. $D/\lambda = 59.54$.

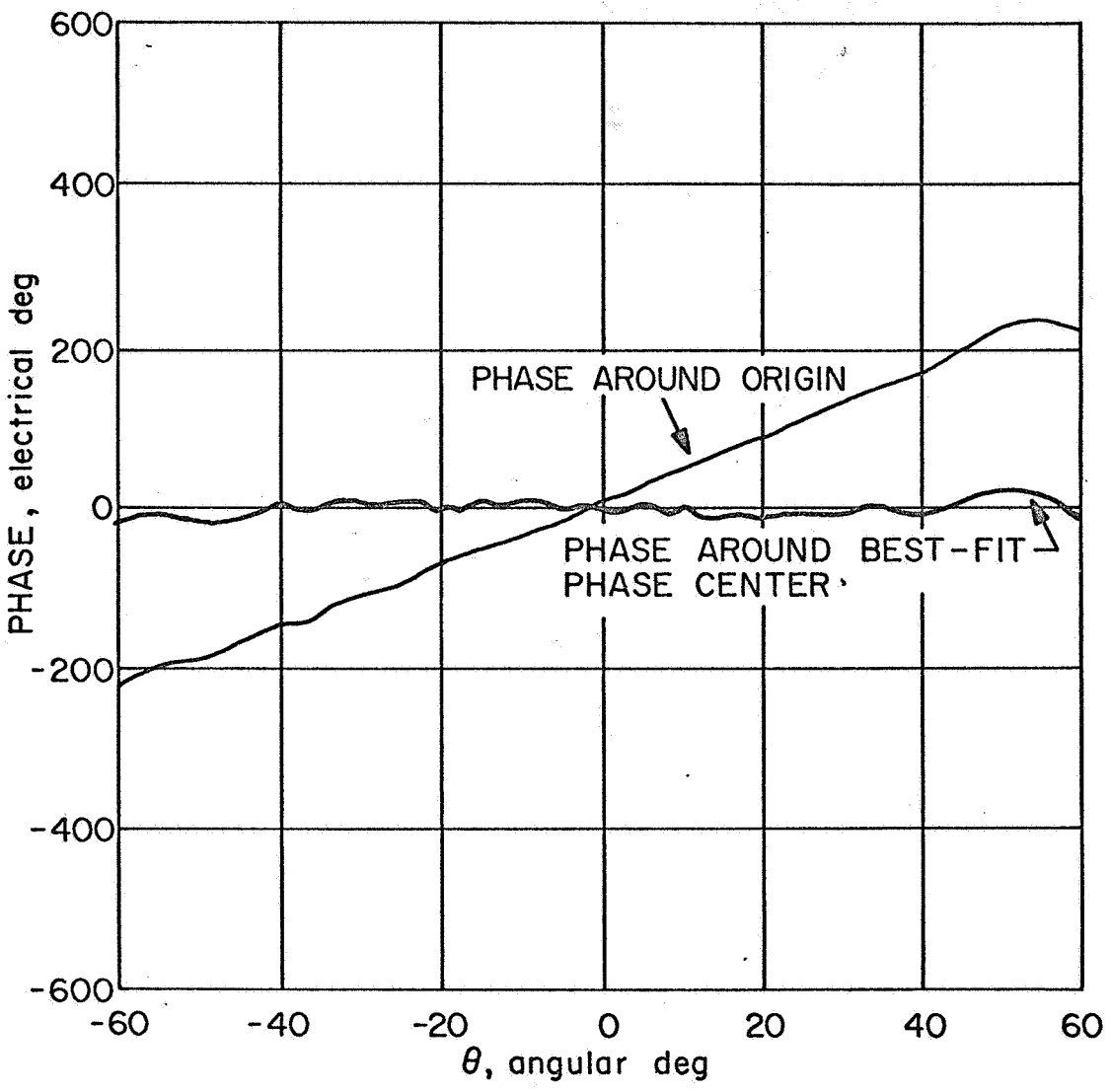

Figure 3-11. Physical optics phase function. $D/\lambda = 24$.

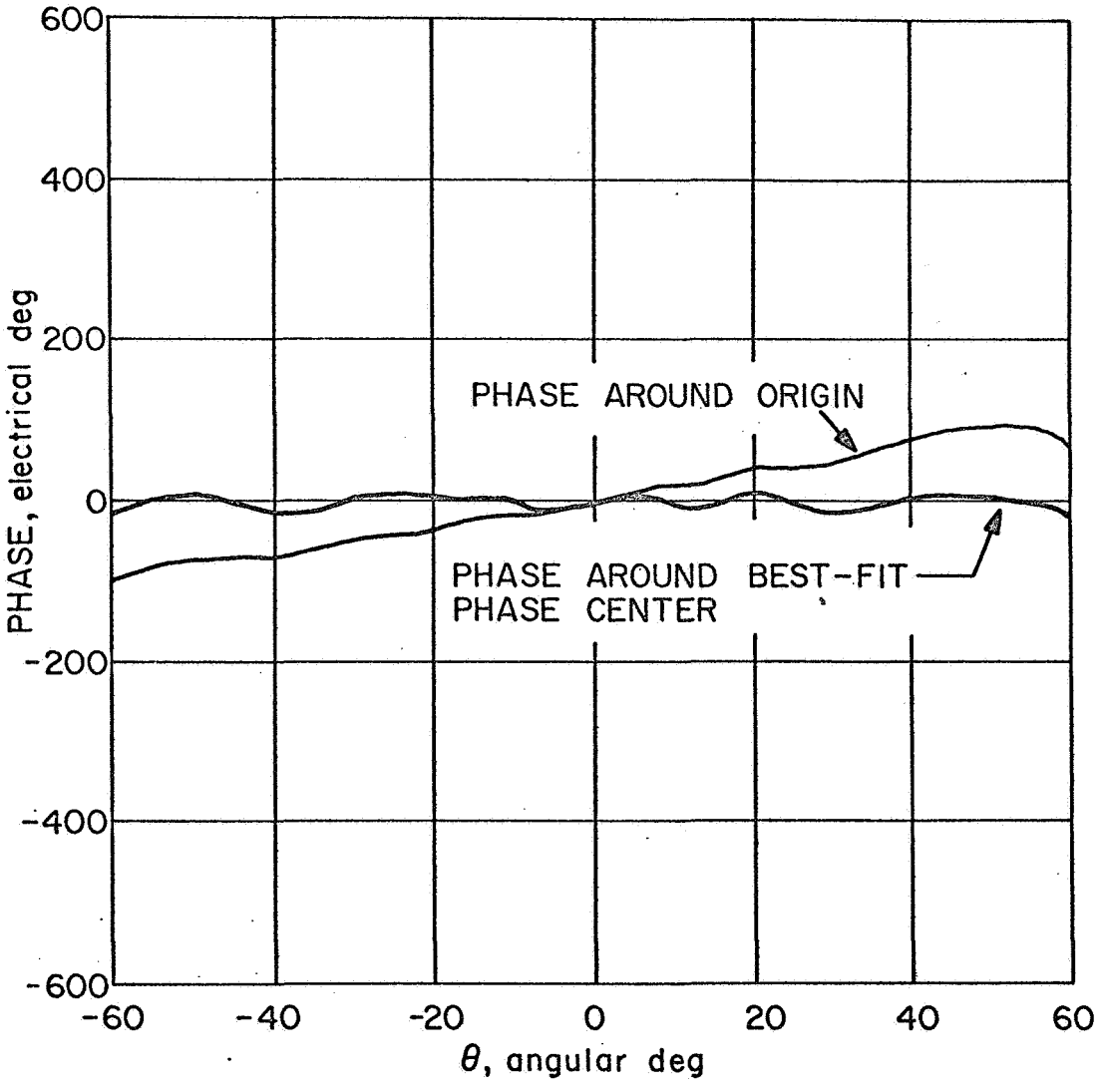

Figure 3-12. Physical optics phase function. $D/\lambda = 10$.

from the $D/\lambda = 59.54$ (weighted) point. These analyses show that geometrical optics determinations of phase center position may be used with considerable accuracy down to D/λ ratios as low as 10. This will be a function of the geometry of the problem, however, and care should be taken in extending geometrical optics analyses to different geometries.

As indicated previously, the variance expressions used in the determination of the best-fit phase centers were summed over the entire angular range subtended by the primary paraboloidal mirror. For the three cases considered, field points were taken every degree so that 121 points were taken. In the same manner, differential phase centers over smaller angular ranges can be computed by summing the variance over smaller angular ranges. Because of the discrete step size there is ultimately a lower limit on the size of the angular range that may be considered. It was discovered that for the $D/\lambda = 59.54$ case, a minimum number of forty steps needed to be taken. Less than forty steps yielded extremely erratic phase center determinations. Consequently, differential phase centers for the following forty-step intervals of the scattered field were computed from Equations (3-21) for the diffraction theory results:

40A: -60 deg to -21 deg	40F: -10 deg to +29 deg
40B: -50 deg to -11 deg	40G: 0 deg to +39 deg
40C: -40 deg to -1 deg	40H: +10 deg to +49 deg
40D: -30 deg to +9 deg	40I: +20 deg to +59 deg
40E: -20 deg to +19 deg	

The positions of these differential phase centers for the above nine forty-step intervals of the scattered field are plotted in Figure 3-13 along with the two branches of the ray-optical caustic curve computed in Section 3.3.1. It is seen that these points follow the lower branch of the caustic, although lying a small fraction of a wavelength above it.

In the same manner differential phase centers were calculated for seven sixty-step intervals, five eight-step intervals, and three hundred-step intervals. These results are plotted on the figure along with the phase center of the total field (121 steps from -60 degrees to + 60 degrees). It is seen that as the width of the angular interval decreases, the differential phase centers approach the caustic curve a result which is easily proved with a ray-optical analysis (cf. Appendix B).

3.3.4 Intersecting Circles Determination of Phase Center

A simple geometrical interpretation of the constant and non-constant phase circles surrounding the asymmetric and symmetric phase centers is carried out in this section. This method is, in a way, a graphical solution to the analysis developed in the best-fit phase center determinations.

For small angular tilt of the hyperboloidal subdish, it may be assumed that the movement of the phase center of the scattered

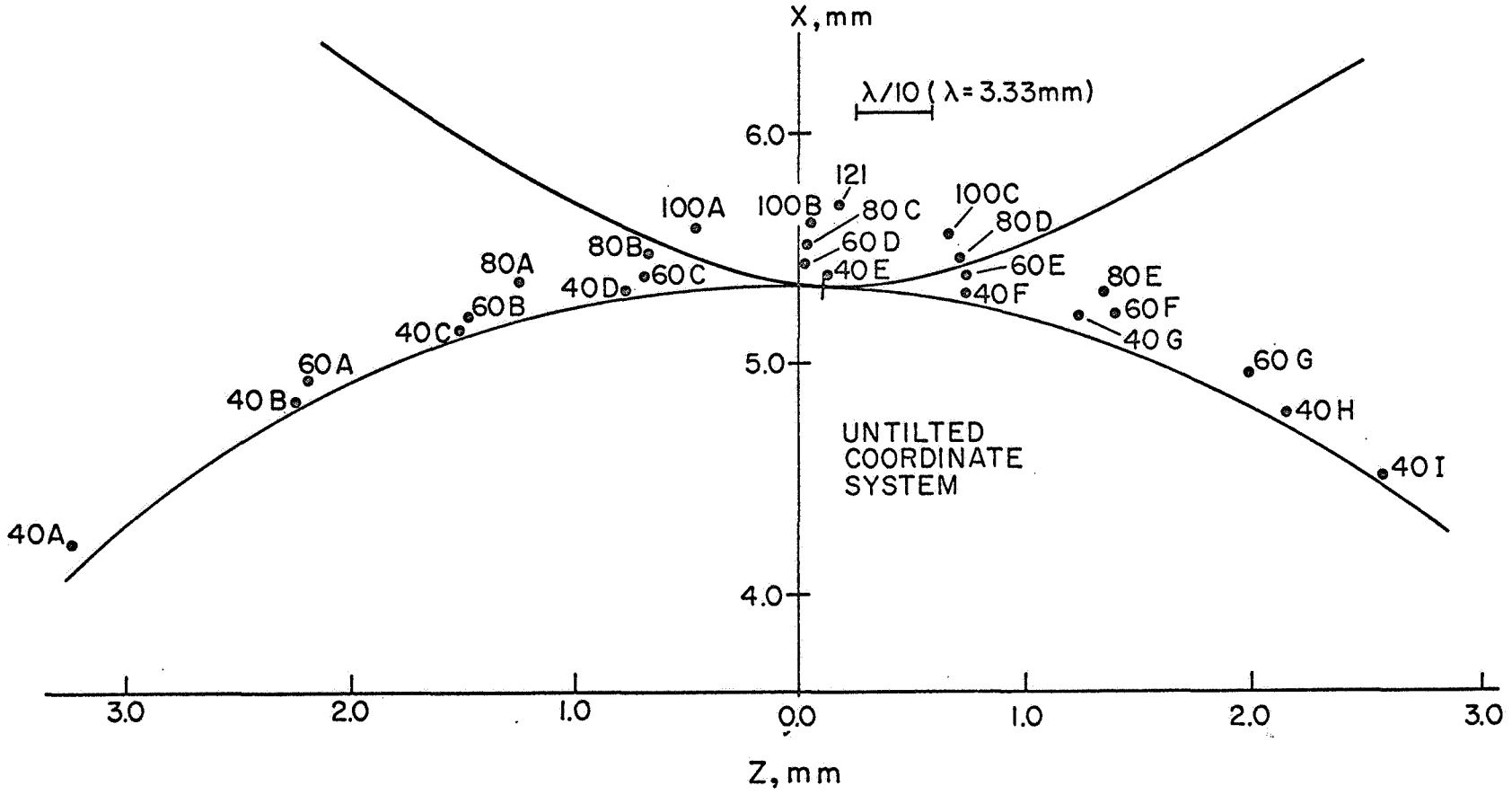

Figure 3-13. Positions of differential phase centers relative to the caustic curves for small portions of the physical optics field with $D/\lambda = 59.54$.

field is in a direction normal to the untilted axis, from F to 0 in Figure 3-14. In the case of geometrical optics in the symmetric case, spheres centered at F will be surfaces of constant phase; and in a vector diffraction theory solution to the symmetric scattering problem, F will be considered the best-fit phase center of the scattered field. In a similar way, point 0, located at 90^{o} from the symmetric axis (z-axis) will be considered the center of best-fit circles upon which the phase is constant in a least-squares sense, for the asymmetric case. The geometrical interpretation is then that the phase on circle S' (centered at F) varies directly as the distance between the two intersecting spheres S' and S'' centered at F and 0. Figure 3-14 shows a cross-section of two intersecting spheres in the plane of incidence of the spherical wave illuminating the tilted hyperboloid. Referring to Figure 3-14,

F = phase center of un-tilted hyperboloid; i.e., phase center for symmetric case

0 = least-squares phase center for tilted hyperboloid; i.e., that point about which the difference between the actual phase of the scattered field on a circle centered at that point and a constant, is assumed to be a minimum in a least-squares sense

a = lateral deviation of phase center upon tilting hyperboloid; assumed to be at 90^{o} from the z-axis

P = field point; on a circle of constant radius but non-constant phase centered at F

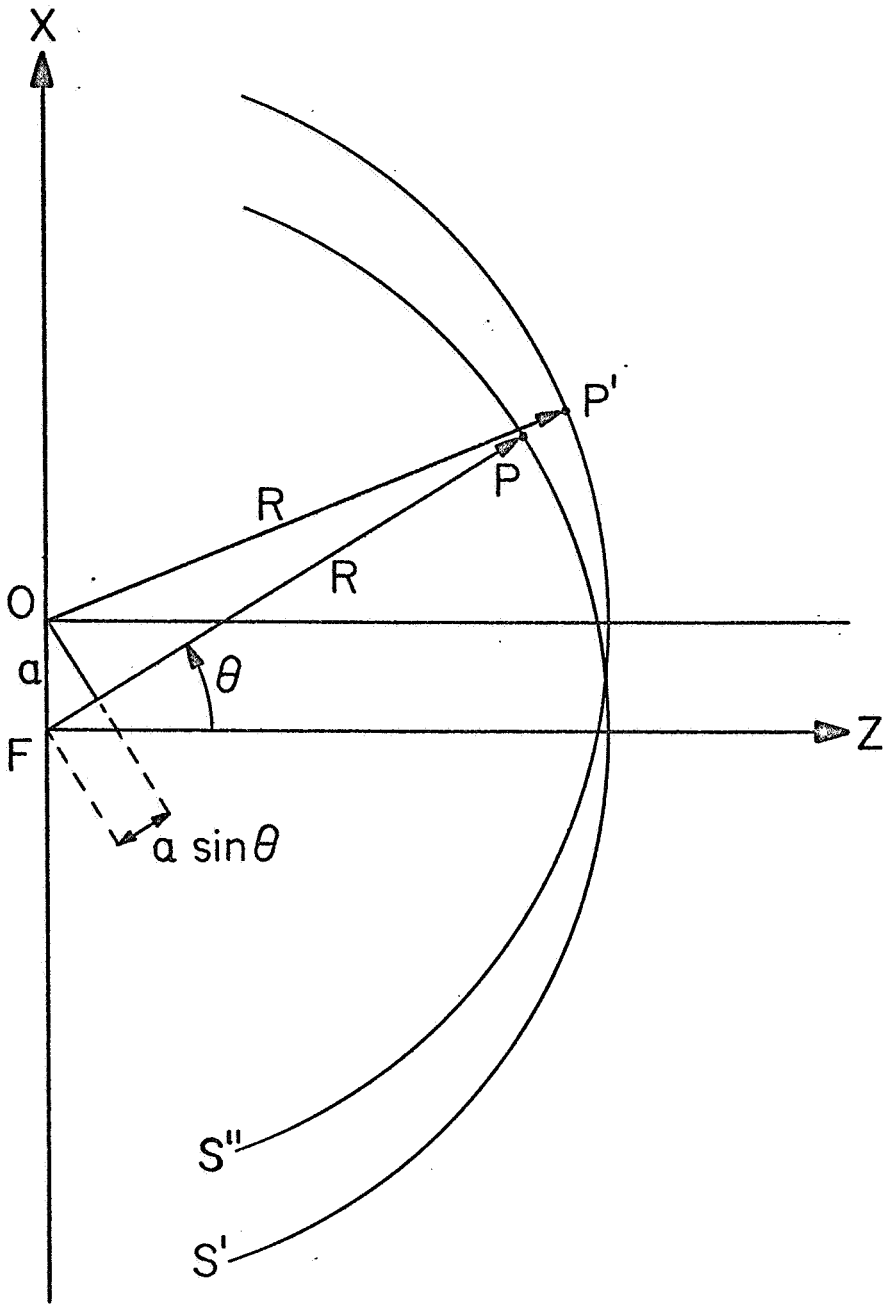

Figure 3-14. Geometry for intersecting circles determination of phase center.

P' = point on a circle of constant radius and constant phase centered at 0

R, θ = coordinates of field point P

S' = circle upon which the phase in the tilted case is not constant in any sense; centered at F. Phase is obtained from computed results in scattering calculations.

S'' = circle upon which phase is assumed to be constant, in the least squares sense; centered at 0

R = radii of circles centered at F and 0; same radius for both surfaces

$\delta(\theta)$ = phase difference in fractions of a wavelength between points P and P'

For $R \gg a$, $R - a \sin\theta = R - \delta(\theta)$.

Therefore, $\delta(\theta) = a \sin\theta$ (3-33)

Thus, knowing the computed phase on surface S' allows one to easily determine a from a plot of $\delta(\theta)$ vs. $\sin\theta$, under the following assumptions:

1. $R \gg a$
2. Movement of the phase center is perpendicular to the Z-axis.

Fitting a straight line to the plot of $\delta(\theta)$ vs. $\sin\theta$ yields the slope of the line (a) in degrees. The actual distance of the phase center movement may be computed from

$$a\ (\text{distance}) = \frac{a\ (\text{degrees phase})}{(360^{\circ})} \cdot \lambda$$

where λ is the wavelength used in the particular scattering calculation.

Using the diffraction-theory results for the $D/\lambda = 59.54$ case, the slope of the line is found to be 604°. For ease of computation, the actual phase $\Phi(\theta)$ is plotted rather than $\delta(\theta)$ since the important graphical value is the slope of the line rather than the values of each point; and the phase differs from $\delta(\theta)$ only by a constant. It is found, therefore that

$$a\ (\text{distance}) = (604/360) \cdot \lambda = 1.68\lambda \quad \text{at an angle of } 90^{\circ} \text{ from the z-axis}$$

The analysis presented here yields a surprisingly accurate determination of the asymmetric phase center (compared to the positions determined by other, more quantitative, methods). Clearly, the method is very straightforward; but it requires a knowledge of the phase of the scattered field at all points on a circle surrounding the symmetric phase center. When computer techniques are introduced to compute the phase of the scattered field, it might be as convenient to use the best-fit method described in Section 3.3.3. Even with the limitation of assuming a 90° movement of the phase center, the method presented here gives an accurate and quick estimate of

asymmetric phase center position.

3.3.5 Phase-Center Determination from Demagnification Formulas

The hyperboloidal subreflector in a Cassegrainian antenna system acts like a demagnifying optical system. The following rules may be applied, from Viggh (6):

(a) Transverse Source Movement: If the feedhorn is moved off-axis a distance Δ_T, its virtual image in the hyperboloidal mirror is moved a distance $\delta_T = \Delta_T/M$ off-axis in the same direction, where $M = (e+1)/(e-1)$ and e is the eccentricity of the hyperboloid.

(b) Longitudinal Source Movement: If the feedhorn is moved toward the hyperboloid a distance Δ_L, its virtual image in the hyperboloidal mirror is moved a distance $\delta_L = \Delta_L/M$, in the opposite direction.

These principles are illustrated in Figure 3-15.

The situation in the asymmetric configuration, illustrated in Figure 3-16, is slightly more complicated, although the demagnification formulas can also be applied. However, the movement of the source, $\overline{\Delta}$, and the effective movement of its image, $\overline{\delta}$, must be evaluated in the tilted (X'- Z') coordinate system. The effective phase

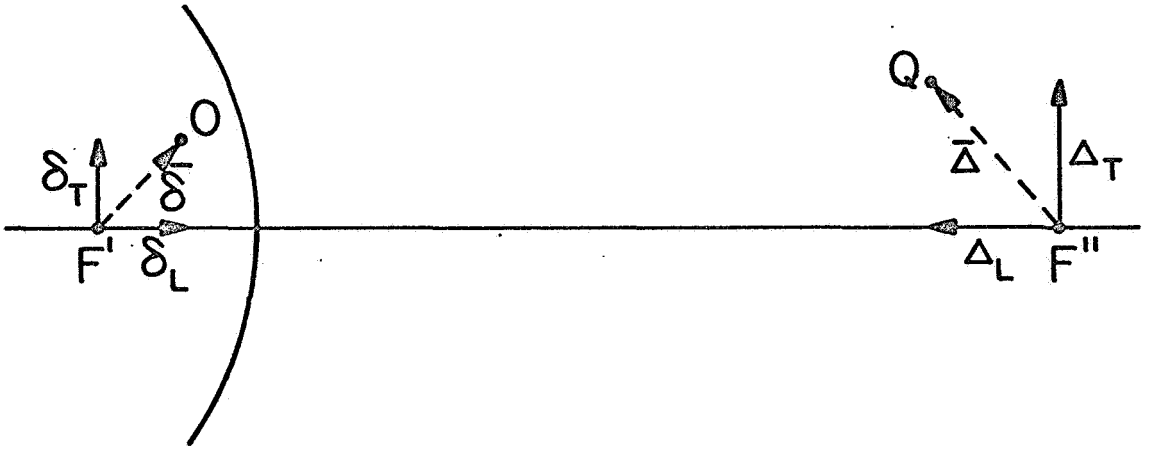

Figure 3-15. Symmetric geometry for defining optical demagnification rules.

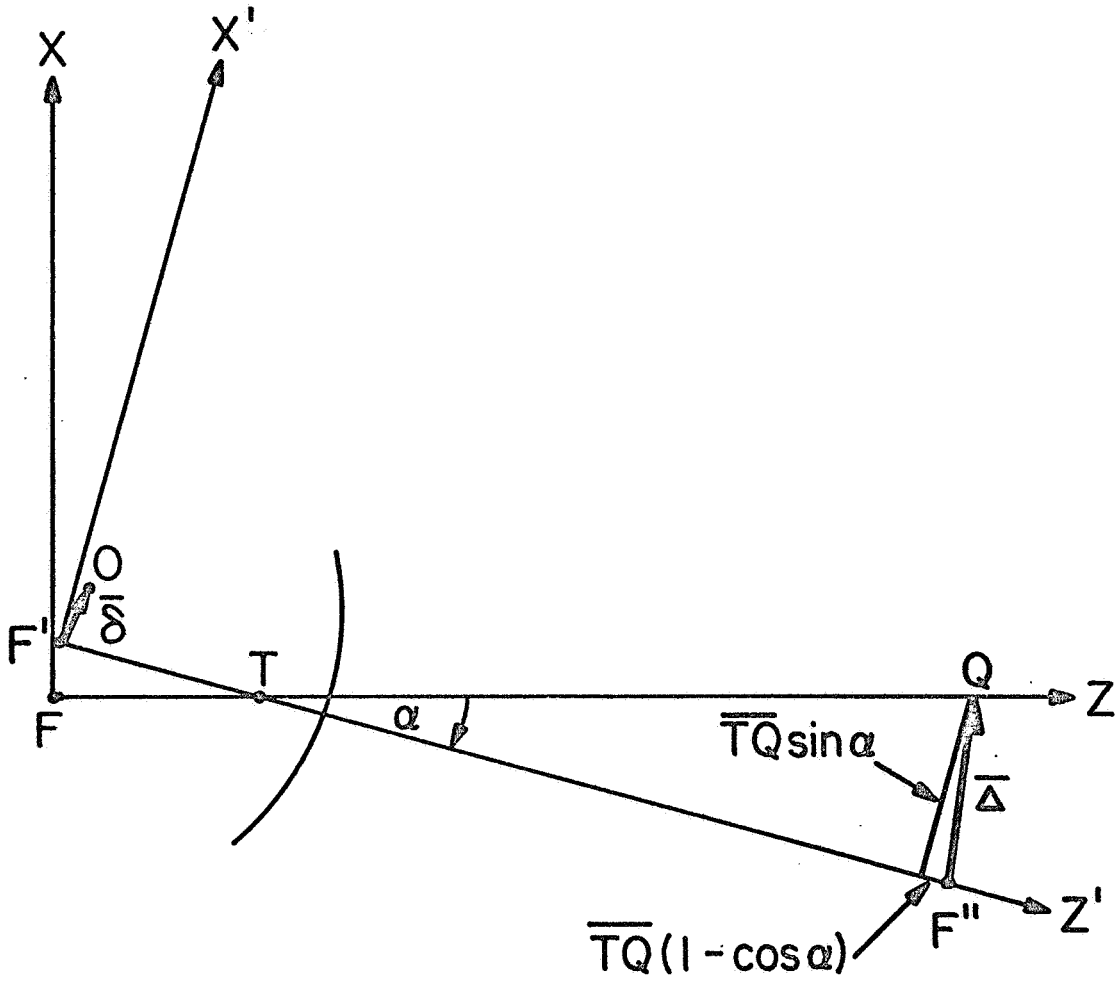

Figure 3-16. Asymmetric geometry for applying optical demagnification rules.

center of the scattered field then lies at the tip of the vector $\bar{\delta}$.

A calculation of this type has been carried out for the geometrical parameters being considered in this paper. The resulting coordinates of the phase center, when transformed into the untilted (X-Z) coordinate system, are a =5.318 mm, ψ = 87.82 deg. These values compare favorably to the results of the previous sections. The obvious advantage of this technique is that the phase center of the scattered field may be determined only from the elementary geometrical parameters of the hyperboloid. It is to be expected, however, that for more extreme tilt angles the demagnification formulas will produce less accurate results than those obtained by other means.

3.4 Summary of Results and Conclusions

The coordinates of all phase centers determined in this dissertation are shown in Figure 3-17 and tabulated in Table 3-3. Not shown in the figure is the actual physical position of the hyperboloid geometric focus (F') in its tilted position at a = 2.348 mm, ψ = 88.97 deg. It is evident that F' may not be used to approximate the phase center of the scattered field, since all the phase center positions are approximately one wavelength (for λ = 3.33 mm) further from the symmetric focus (F) than is the new position of the hyperboloid focus (F').

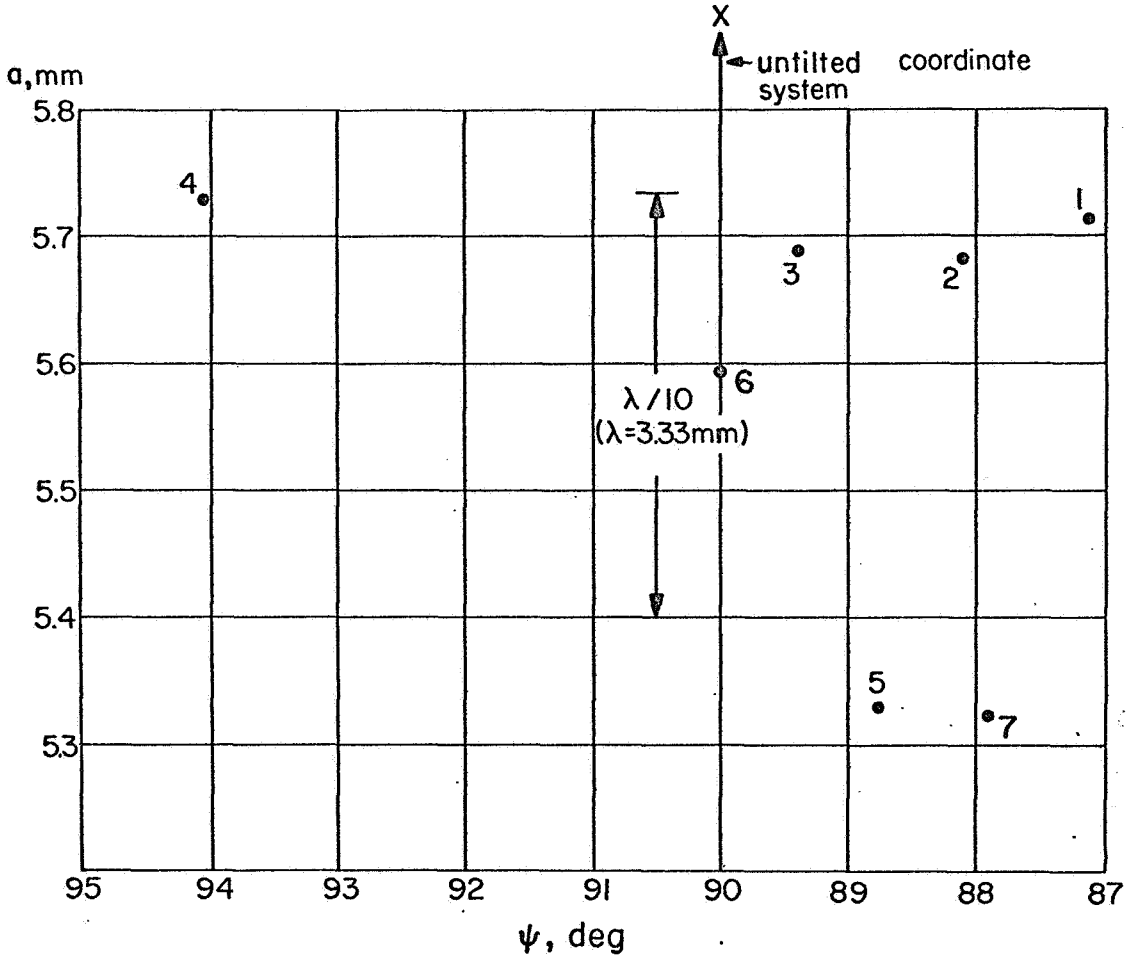

Figure 3-17. Positions of all phase centers determined in this chapter, corresponding to points listed in Table 3-3.

No.	Analysis	Radius (a), Wave-lengths	Radius (a), Milli-meters	Angle(ψ)
1	Geometrical Optics Best-Fit Weighted, 117 pts.	---	5.714 mm	87.148°
2	Diffraction Theory Best-Fit Weighted, 121 pts., D/λ = 59.54, λ = 3.33 mm	1.707λ	5.684 mm	88.108°
3	Diffraction Theory Best-Fit Weighted, 121 pts., D/λ = 24, λ = 8.26 mm	0.689λ	5.691 mm	89.373°
4	Diffraction Theory Best-Fit Weighted, 121 pts., D/λ = 10, λ = 19.83 mm	0.289λ	5.731 mm	94.041°
5	Intersection of Caustic Curves	---	5.321 mm	88.755°
6	Intersecting Spheres D/λ = 59.54, λ = 3.33 mm	1.68 λ	5.594 mm	90°
7	Application of Demagnification Formula D/λ = 59.54, λ = 3.33 mm	1.595λ	5.318 mm	87.82°

Table 3-3

(cf. Figure 3-17)

It is of interest to develop relationships between the angle of the phase center movement and the net movement of the antenna beam in a complete Cassegrainian system. In Figure 3-18, where the source Q has been chosen to lie at the vertex of the paraboloid, the angle of antenna beam movement is defined as τ, and the angle of phase center tilt (as seen from the source Q) is defined as β. For the nodding subdish system

$$\tau = 27.75 \text{ min arc (experimental)}$$

$$\beta = \tan^{-1}(\overline{FO}/\overline{FQ}) = \tan^{-1}(0.224''/25.6'') = 30.08 \text{ min arc}$$

$\overline{FO}$ is the movement of the $D/\lambda = 59.54$ best-fit phase center. The ratio becomes

$$\tau/\beta = 0.924$$

A ratio of less than one is expected and has been discussed in the literature by Lo (24) and Sandler (25). Following Lo, a Beam Deviation Factor (BDF) is defined as the ratio of the beam deflection angle (τ) to the angular displacement of the feed (β), both measured from the axis of a paraboloidal reflector with the vertex as origin. For a paraboloid F/D ratio (focal length/diameter) of 0.427 (the nodding subdish system), a BDF of 0.887 is predicted from theoretical considerations. For a phase center position defined by the $D/\lambda = 59.54$ best-fit phase center, the feed offset is 0.501^{o}. A predicted

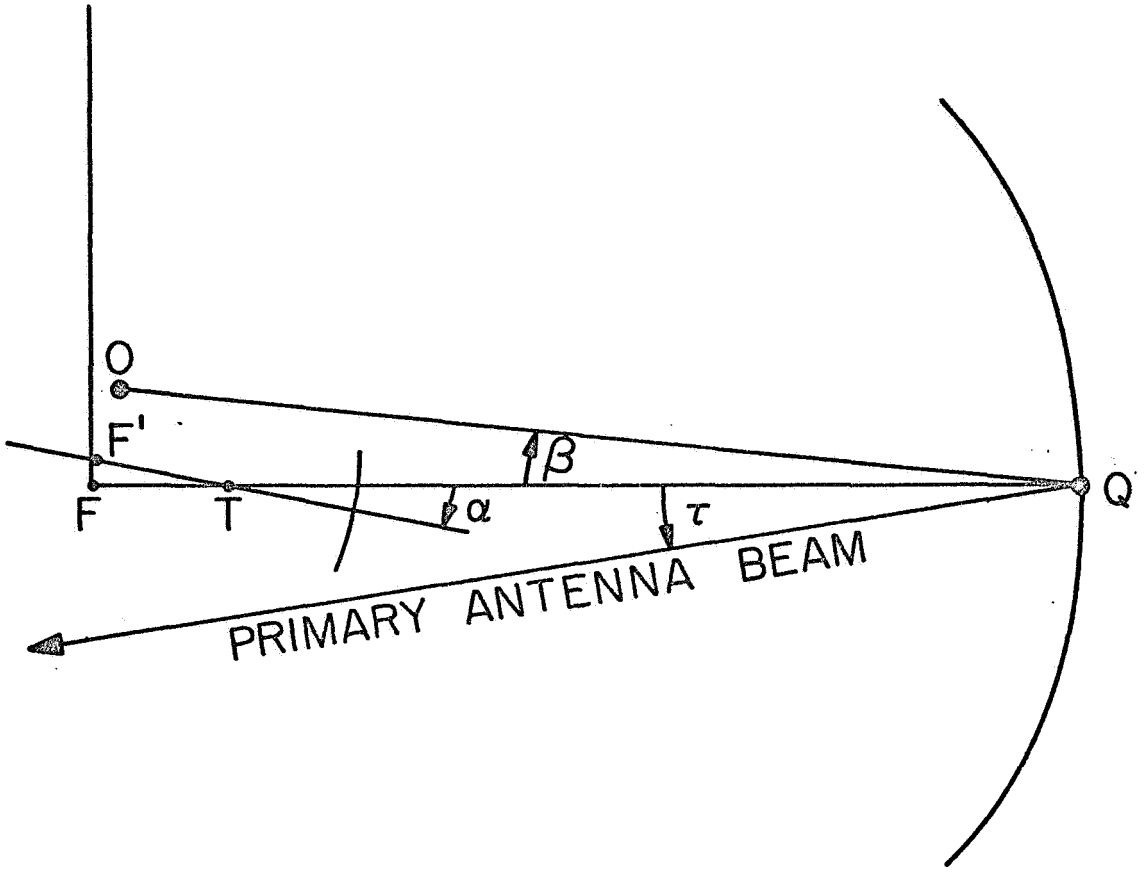

Figure 3-18. Illustration of the relationships between phase center movement (β) and resulting displacement of the primary antenna beam (τ).

beam deflection of 0.444^{o} (0.887×0.501^{o}) is found, which compares favorably with the experimental value of 0.463^{o} (27.75 min arc). The difference is 0.019^{o}, or 1.14 min arc.

To a first order approximation, standard formulae, as in Isber (26) and Reed (27), for beam pointing calculations define the beam tilt due to a displaced focal point (for small angles) as

$$\theta_t = \frac{\text{focal pt. movement}}{\text{focal length of paraboloid}} \qquad (3\text{-}34)$$

$$= (0.224''/25.6'')$$

$$= 0.00875 \text{ radians} = 30.08 \text{ min arc}$$

This agrees within ten percent of the experimental value of 27.75 min arc.

Several conclusions may be drawn from the studies carried out in this chapter:

1. The geometrical focus F' of the hyperboloid may not be regarded as the phase center of the field scattered from a tilted hyperboloid. For the particular case in which $D/\lambda = 59.54$, it was found that the best-fit phase center was approximately one wavelength from the position of the geometrical focus of the hyperboloid.

2. For D/λ ratios as low as 10, it was found that physical

optics and geometrical optics determinations of best-fit phase center agree to within approximately 1/10 wavelength or better. The actual phase center positions are independent of the value of D/λ, for the small number of cases considered, $D/\lambda > 10$, and a specific geometry.

3. For moderate tilt angles, the phase center position may be determined for a first approximation by either the geometrical-optics method (cf. Section 3.3.2) or the demagnification formula (cf. Section 3.3.5). Accuracy is good to within 0.1 - 0.2 wavelengths.

4. The relationships between phase center movement and antenna beam-tilt (cf. Section 3-4) give relatively accurate (within 3-10%) values of antenna beam-tilt when the phase center position is accurately known. For a more accurate beam-tilt determination, a complete diffraction theory analysis of electromagnetic wave scattering from the paraboloid must be carried out.

Chapter 4

INSTRUMENTATION

4.1 Nodding Subdish Description and Performance

The nodding subdish mechanism is located at the vertex of the tripod structure shown in the photograph of the 90-GHz radio telescope in Figure 4-1. The position is identical with that of the previously used non-tilting hyperboloidal subreflector.

While operating, the nodding subdish moves between two off-axis positions, symmetric with respect to the centerline of the operating mechanism (Figures 4-2 through 4-6). The axis about which the subdish moves may be indexed to give movement in any desired direction. For radio-astronomical applications, it was determined that the optimum switching direction was up-down for a polar mounted antenna pointing south. As the antenna was swung to the east or west, the switching direction would become more horizontal and the difference in antenna beam elevation would be minimized. This would insure as constant an atmospheric path length as possible during on- and off-source measurements.

Provision is also made for focussing the subdish by means of an internal motor, gear drive, and lead screw. Located on the back of the subdish are a small cam follower and two small bearings.

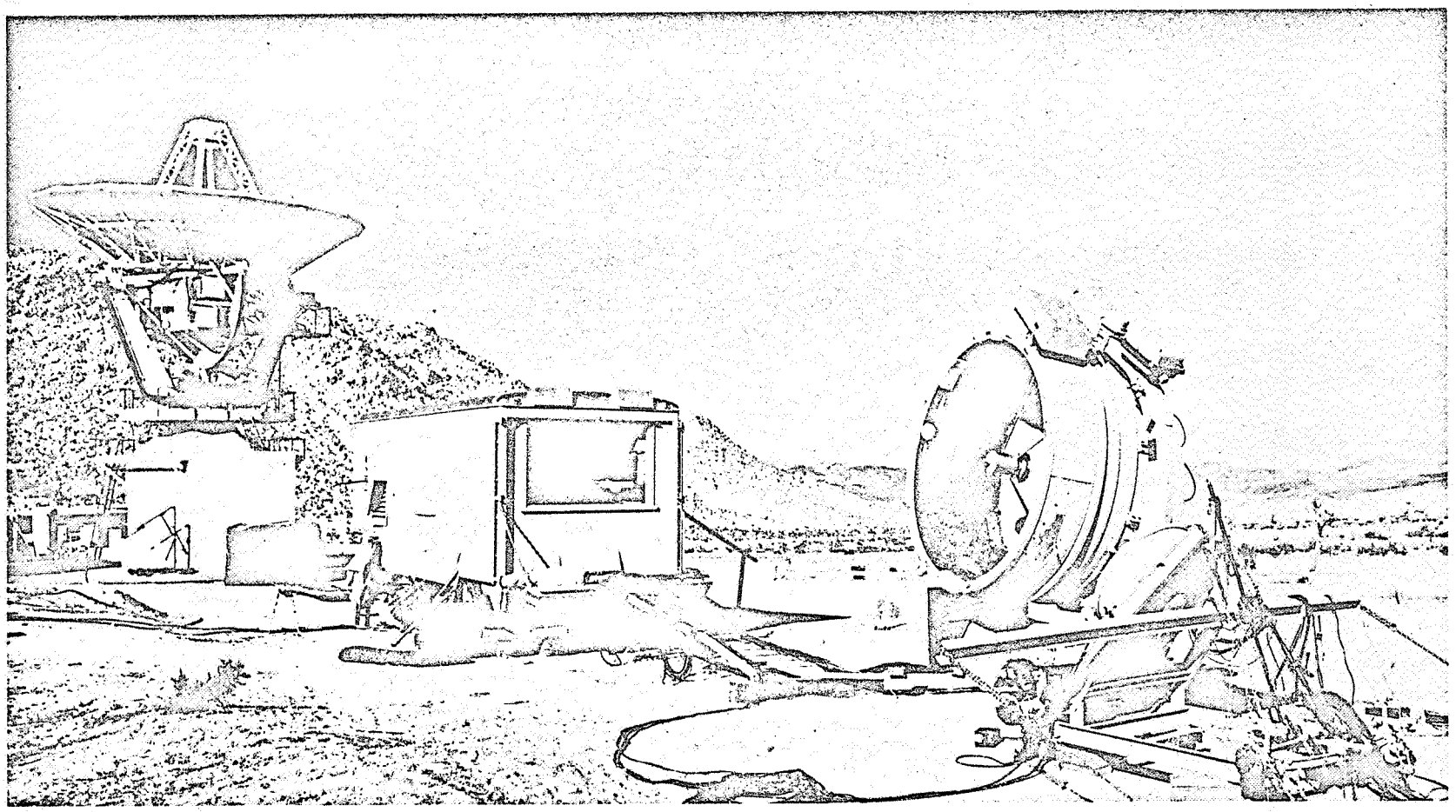

Figure 4-1. 90-GHz radio telescope at the JPL Goldstone Tracking Station (instrumentation trailer and 30-foot antenna in background).

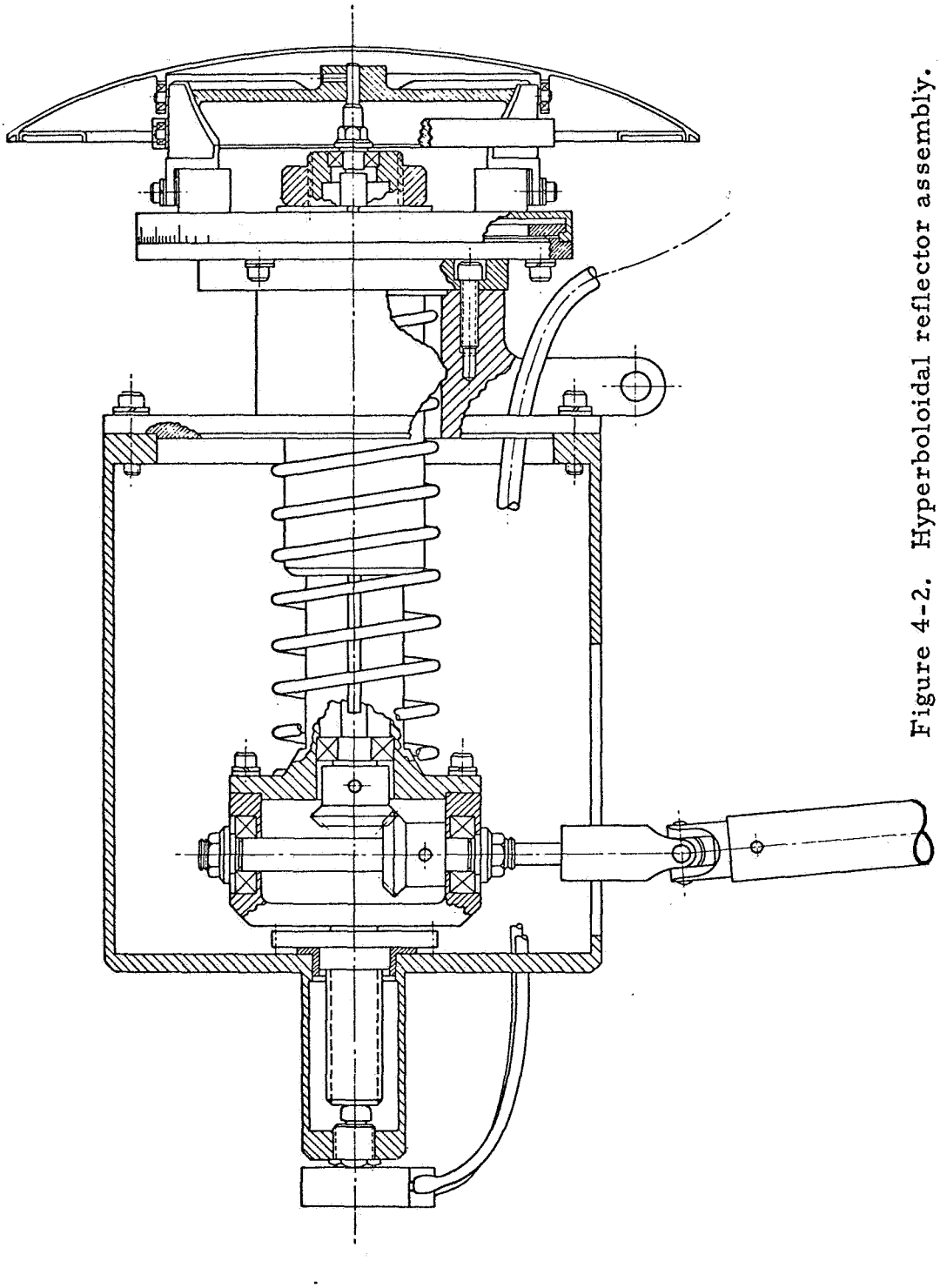

Figure 4-2. Hyperboloidal reflector assembly.

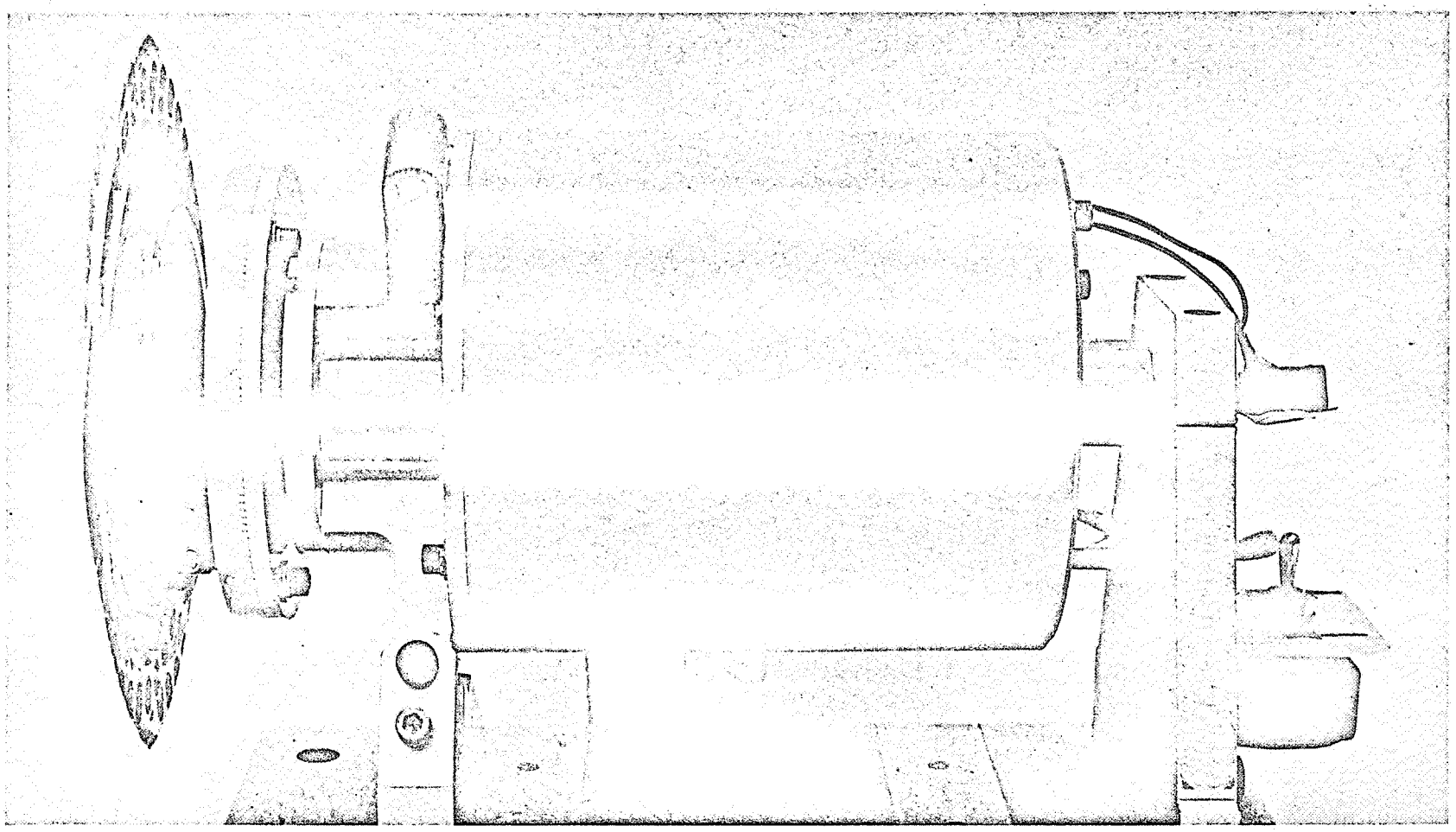

Figure 4-3. Side view of nodding subdish assembly showing extremes of mirror motion during a switching cycle.

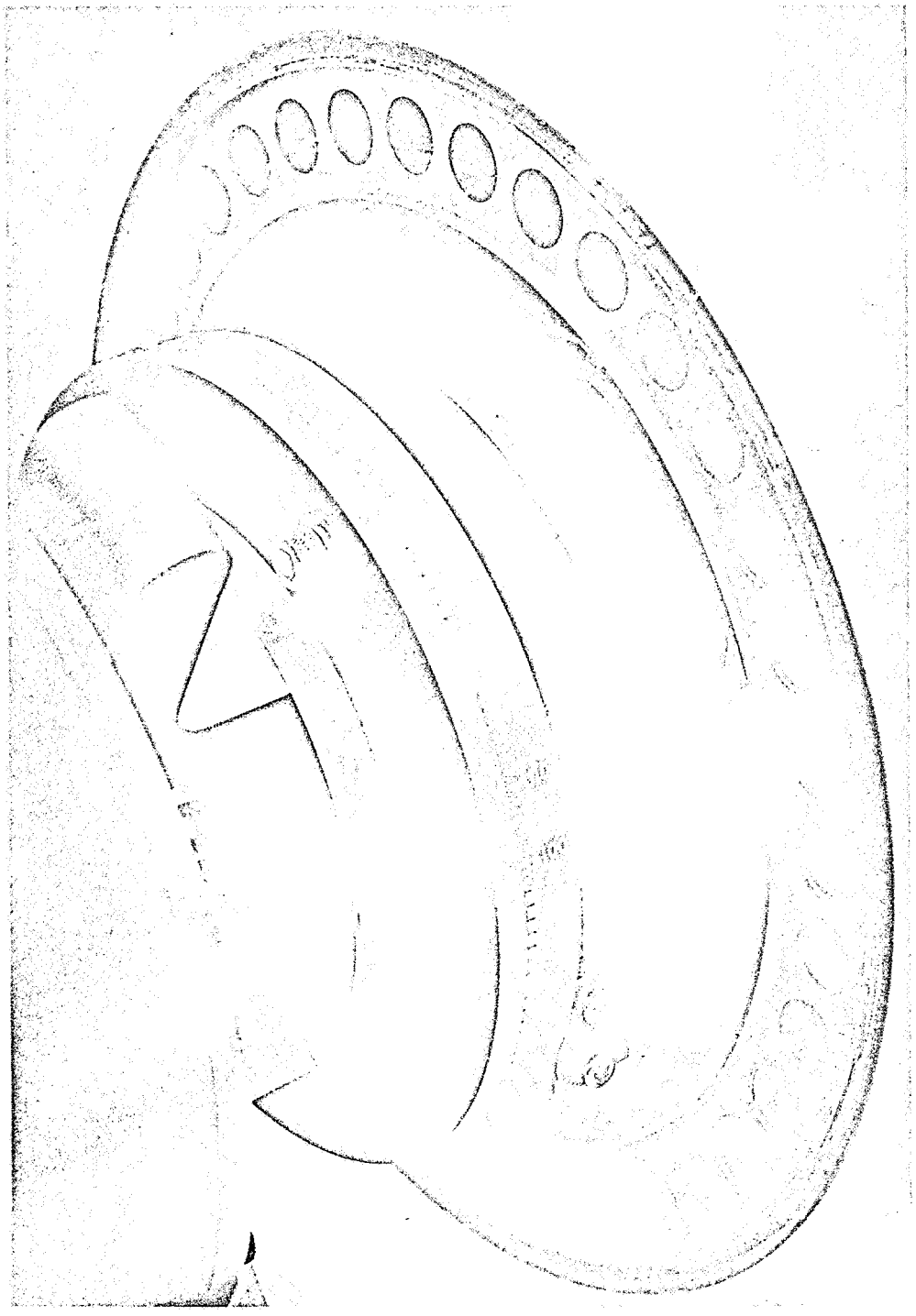

Figure 4-4. Back view of subdish assembly showing mirror stiffening ring, bearing holders, cam follower, cam wheel, counterweight, indexing plate, and tripod head.

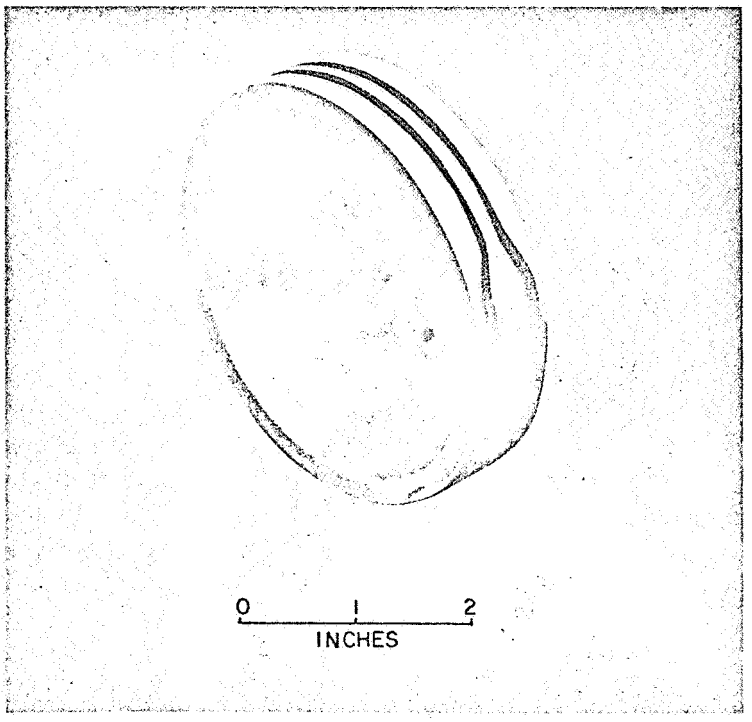

Figure 4-5. Cam wheel showing symmetrical cam tracks.

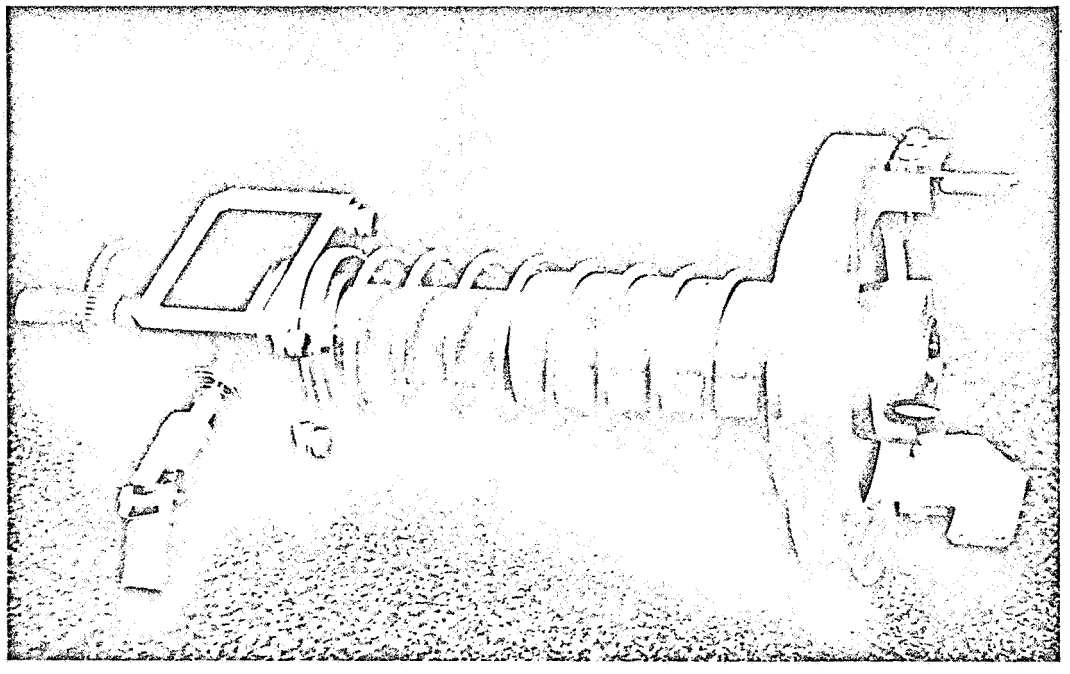

Figure 4-6. Focussing and drive unit showing universal joint for external drive, miter gear housing, focussing screw and gear, indexing plate, and bearing holders.

Located on the circular counterweight are a similar cam follower and similar bearings. The four bearings fit into a holder in a fixed position with respect to the adjustment plate. The cam followers fit into a two-track cam wheel which is driven by an external motor.

Rotation of the cam wheel causes approximate "square-wave" motion of both the subdish and the counterweight. The subdish remains in one off-axis position for about forty-five percent of the rotation of the cam wheel, switches for five percent of the rotation, remains in the second position for forty-five percent of the rotation, and then switches back to the first position during the remaining five percent of the cam wheel rotation.

An extensive series of mechanical tests was made to determine possible operating frequencies for the subdish mechanism, since the mechanical problems would be the limiting factors in system performance. Although operation of the subdish mechanism was made at rates as high as 8 switching cycles per second, it was felt that this was mechanically punishing to the relatively delicate mechanism, which would have to operate for several million cycles without failure or repair. It was decided, after extensive electronic tests also, that 2.7 cycles per second was a good compromise for optimum mechanical and electronic operation. High frequencies (greater than 5 cycles per second) were poor from a mechanical standpoint, and low frequencies

(less than 2 cycles per second) were poor from an electronic standpoint.

4.2 Antenna Characteristics

Antenna pattern measurements were taken using the tilted hyperboloid in one stationary position, tilted 2.06° from its symmetric position (axis of hyperboloid colinear with axis of paraboloid). The total excursion from one extreme of tilt to the other is 4.12°. The total antenna beam shift between extremes is 55.5 minutes of arc. Hence the deviation of the beam from its symmetric position is 27.75 minutes of arc.

Figures 4-7 and 4-8 show the static antenna patterns measured with the subdish tilted to its 2°-off-axis position. Comparison of these patterns with the patterns measured for the symmetrical geometry (3) does not reveal significant abberations such as excessively high sidelobes or excessive beam broadening. The 1966 symmetric case measurements indicated a 3-dB beamwidth of 10.5 minutes of arc, with a different feedhorn (dual-mode feedhorn). The most recent measurements (November 1967) indicate that the 3-dB beamwidth in the east-west plane is 12.2 minutes of arc, and in the north-south plane is 9.7 minutes of arc. This asymmetry and beam broadening in an asymmetric geometry was expected and has been predicted in the literature (21, 25). No appreciable coma (usually

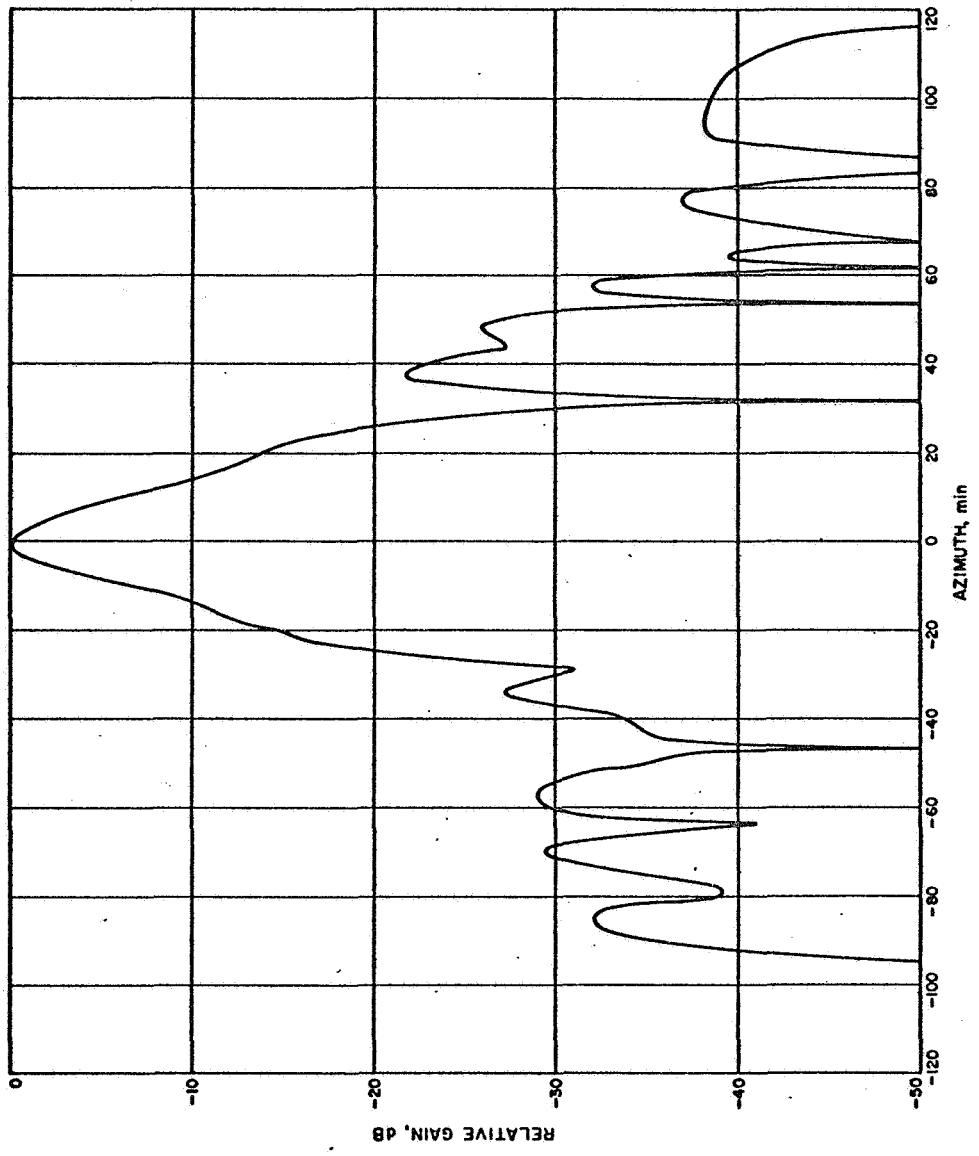

Figure 4-7. Azimuth antenna pattern, tilted hyperboloid.

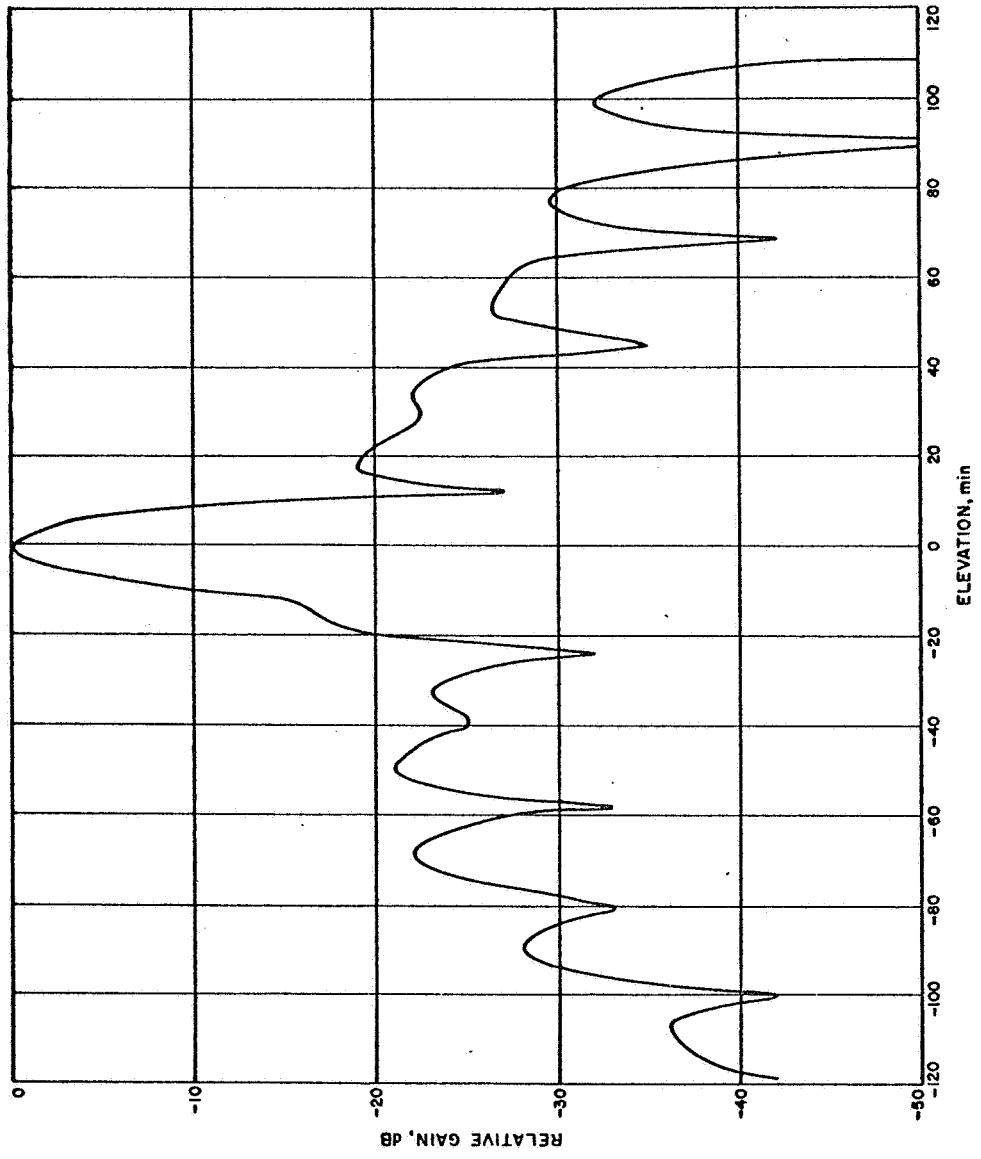

Figure 4-8. Elevation antenna pattern, tilted hyperboloid.

introduced by feed displacement normal to the axis) is introduced by tilting the hyperboloid, as evidenced by the fact that the antenna patterns remain relatively symmetrical, although offset approximately $\frac{1}{2}^{o}$. A slightly astigmatic condition (usually introduced by feed displacement parallel to the axis) is present as indicated by the slight beam broadening in the plane normal to the plane of tilt.

In a beam-switching synchronous detection scheme, it is necessary that very little source signal appear in the reference, or off-source, beam. The sidelobe level of the reference beam is down approximately 33 db (.05%) at the position corresponding to the location of the primary beam.

4.3 Radiometer Description

The 90-GHz radiometer used in the nodding subdish system was operated in a synchronous detection mode at a switching rate of 2.7 cycles per second, i.e., the subdish switched the beam back and forth in the sky at the switching rate, and the net RF signal in phase with a 2.7-Hz radiometer reference signal was synchronously detected. A block diagram and photograph of the RF portion of the radiometer are shown in Figures 4-9 and 4-10. A block diagram and photograph of the electronic system are shown in Figures 4-11 and 4-12.

The subdish drive mechanism not only operates the subdish but also creates a square wave electrical signal for use as a radiometer

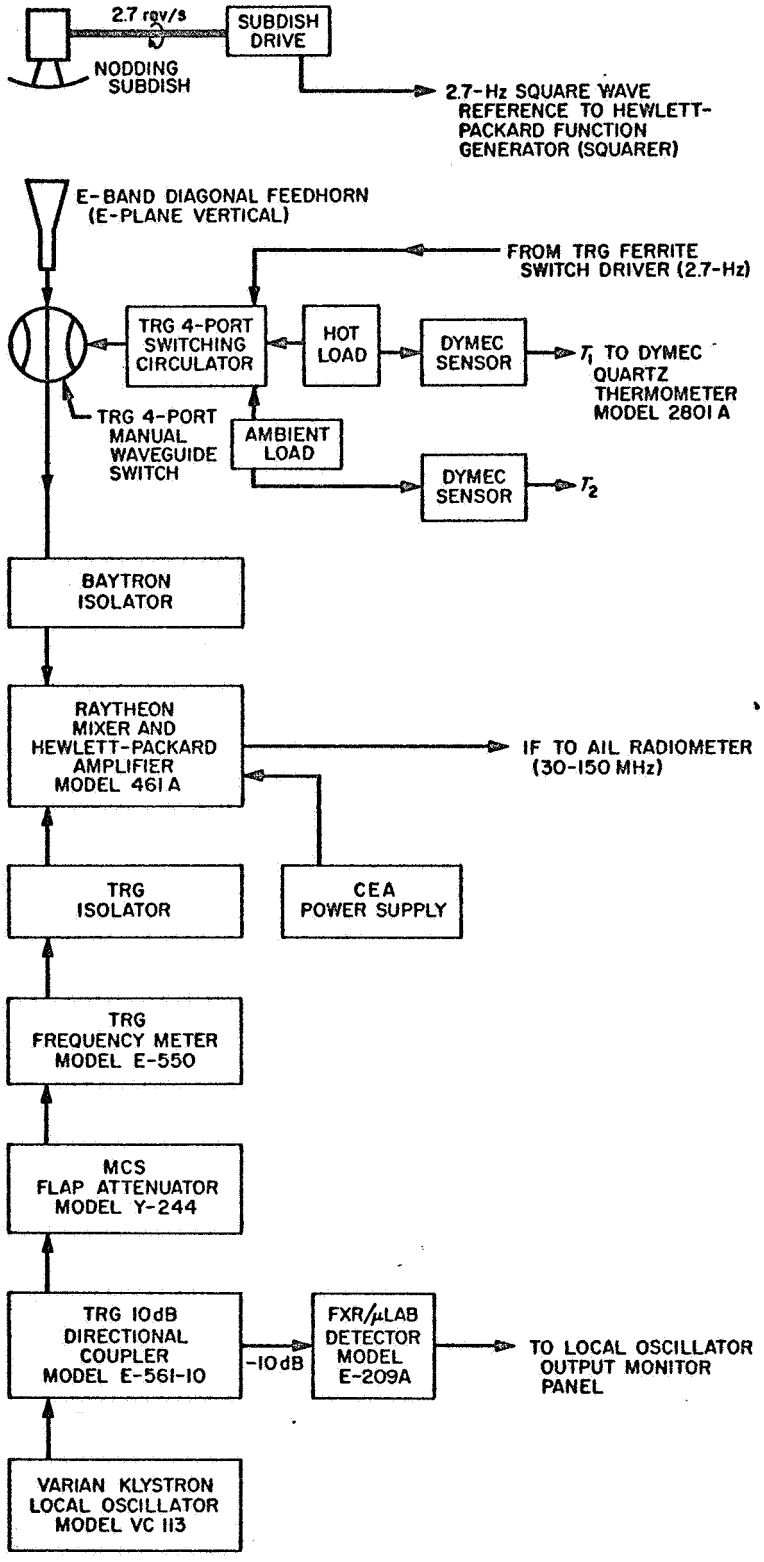

Figure 4-9. Block diagram of RF portion of nodding subdish system.

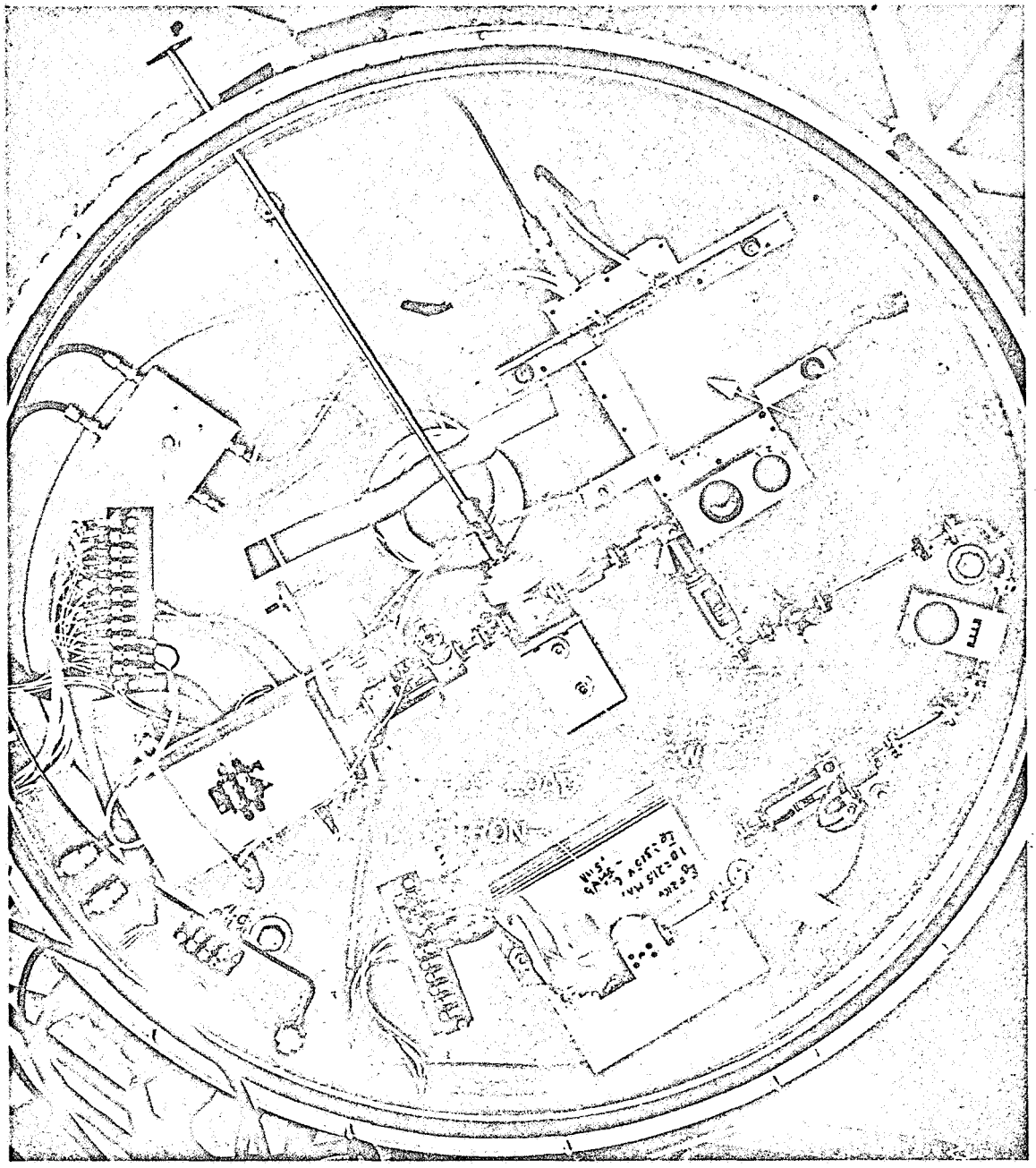

Figure 4-10. Photo of RF portion of nodding subdish system, showing radiometer in position on back of antenna.

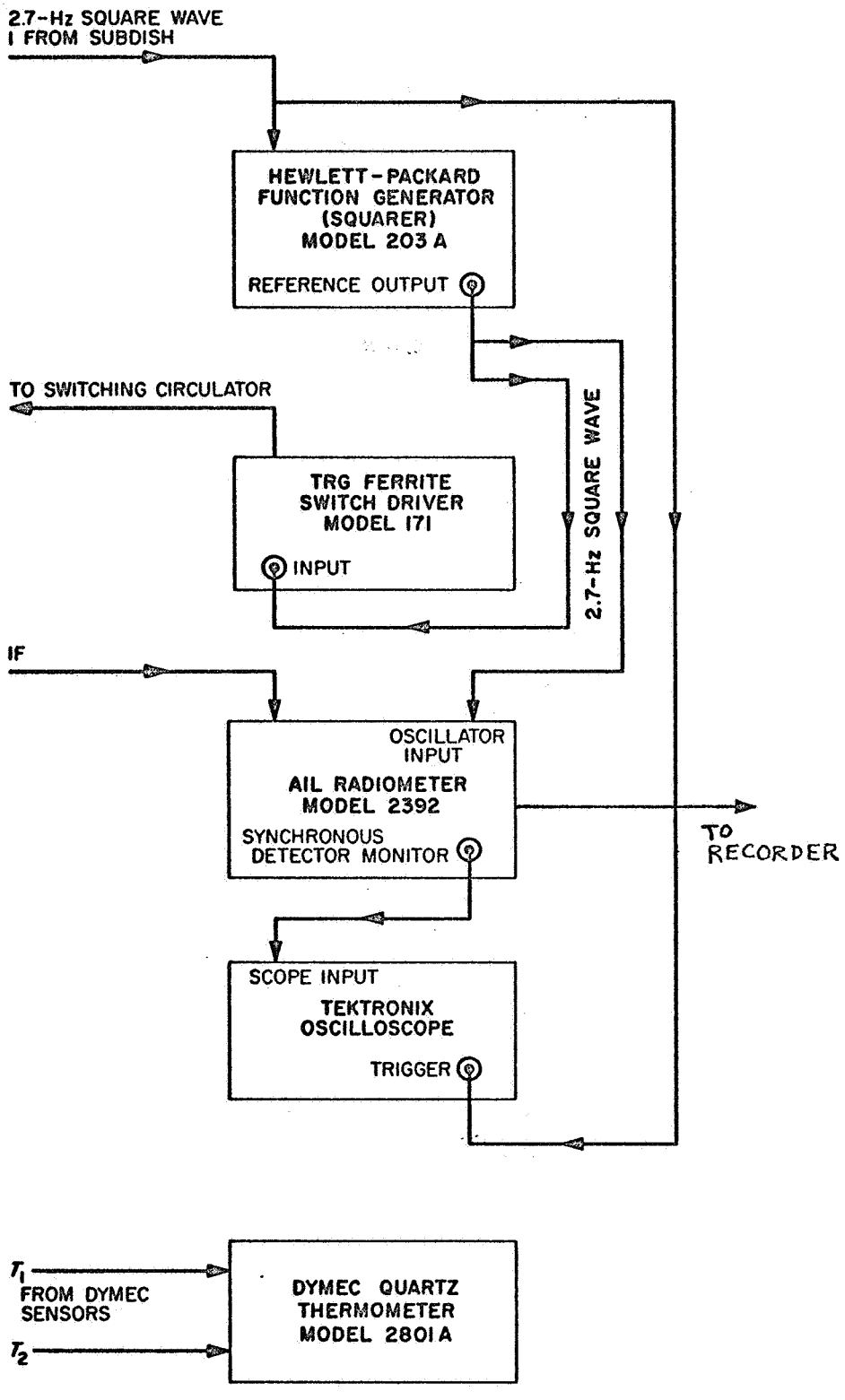

Figure 4-11. Block diagram of electronic portion of nodding subdish system.

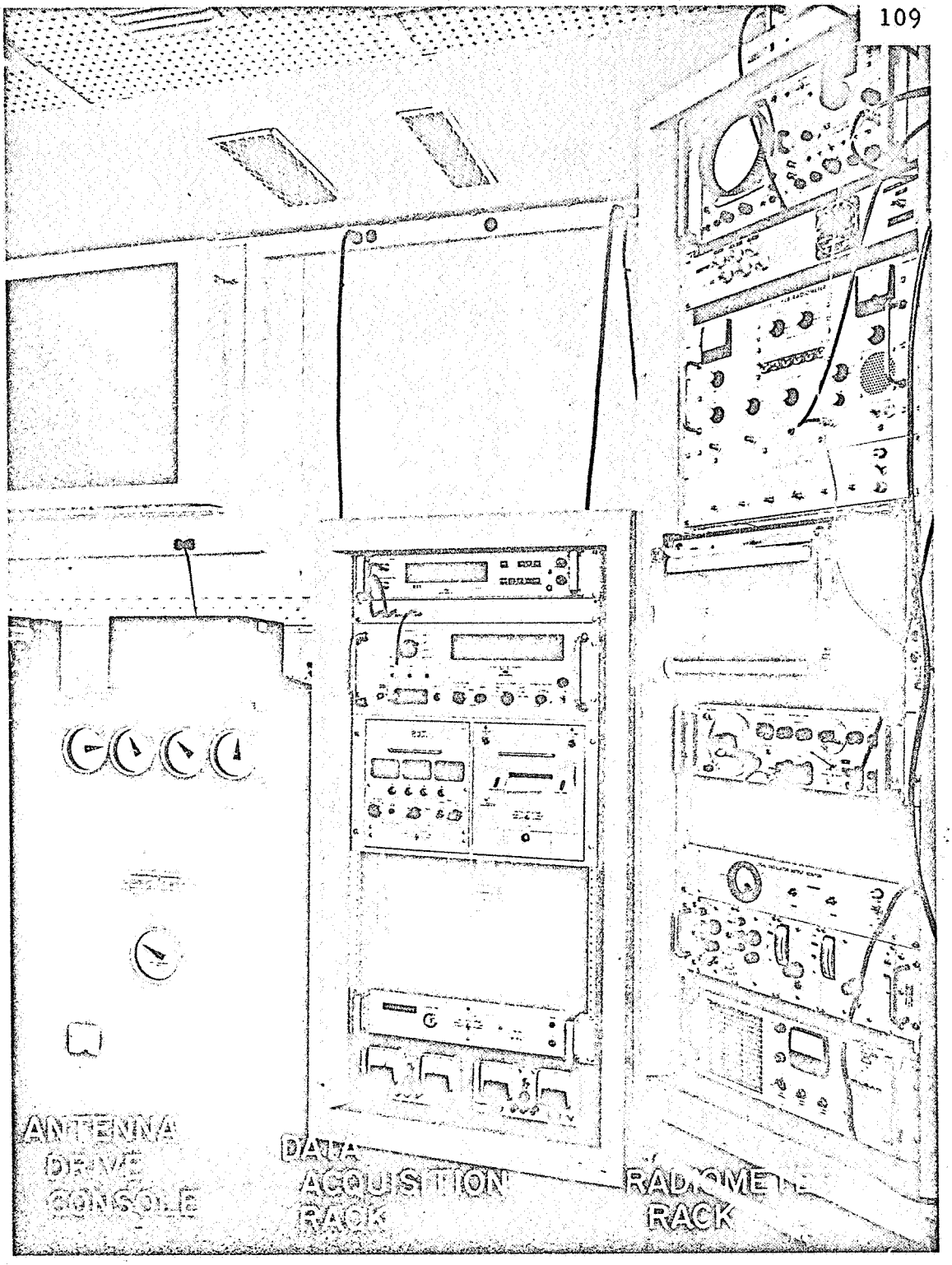

Figure 4-12. Photo of electronic portion of nodding subdish system, showing equipment racks in instrumentation trailer.

reference input. The square wave signal is obtained by chopping a light beam with a rotating slotted wheel. This wheel may be rotated with respect to the drive shaft to adjust the phase relationship between subdish movement and radiometer reference. Testing indicated that the optical sensor in the drive mechanism did not give a perfectly "square wave," and this would not switch the AIL radiometer properly. A Hewlett-Packard function generator was modified to receive the reference signal, square it, and present it to the AIL radiometer in a form suitable for proper operation. This square wave is also used as input to the ferrite switch driver, and switches the hot-load signal at the synchronous frequency during calibration measurements.

The signal line from feed horn to mixer was made as short and direct as possible, to reduce signal loss.

The diagonal feedhorn is an improvement over the original dual-mode feedhorn and matching iris utilized in earlier systems. Since Cassegrainian optics are used in the antenna, where the feedhorn illuminates the hyperboloidal subreflector, it is highly desirable that the feedhorn have an axially symmetric pattern, a relatively narrow beam, and low sidelobes to minimize forward spillover. The matching iris in the original feedhorn resulted in a horn with narrow frequency bandwidth performance. Currently available 90-GHz

klystrons, one of which is used in the radiometer as a local oscillator, are not well frequency-stabilized. The resulting frequency instability in a narrow-band RF front end leads to degradation of radiometer gain and sensitivity. Consequently, it was felt desirable to incorporate a different feedhorn configuration in the radiometer. The design selected was the diagonal-horn type (20). The horn (Figures 4-13 and 4-14) consists of three regions: an E-band waveguide region with flange, a transition region, and a long tapered region with rotated square cross section. The completed unit was gold-flashed. The measured VSWR was less than 1.05 over a frequency range of 89.60 to 90.30 GHz.

The only other two items in the signal line were a TRG Model E 530 manual four-port waveguide switch and a Baytron isolator having a very low insertion loss (approximately 0.4 dB). The mixer is a Raytheon Model WR 10 balanced mixer.

The hot-load calibration line consisted of the heated waveguide termination, a TRG Model E 162 switching circulator, the four-port waveguide switch, and the Baytron isolator. Both the hot load and the ambient load were fitted with Dymec quartz crystal oscillators, which enabled the load temperatures to be measured to an accuracy of about 0.01 ^{o}K. The calibration technique is described in Section 5.2.

The local oscillator line consisted of a Varian Model VC 113

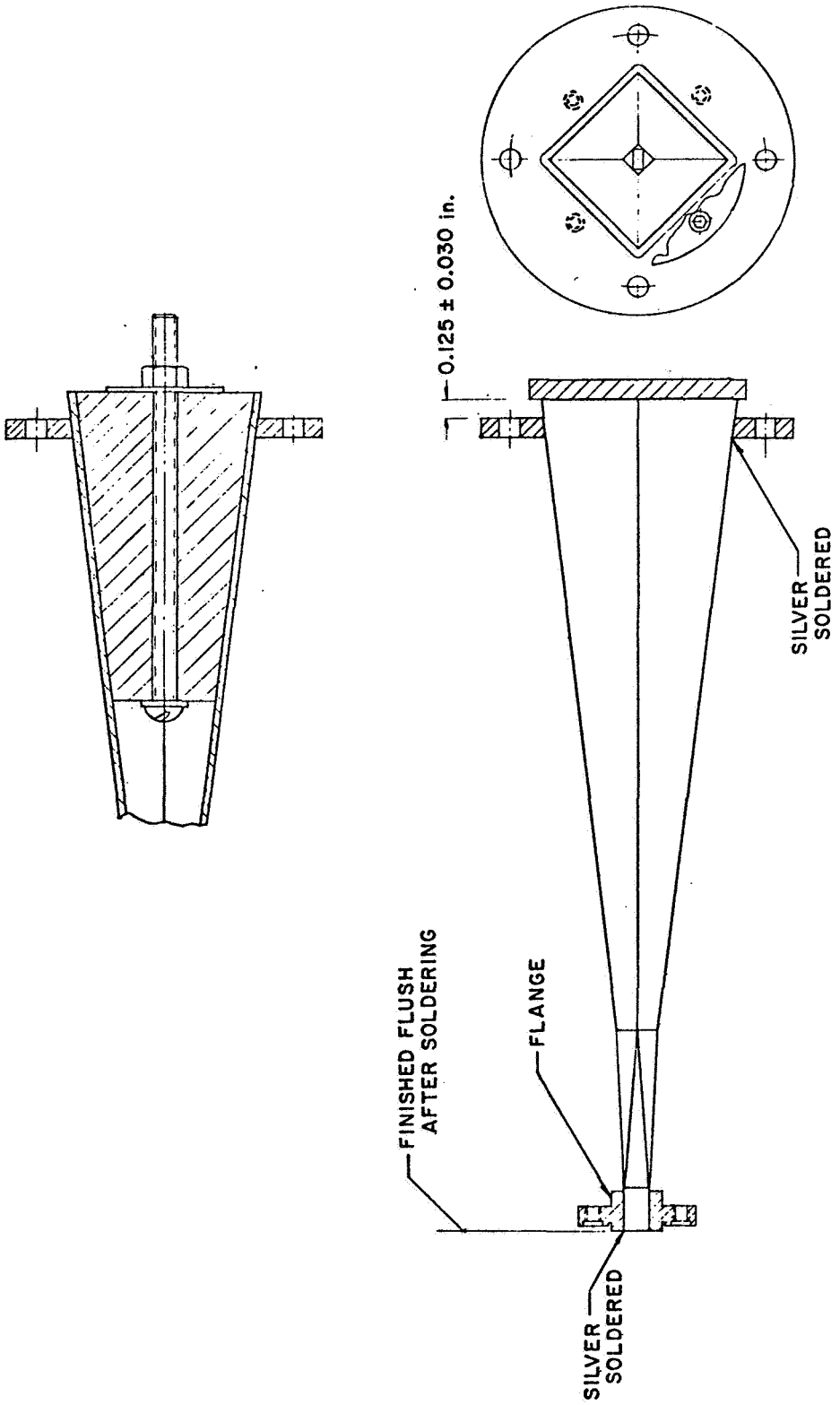

Figure 4-13. Diagonal feedhorn used in nodding subdish system.

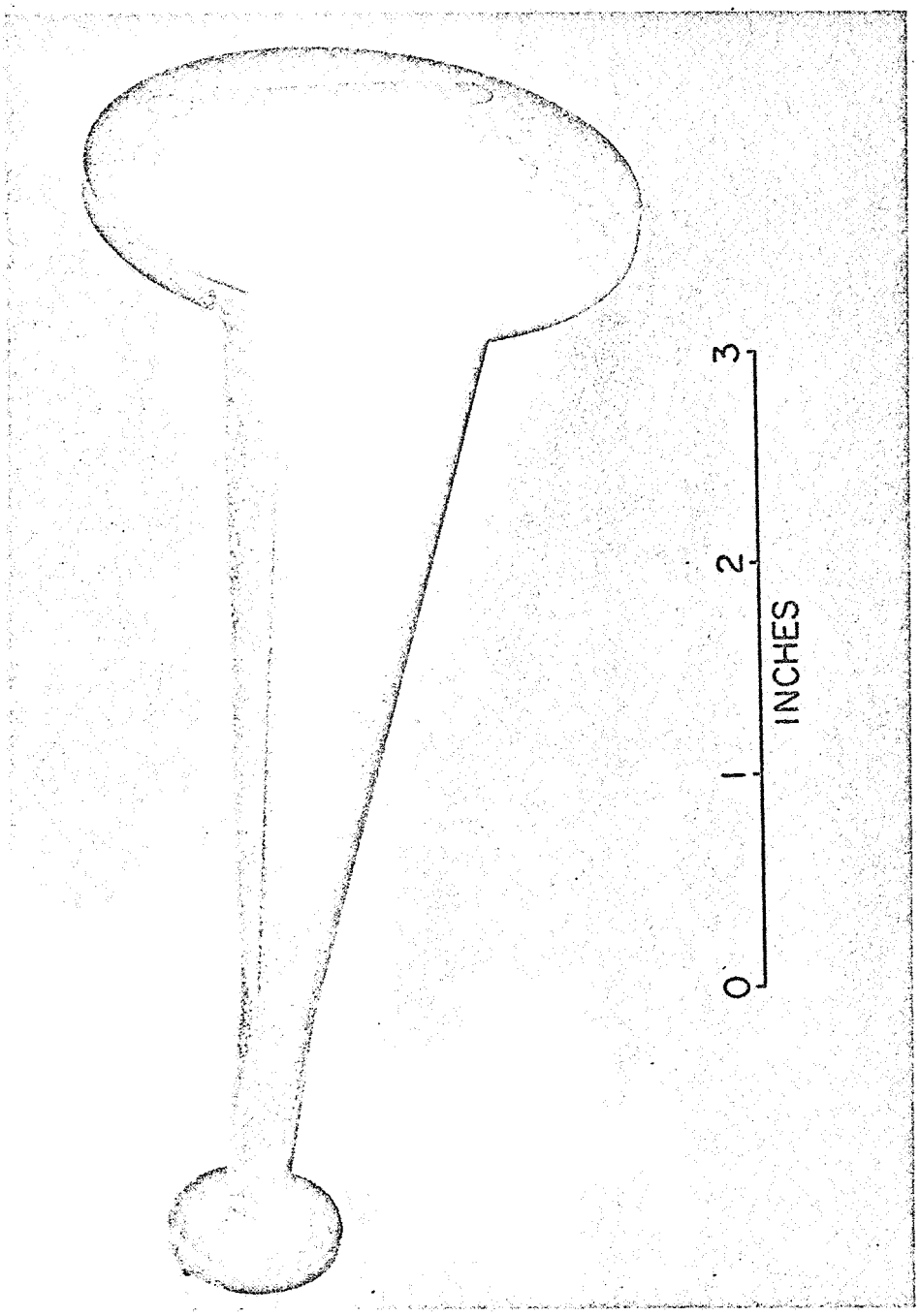

Figure 4-14. Diagonal feedhorn used in nodding subdish system.

klystron, a TRG Model E 561 10-dB directional coupler, an MCS Model Y-244 flap attenuator, a TRG Model E 550 frequency meter, and a TRG Model E 110 isolator.

The electronic system consisted of an AIL Type 2392 universal radiometer, a TRG Model 171 ferrite switch driver, a Hewlett-Packard Model 203A function generator (used for squaring the subdish reference signal), a Dymec quartz thermometer, and other pieces of auxiliary equipment.

Short-term (minutes) jitter of $3^{\circ}K$ peak-to-peak and long-term (hours) jitter of $4^{\circ}K$ peak-to-peak were achieved with this radiometer system, operating at a switching rate of 2.7 Hz, with a post-detection time constant of three seconds and a ten-second digital voltmeter sampling period. This represents a threefold improvement over the previous radiometer system, which operated at a synchronous detection rate of 37 Hz. The improvement does not arise solely from the use of a nodding subdish system but also from electronic and operational improvements in the radiometer itself.

4.4 Radiometer Noise and Gain Change Measurements

During radiometer testing to determine the optimum switching frequency for the nodding subdish mechanism, it became apparent that low frequency radiometer switching resulted in increased radiometer instability, noise jitter, and gain changes. It was decided to examine

the radiometer performance at various switching frequencies to determine the amplitude and frequency dependence of these instabilities.

Noise in an idealized radiometer arises from contributions of two sources: 1) thermal noise jitter, and 2) gain changes. In a total power radiometer these contributions may be written as

$$\Delta T_{\substack{\text{thermal} \\ \text{total power}}} = \frac{K_1 T_s}{\sqrt{B\tau}} \tag{4-1}$$

$$\Delta T_{\substack{\text{gain change} \\ \text{total power}}} = K_2 \frac{\Delta G}{G} T_s \tag{4-2}$$

where T_s = system temperature

B = pre-detection bandwidth

τ = post-detection time constant

G = receiver gain

In a Dicke radiomter, where the input signal arises from RF switching between source and reference, this may be written as:

$$\Delta T_{\substack{\text{thermal} \\ \text{Dicke}}} = \frac{K_3 T_s}{\sqrt{B\tau}} \tag{4-3}$$

$$\Delta T_{\substack{\text{gain change} \\ \text{Dicke}}} = K_3 \frac{\Delta G}{G} (T_2 - T_1) \tag{4-4}$$

where T_s = system temperature

B = pre-detection bandwidth

τ = post-detection time constant

G = receiver gain

T_2 = source temperature

T_1 = reference temperature

The constants in the above equations are of the order of 1.

Since these noise temperatures are non-correlated,

$$\Delta T_{Dicke} = \sqrt{\left(K_3 \frac{T_s}{\sqrt{B\tau}}\right)^2 + \left(K_4 \frac{\Delta G}{G}[T_2 - T_1]\right)^2} \qquad (4\text{-}5)$$

The radiometer gain probability distributions may be represented schematically, following Strum (28), as in Figures 4-15 and 4-16. G is the gain of the radiometer, G_o is the average gain of the radiometer, P(G) is the gain probability distribution function, f is the frequency of random gain fluctuations, and P(f) is the radiometer gain-change frequency probability spectrum. Figure 4-15 shows that the radiometer gain has some probability distribution centered about G_o; and Figure 4-16 shows that most radiometer gain changes occur with low frequency. From these figures we can see that the faster the radiometer is switched between source and reference, the less effect gain instabilities have on increasing the noise of the radiometer,

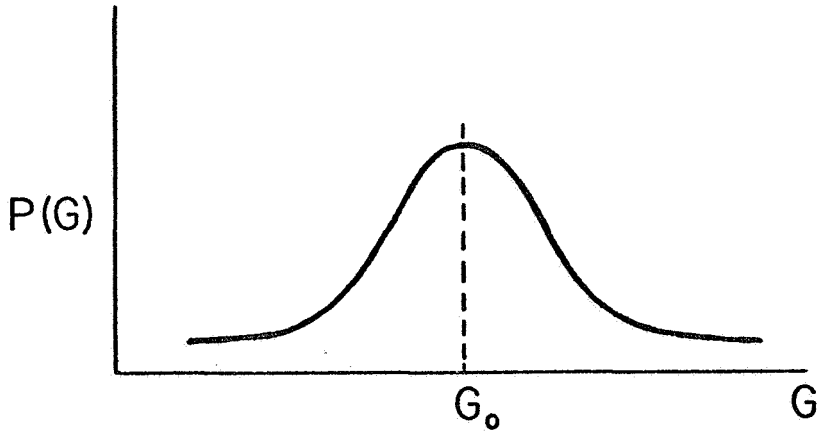

Figure 4-15. Radiometer gain probability distribution.

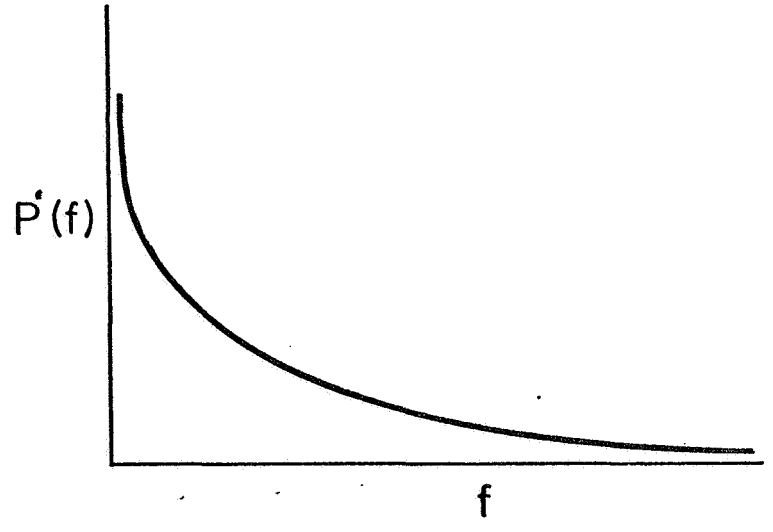

Figure 4-16. Radiometer gain-change frequency probability spectrum.

particularly if the term $(T_2 - T_1)$ is small. For high-speed switching, the term $\Delta T_{\text{gain change}}$ becomes negligible and the curve of ΔT_{Dicke} approaches the theoretical value for thermal noise jitter alone. Figure 4-17 indicates schematically the relationships between switching frequency and noise jitter for an idealized Dicke radiometer system. Curves of ΔT vs. f may be drawn for various values of $(T_2 - T_1)$ as in Figure 4-18.

A series of radiometer tests was made at various switching frequencies to determine the effects of thermal noise and gain changes. Radiometrically switching between a hot load an an ambient load should yield one of the schematic curves in Figure 4-18. Switching between two ambient loads should yield the dotted line, since $(T_2 - T_1)$ is equal to zero, and gain changes would have no effect on the synchronously detected output. One must realize that this will only be true for an idealized Dicke radiometer system.

The experimental method used in these tests was to switch between the hot and ambient loads, and then between both ambient loads at different switching frequencies. ΔT is defined in this section as the actual probable error (in degrees Kelvin) in the measurement of the net detected power when switching between T_2 and T_1. For the radiometer performance tests, the physical temperature difference between the hot and ambient loads was approximately $60^{\circ}K$. However,

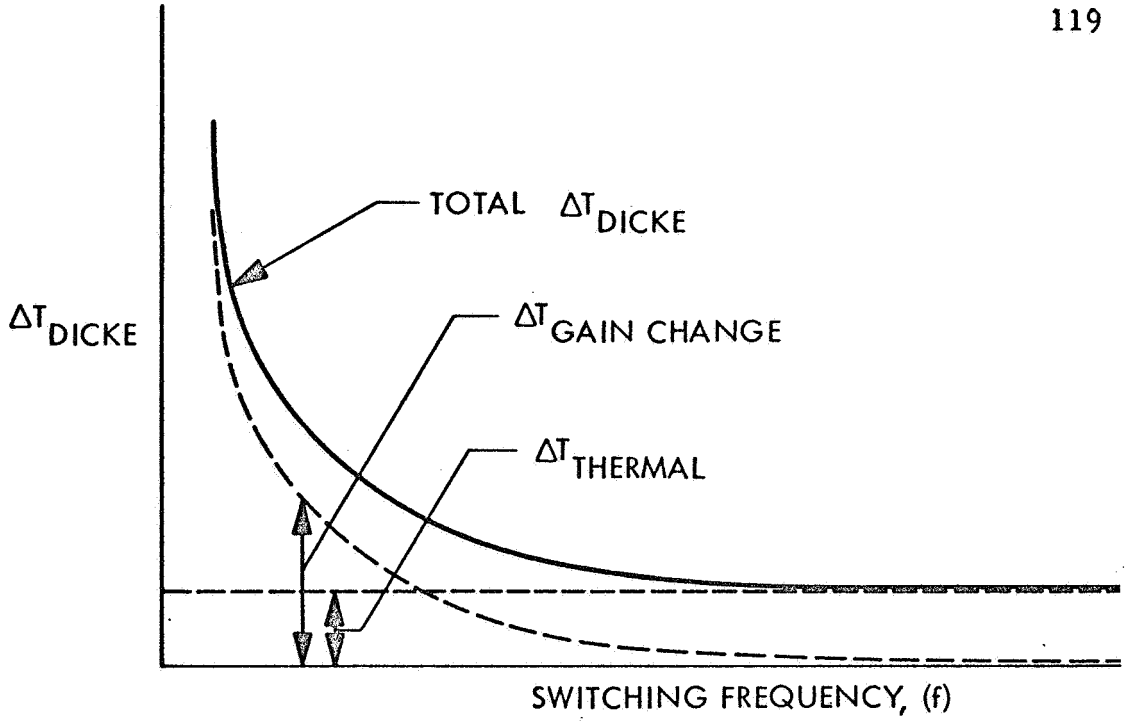

Figure 4-17. Noise jitter vs. switching frequency for an idealized Dicke radiometer.

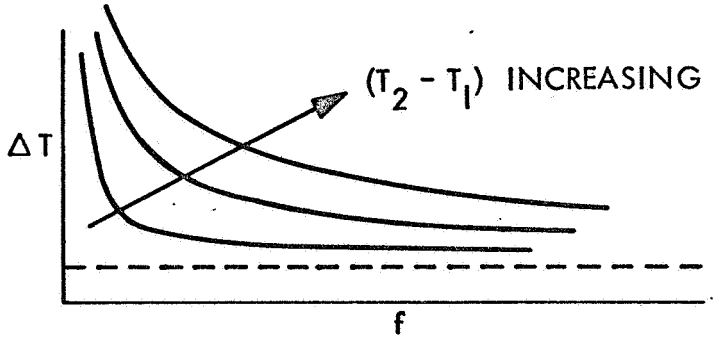

Figure 4-18. ΔT vs. switching frequency for various values of $(T_2 - T_1)$.

since the output of the hot load must pass through the load waveguide, a four-port switch, and a ferrite switch, the net effective output difference was determined to be about $35^{o}K$.

The results of the tests are shown in Figure 4-19. Graphical representations of these results indicate that both the $\Delta T = 0$ and the $\Delta T \neq 0$ curves have a frequency-dependent character, whereas theoretically, only the $\Delta T \neq 0$ curve should have this characteristic. What the graphical results indicate, then, is that in the expression for ΔT containing the thermal jitter term and the gain stability term (Equation 4-5), a third term $(\Delta T)_3$ must also be added. Thus, for a non-ideal Dicke radiometer,

$$\Delta T_{Dicke} = \sqrt{\left(K_3 \frac{T_s}{\sqrt{B\tau}}\right)^2 + \left(K_4 \frac{\Delta G}{G}[T_2 - T_1]\right)^2 + (\Delta T)_3^2} \qquad (4\text{-}6)$$

The $(\Delta T)_3$ term increases with decreasing frequency and at frequencies below 5 Hz begins to dominate the other two terms. Its domination may be clearly seen from the graph, since both ΔT curves have approximately the same shape and value for low frequencies. This also indicates that the contributions of the first two terms are quite small at low frequencies.

In many actual radiometric applications, switching rates in the Dicke system are high enough (greater than approximately 30 Hz) to

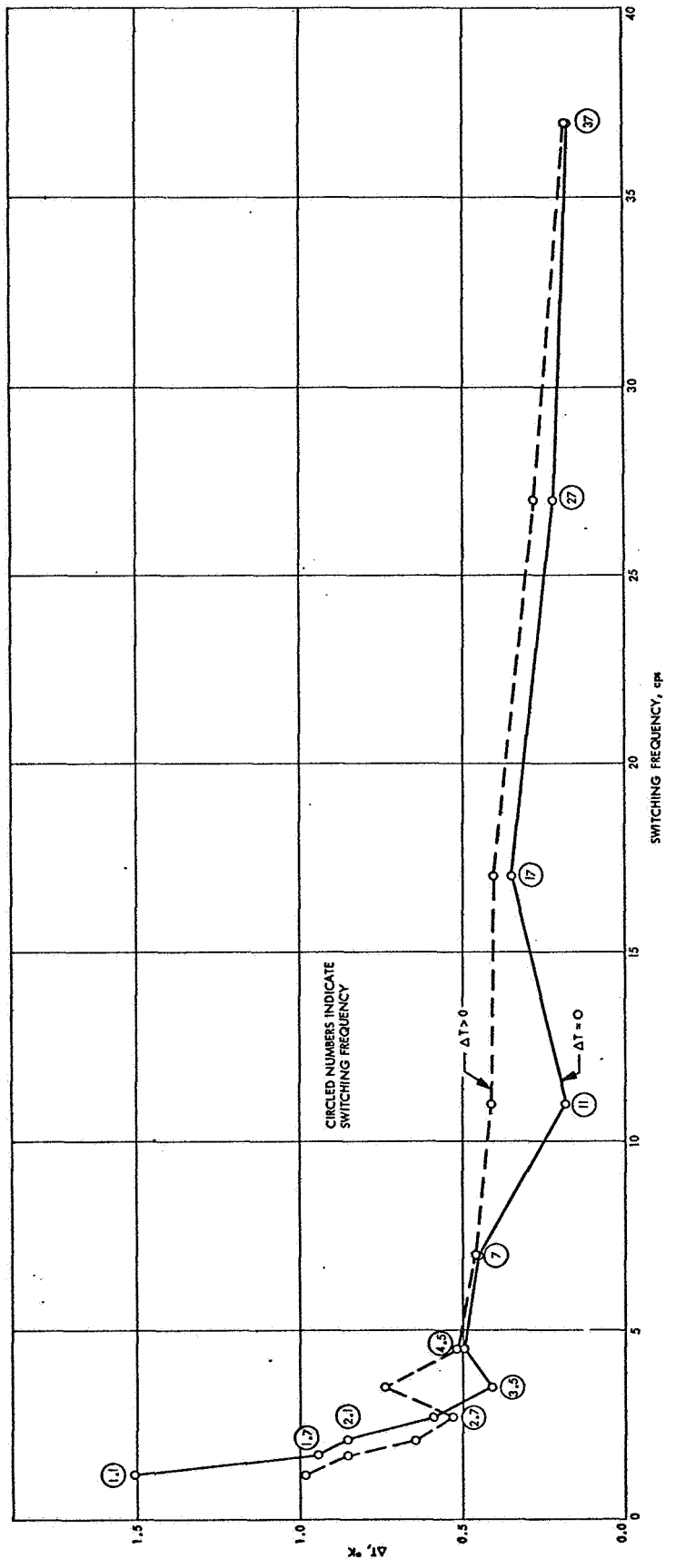

Figure 4-19. Experimental results, ΔT vs. switching frequency.

eliminate the effects of radiometer gain instabilities and other low frequency effects. Theoretically and practically, the problems associated with low-frequency Dicke switching are avoided. However, in low-frequency switching applications, it is necessary to consider all possible sources of radiometer instabilities--mixer diodes, local oscillator, IF amplifiers, switching transients, radiometer rear-end, etc.

In addition to the radiometer switching frequency tests, a second experiment was carried out to determine the noise power spectrum of the radiometer output. Figure 4-20 indicates the non-real time digital spectrum analyzer utilized in this investigation. The RF signal was modulated by a ferrite switch, switching at 2.7 Hz between a hot load and an ambient load. The amplified and detected IF signal was sampled directly without processing by the synchronous detector. The RF switching resulted in a 2.7-Hz calibration pulse being inserted in the spectrumsince the switching was indistinguishable from a 2.7-Hz gain change. The amplitude of the calibration pulse was directly proportional to the net noise temperature difference $(T_2 - T_1)$ between the hot and ambient terminations. Figure 4-21 indicates schematically the form of the spectral content of the noise. Figures 4-22 and 4-23 show the measured spectral content for the ranges 0-50 Hz and 0-5 Hz.

Reference to Figure 4-9 will show that the magnitude of the

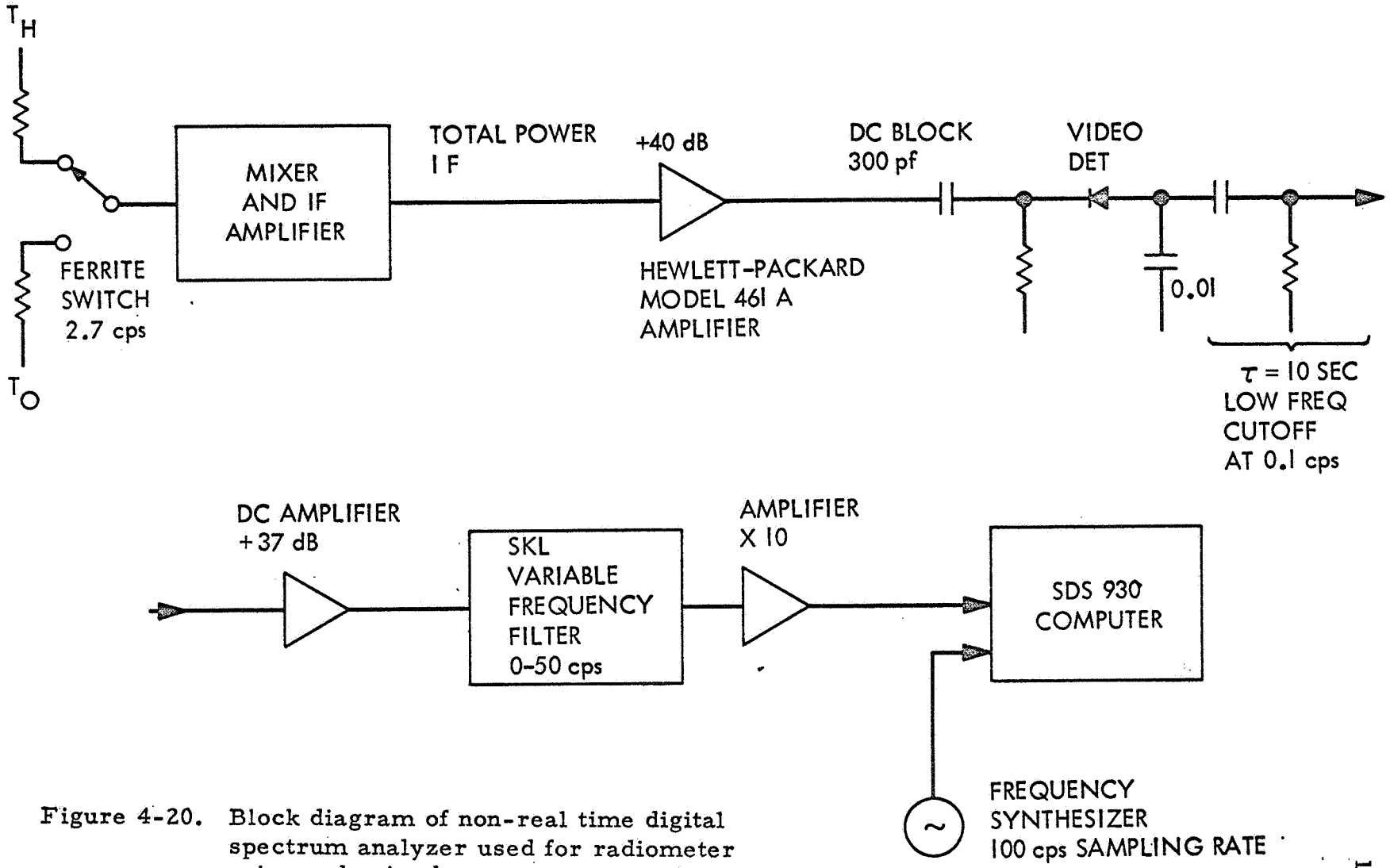

Figure 4-20. Block diagram of non-real time digital spectrum analyzer used for radiometer noise and gain change measurements.

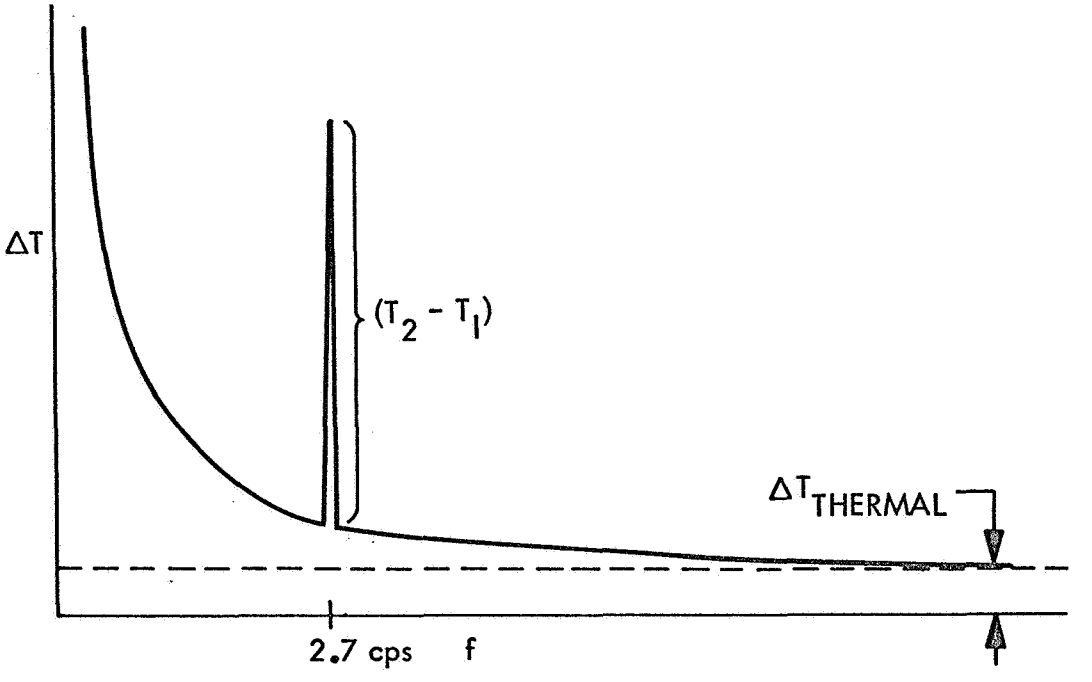

Figure 4-21. Schematic spectral content of radiometer noise, with calibration pulse.

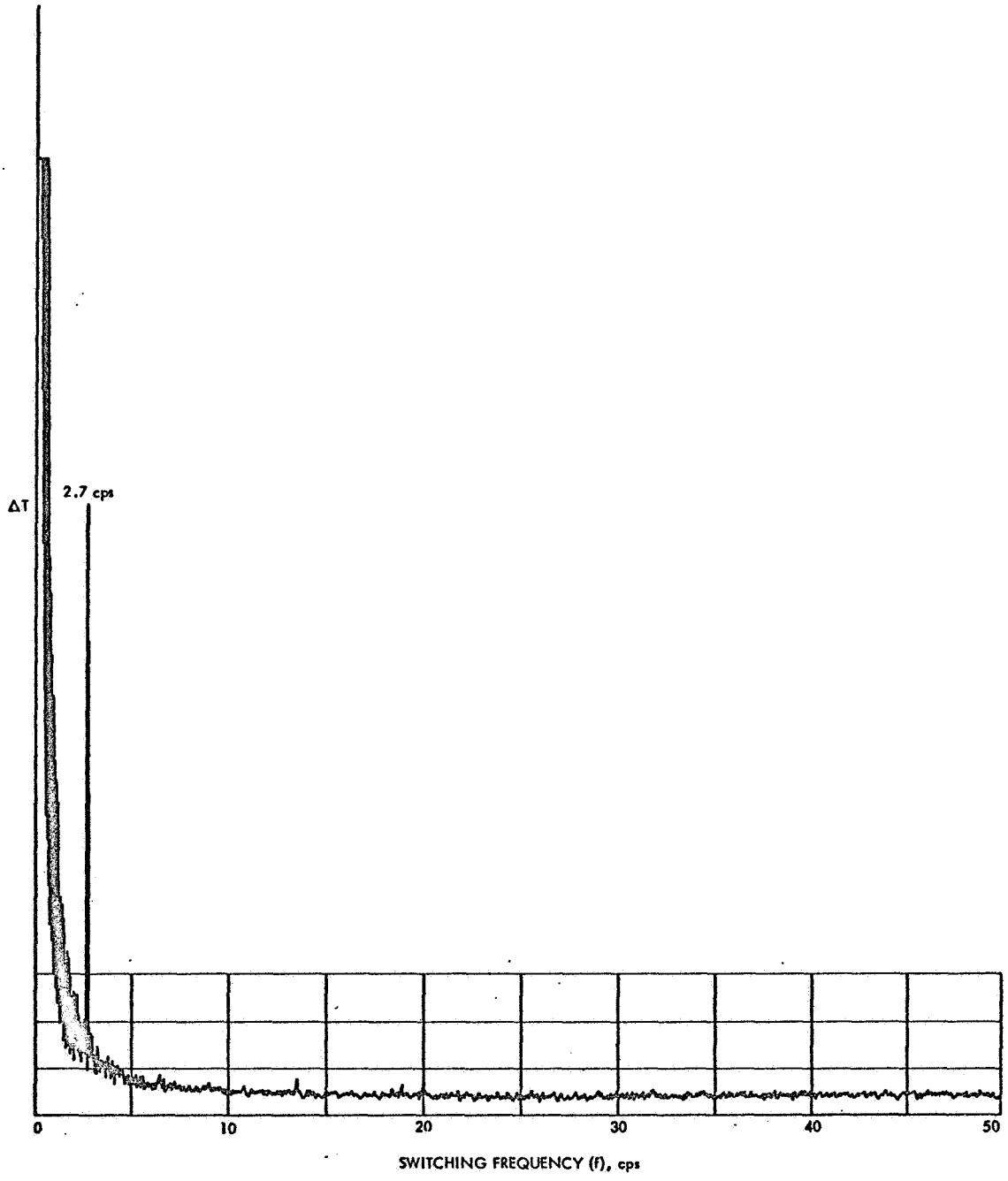

Figure 4-22. Radiometer noise spectrum (0-50 Hz).

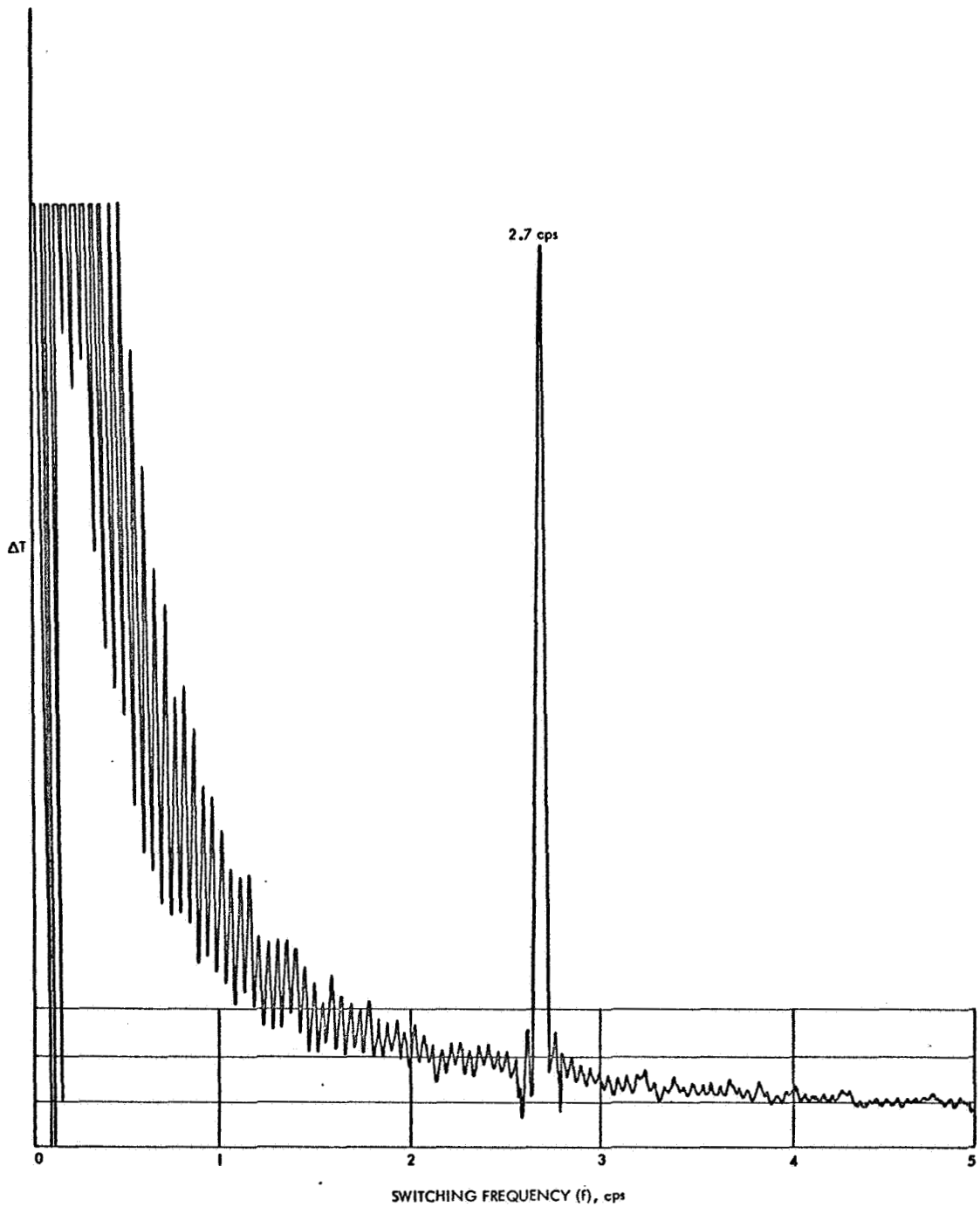

Figure 4-23. Radiometer noise spectrum (0-5 Hz).

2.7-Hz calibration pulse was determined by the equivalent output temperature of the hot load and the insertion loss of the waveguide run between the hot load and the output of the switching circulator. Insertion loss measurements gave a loss of 2.3 dB for the waveguide run including the switch port and circulator. The VSWR looking into the hot load was less than 1.03. Consequently, the equivalent output temperature of the hot load was about 35°K. This was the magnitude of the pulse relative to the curve in Figures 4-22 and 4-23. Thus, the minimum noise jitter attainable by the radiometer (at high switching frequencies) was about 1°K. This compares favorably to the theoretical value of 0.41°K as predicted by the formula

$$\Delta T_{thermal} = \frac{2\,T_s}{\sqrt{B\tau}}$$

where B = total IF bandwidth = 240 MHz

τ = post-detection time constant = 10 seconds

T_s = receiver noise temperature = 10000°K

Chapter 5

OBSERVATIONS OF THE TOTAL LUNAR ECLIPSE OF 18 OCTOBER 1967

5.1 Introduction

Radiometric observations of the Moon before, during, and after a total lunar eclipse, were carried out during the period October 17-19, 1967 (local time), at the Venus Site of the Jet Propulsion Laboratory's Goldstone Tracking Station in the Mojave Desert (cf. Figure 4-1). The purpose of the eclipse observations was twofold: (1) to field-test the newly developed nodding subdish system, and (2) to resolve the measurement uncertainties arising from a previous lunar eclipse measurement in 1964 (29) which indicated no significant change in the lunar temperature during the period of the eclipse. Operational details of the antenna and radiometer in the nodding subdish system have been described previously in Chapter 4 of this paper.

5.2 Observations

The center of the Moon was tracked optically with a forty-power sighting telescope that had been aligned with the primary antenna beam. The nodding subdish system (NSS) then directed the reference antenna beam to a position in the sky 55'30" in declination

above the primary beam, in the synchronous detection mode of operation. The measured isolation between these two beams was 33 dB (cf. Section 4-2).

On October 18, 1967, seventy-one observations of the center of the Moon were made during the period from 02:07 - 13:15 UT. During the sixteen observations prior to local midnight, a relatively low data rate observing sequence was used for the purpose of calibrating the system and, at the same time, obtaining atmospheric information. This low data rate sequence consisted of the following steps (cf. Figure 4-9):

(1) The center of the Moon was tracked for 120 seconds during which time the antenna switched at a rate of 2.7 Hz between the Moon (primary beam) and the sky (reference beam).

(2) The waveguide switch was rotated to the calibration path (hot load line). A reference signal was obtained for 120 seconds from the output port of a switching circulator which switched alternately between heated and ambient terminations, the temperatures of which were monitored continuously by a quartz thermometer and displayed digitally in the radiometer control room. During this period the antenna continued to track the moon, and the subdish continued switching, providing the square wave

reference signal to both the synchronous detector and the ferrite switch driver controlling the switching circulator.

(3) The waveguide switch was returned to its original position in the RF path. The antenna continued to track the Moon as in Step 1; however, the subdish drive mechanism was deactivated for sixty seconds so that a reference signal was no longer available for the radiometer. The resulting "zero" radiometer output corresponded to the radiometer switching between two equal inputs (assuming ideal radiometer performance). This reference output will be subsequently referred to as the "electronic" baseline.

(4) The subdish drive mechanism was reactivated, causing a reference signal to be transmitted to the radiometer. The NSS and radiometer then operated in the normal mode of operation. However, the antenna drive was turned off for the first time, allowing the earth's rotation to displace the antenna beam two degrees east of the Moon. By this time the NSS was switching between two nearly equal-temperature positions in the sky, and the zero-output radiometer reference thus obtained (subsequently referred to as the "sky" baseline) was

measured for an additional 120 seconds.

During the fifty-five observations made after local midnight a relatively high data-rate observing sequence was used, because the lunar eclipse took place during this period. Sample chart recordings of runs 6 to 10 are shown in Figure 5-1. This high-data-rate sequence consisted of the following two steps:

(1'). Same as Step (1) (step A, Figure 5-1)

(2'). Same as Step (3) (step B)

Every fourth two-step cycle of this type was followed by a more extended four-step calibration sequence consisting of:

(1''). Same as Step (1) (step A)

(2''). Same as Step (3) (step B)

(3''). Same as Step (2) (step C)

(4''). Same as Step (4) (step D)

Of the fifty-five observations made following meridian transit, ten were made during the initial penumbral stage of the eclipse (0710 - 0826 UT), thirteen during the initial umbral stage (0826 - 0945 UT), eight during totality (0945 - 1046 UT), thirteen during the concluding umbral stage (1046 - 1245 UT), and eleven during the concluding penumbral stage (1205 - 1321 UT).

The data were recorded on a strip-chart recorder with a

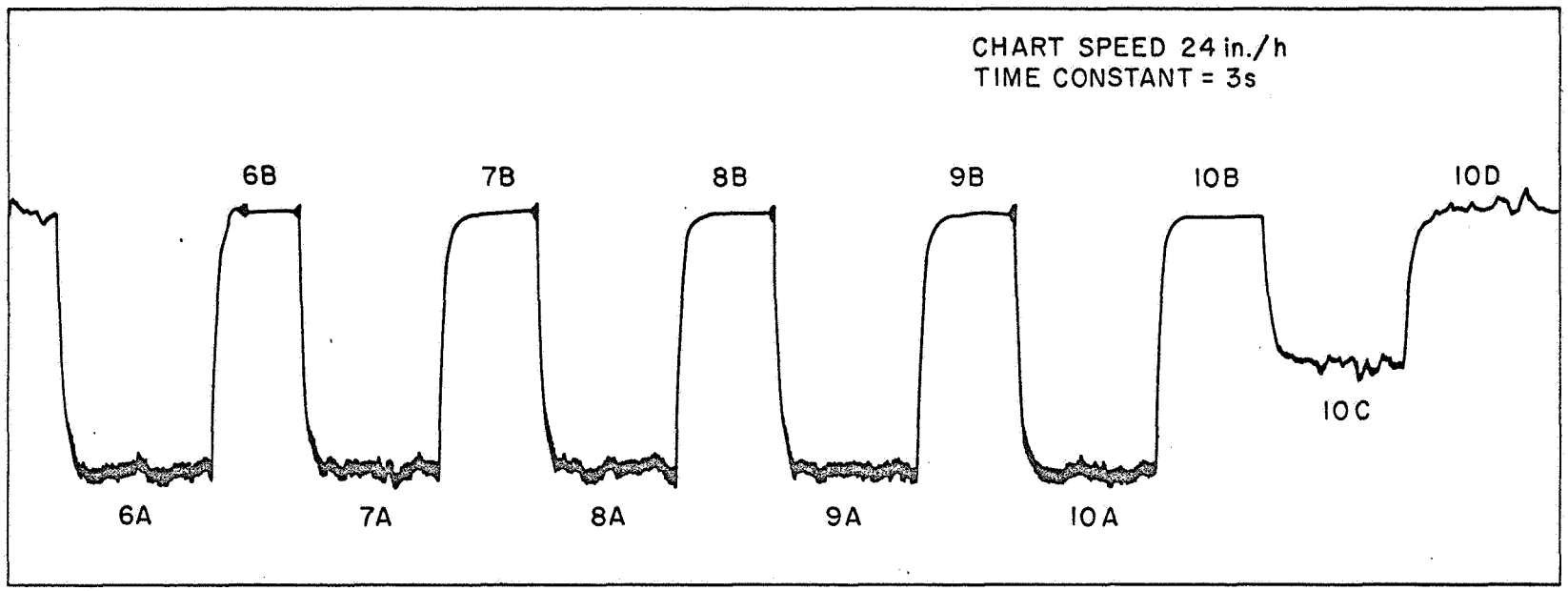

Figure 5-1. Strip chart recording of runs 6 to 10 made during lunar eclipse measurements (A = Moon, B = electronic baseline, C = hot load, D = sky baseline).

radiometer post-detection time constant of five seconds. The data were also recorded on a digital counter-printer, with effective counting intervals of sixty seconds for the electronic baseline and 120 seconds for the Moon, calibration, and sky-baseline. As a measure of system performance, the digital results corresponding to the strip-chart record of runs 6 to 10 indicated in Figure 5-1 were converted into equivalent antenna temperature (referred to the aperture of the antenna). The average probable error of each Moon-track, calibration, and sky-baseline data point was $0.36^{\circ}K$ (proportional to the jitter of the pen recording in Figure 5-1). The average probable error of the electronic-baseline data was $0.05^{\circ}K$.

5.3 Gain Calibration

The data obtained during Step 2 of the low-data-rate sequence and Step 3" of the high-data-rate sequence provided a means to monitor the relative system gain during the experiment. In this mode of operation an amount of power proportional to the known temperature differences between the heated and ambient terminations was injected into the radiometer, i.e., $P_i = C(T_h - T_a)$, where the constant C is determined by various physical constants and such system constants as the insertion loss between the heated termination and the reference point at the output of the waveguide switch. If the radiometer output voltage is assumed to be linearly related to the

power injected into the RF path, then the radiometer gain will be given by

$$G_{rad} = \frac{V_{cal} - V_{baseline}}{C(T_h - T_a)} \qquad (5\text{-}1)$$

where V_{cal} is the output voltage during the calibration step and $V_{baseline}$ is the output voltage during the baseline step. (Unless specified otherwise the electronic baseline was used.)

Conversely, a system "transfer constant" may be defined by

$$STC = \frac{1}{GC} = \frac{(T_h - T_a)}{V_{cal} - V_{baseline}} \qquad (5\text{-}2)$$

and the units of STC are degrees temperature difference (at the point of the heated termination) per voltage change at the radiometer output. Ultimately it is necessary to convert the STC to a temperature change at the reference point of the waveguide switch. However, the STC as defined above provides a convenient measure of the relative gain stability of the radiometer. Consequently, the twenty-two values of the system transfer constant measured during the night of the eclipse are plotted in Figure 5-2 as a function of Universal Time.

Superimposed on the data points in Figure 5-2 is a second-order curve fitted to the data. The jitter of the actual data with respect to this curve corresponds to gain changes of about 0.1 dB,

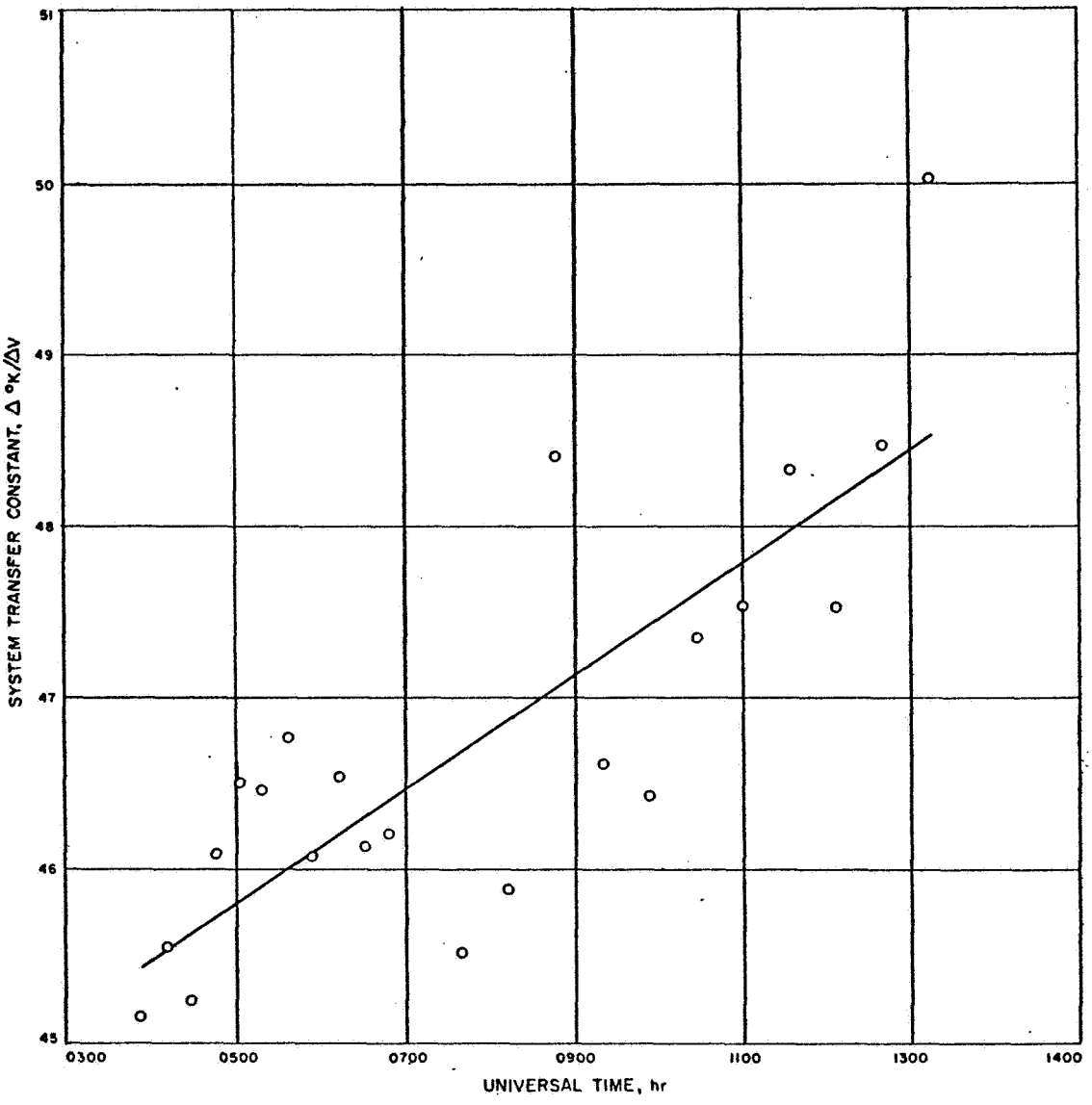

Figure 5-2. System transfer constant during night of eclipse (18 October 1967).

while the long-term change over a period of nine hours corresponds to a gain drift of about 0.3 dB. This second-order curve fitted to the actual data points was used to normalize the moon-temperature data and thereby remove the effects of gain drift from the data.

5.4 Extinction Curve

For each Moon track, an STC-normalized antenna temperature may be determined, corresponding to a specific lunar zenith angle (Z). The effective Moon black-body disc temperature is related to the measured antenna temperature by the relation

$$T_{AM} = T_A \cdot L \tag{5-3}$$

where T_{AM} = effective Moon black-body disc temperature

T_A = measured STC-normalized antenna temperature relative to the aperture of the antenna

L = atmospheric loss factor, greater than 1.0

The atmospheric loss factor L is defined as

$$L = e^{\alpha l} \tag{5-4}$$

where α = atmospheric attenuation per unit length of atmosphere

l = length of atmospheric path

The atmospheric path length l is defined by

$$l = l_o \cdot AM(Z) \tag{5-5}$$

where l_o = atmospheric scale height (on the order of 15 kilometers)

$AM(Z)$ = equivalent air mass at each zenith angle Z (The air mass is equal to sec(Z) to within approximately 1 - 2% for zenith angles less than 80^o.)

Thus if the zenith atmospheric loss factor L_o is

$$L_o = e^{\alpha l_o} \tag{5-6}$$

then the atmospheric loss factor becomes

$$L = L_o^{AM(Z)} \tag{5-7}$$

Equation (5-3) may be rewritten as

$$T_{AM} = T_A \cdot L_o^{AM(Z)} \tag{5-8}$$

or, inversely

$$T_A = T_{AM} \cdot L_o^{-AM(Z)} \tag{5-9}$$

Taking the logarithm of both sides of Equation (5-9) we obtain

$$\log T_A = \log T_{AM} - AM(Z) \cdot \log L_o \tag{5-10}$$

Following the method presented by Coates (30), a standard extinction curve of the data taken on 18 October may be plotted as in Figure 5-3, following Equation (5-10). The ordinate is the logarithm of the STC-normalized antenna temperature (T_A), and the abscissa is the air mass, AM(Z). For a constant source temperature (T_{AM}) and a constant atmospheric loss (L_o), the slope (log L_o) of an extinction curve of this type provides a direct measure of the atmospheric loss; and the intercept with the ordinate-axis is proportional to the source temperature. Although the AIR MASS = 0 axis is suppressed, and although there is no physical significance to values of the air mass less than 1.0, the determination of the source temperature depends on an extrapolation of the extinction curve to that line.

In Figure 5-3 each pre-meridian-transit data point is plotted as a dot (•). Since these observations were made prior to the eclipse, the brightness temperature of the Moon may be presumed to have remained constant in this four-hour interval, and the data may be used to evaluate the atmospheric loss. Using a linearized curve-fitting procedure developed by Stelzried and Rusch (31) the loss before meridian transit was determined to be 0.36 dB with a probable error of 0.03 dB.

Each post-meridian-transit point is plotted in the figure with a circle (o). Also indicated are the approximate times for the

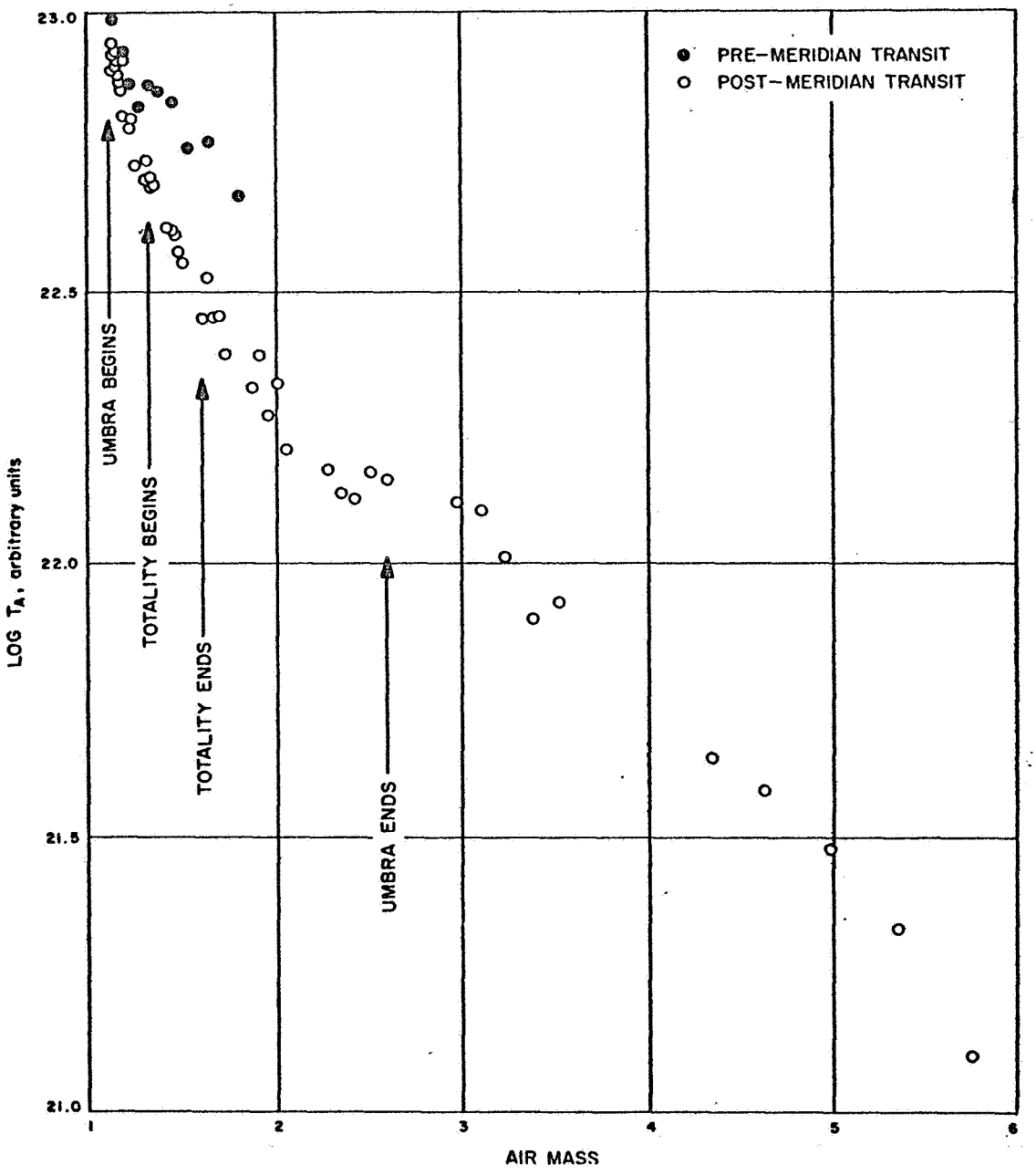

Figure 5-3. Lunar extinction curve during night of eclipse (18 October 1967).

beginning and ending of the umbral stage of the eclipse, and the beginning and ending of totality. The data are considerably compressed during the initial stage of the eclipse, because of the non-linear scales in a plot of this type. However, the effect of a changing source temperature is evident.

5.5 Data Reduction

T_{AM}, the equivalent antenna temperature of the Moon (without atmospheric loss) is related to T_A, the measured antenna temperature relative to the aperture by

$$T_A = T_{AM}(L_o)^{-AM(Z)} \tag{5-11}$$

where Z is the zenith angle, AM(Z) is the equivalent air mass at each zenith angle, and L_o is the atmospheric loss at zenith, i.e., unity air mass. If L_o is known or assumed to be known, the relation can be inverted to yield the equivalent Moon antenna temperature for each data point, i.e,

$$T_{AM} = T_A(L_o)^{+AM(Z)} \tag{5-12}$$

Assuming the pre-transit value of L_o = 0.36 dB remained constant during the entire night of the eclipse, an equivalent Moon antenna temperature can be determined for each of the seventy-one

data points. These values, normalized to the average of the thirteen pre-transit values, are plotted in Figure 5-4 as a function of universal time on 18 October. Also indicated are (A) the beginning of the umbral stage at 0826, (B) the beginning of totality at 0945, (C) the end of totality at 1046, and (D) the end of the umbral stage at 1205. A seven percent decrease in the lunar equivalent disc brightness temperature is evident.

The moon was too low in the sky to obtain the necessary post-eclipse data points necessary to establish an adequate secondary baseline. Consequently, there is some question about the proper value of L_o to use for the post-transit data. The large zenith angles for the post-eclipse data points magnified loss-dependent effects. If the Moon is assumed to have reattained temperature equilibrium in the final few data points, a value of $L_o = 0.386$ dB must be assumed. This value is within the probable error of the pre-transit value of 0.36 dB, indicating that it may be academic to attempt to refine the value of L_o still further. Nevertheless, the data were replotted in Figure 5-5 using the value of $L_o = 0.386$. The curve is virtually identical to Figure 5-4, except for the last few points. In either case the umbral cooling rates are the same and the maximum percentage temperature change is seven percent.

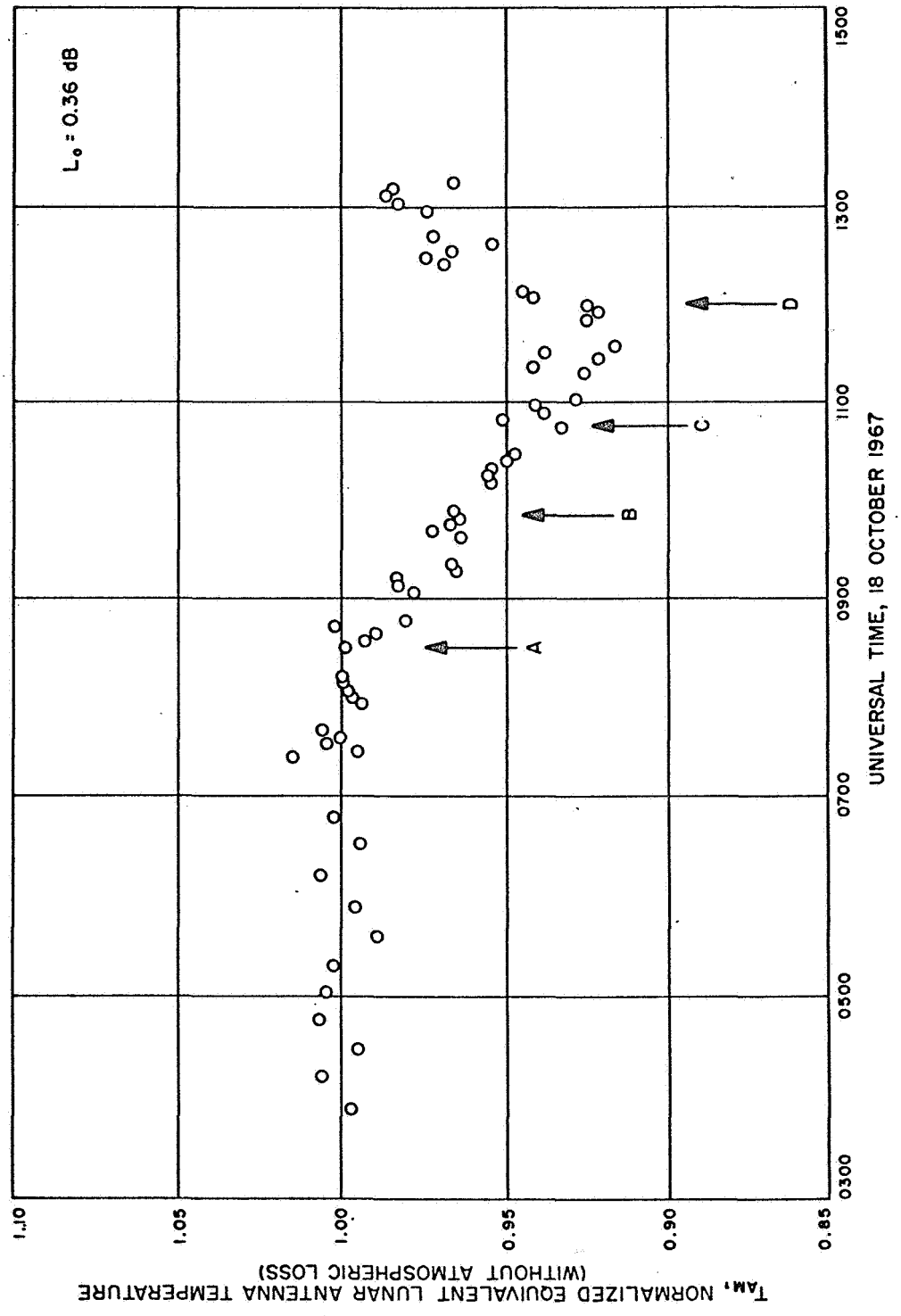

Figure 5-4. Equivalent lunar antenna temperature during night of eclipse, using electronic baseline (L_o = 0.36 dB).

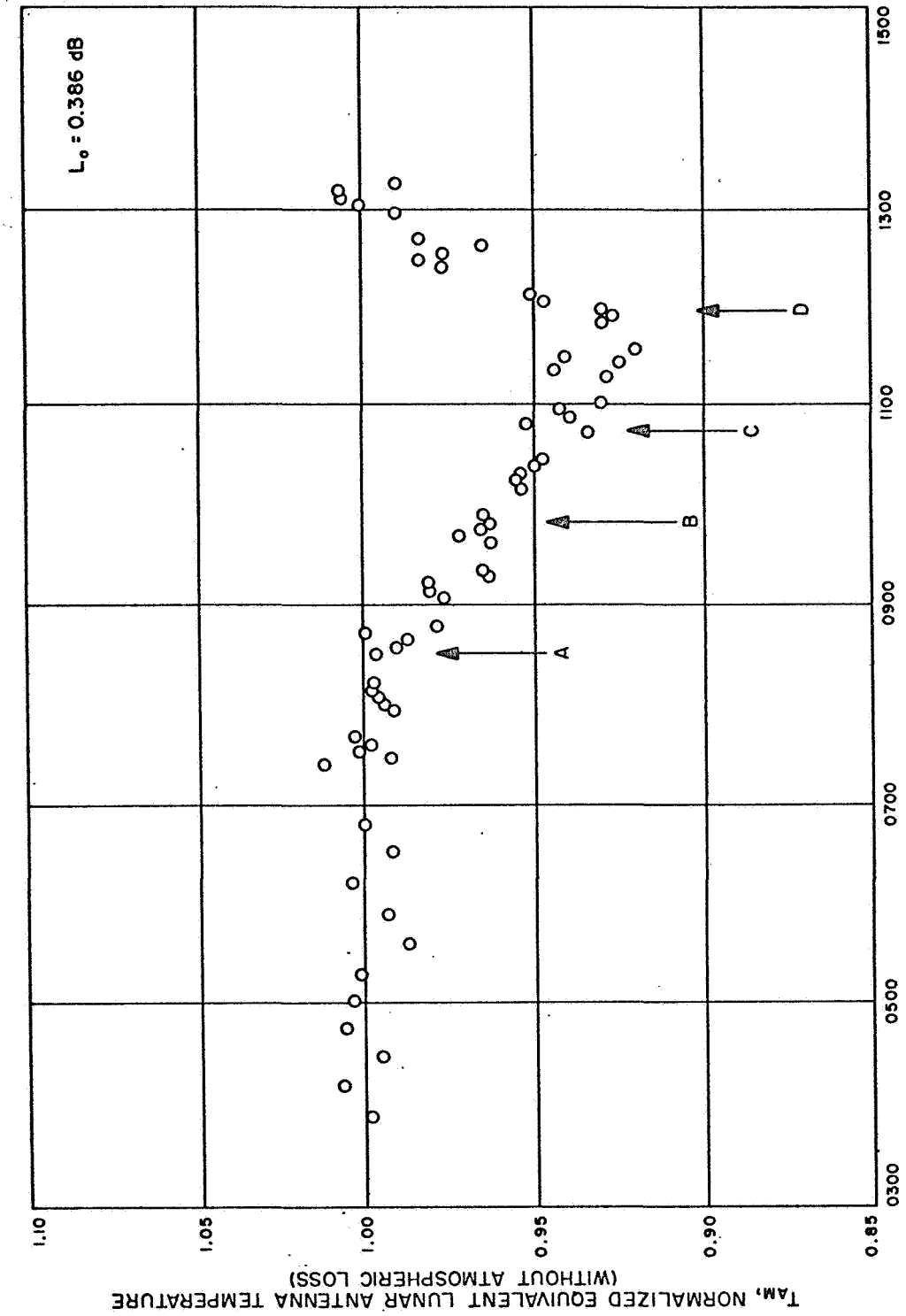

Figure 5-5. Equivalent lunar antenna temperature during night of eclipse, using electronic baseline (L_o = 0.386 dB).

5.6 Conclusions

1. A decrease of seven percent in the equivalent black-body disc temperature of the Moon was measured during the total lunar eclipse of 18 October 1967. (The 1σ measurement dispersion is estimated to be 0.33% of the Moon temperature.) If it is assumed that the equivalent black-body disc temperature of the full Moon is 280°K at a wavelength of 3.33 mm (4), this seven percent decrease amounts to a temperature decrease of 19.6 ± 0.9 (1σ)°K.

2. Using the value of 280°K to establish a full-Moon equivalent disc-temperature calibration constant, the eclipse curves of Figures 5-4 and 5-5 indicate a cooling rate of about five degrees per hour during the umbral stage of the eclipse.

3. The measured jitter of the data points plotted in Figures 5-4 and 5-5 is 1.7 times as large as predicted by the measured short-term radiometer jitter. The fact that this jitter is larger than the theoretical value is due to (1) long-term radiometer fluctuations and/or (2) atmospheric scintillations and opacity fluctuations. Although additional quantitative data are presently unavailable, it is felt that the NSS has significantly reduced the atmospheric effects. A further evaluation of the atmospheric "smoothing" produced by the NSS is a significant area for additional investigation.

4. A comparison of the maximum temperature decreases

(in percentage of the full-Moon temperature) measured radiometrically at short millimeter wavelengths during total lunar eclipses is made in Table 5-1 and Figure 5-6. In general, the percentage temperature decrease increases with decreasing wavelength. It should be remembered, however, that the equivalent lunar brightness temperature in this wavelength range also increases from 250 - 300°K at 3-4 mm to about 370°K at 1 mm. The results of this measurement are in close agreement with those obtained by Epstein et al for the December 30, 1963 eclipse. The results by Kamenskaya et al all appear consistently higher than the USC results (Rusch et al).

The results of the October 1967 total lunar eclipse measurement will be published by Rusch et al (35) at a future date.

5.7 Post-Eclipse Observations and Calibrations on 19 October

Thirty-three observations of the Moon were carried out on 19 October 1967, the night following the eclipse, using the low-data-rate sequence described earlier. The data from these observations served to further calibrate the system and evaluate its performance. The pre-transit and post-transit lunar extinction curves for 19 October are plotted in Figure 5-7. In this figure the pre-transit data points are indicated by dots (•) and the post-transit points by circles (o). The solid curves in the figure were fitted to the data points

Wavelength (mm)	Reported By:	Maximum Temperature Decrease (%)	Eclipse Date
1.0	A	9.7 ± 1.5 (1σ)	December 19, 1964
1.2	B	22.5 ± 2.5 (*)	December 30, 1963
3.2	C	6.4 ± 0.78 (1σ)	December 30, 1963
3.33	D	7.0 ± 0.33 (1σ)	October 18, 1967
4.0	B	12.0 ± 2 (*)	December 30, 1963
6.0	B	8.0 ± 2 (*)	December 30, 1963

A = Low and Davidson 1965 (32)
B = Kamenskaya et al 1965 (33)
C = Epstein et al 1964 (34)
D = Rusch et al 1968 (5)
(*) = definition of error unavailable

TABLE 5-1

Comparison of lunar temperature decreases during a total lunar eclipse, as a function of wavelength. (cf. Figure 5-6)

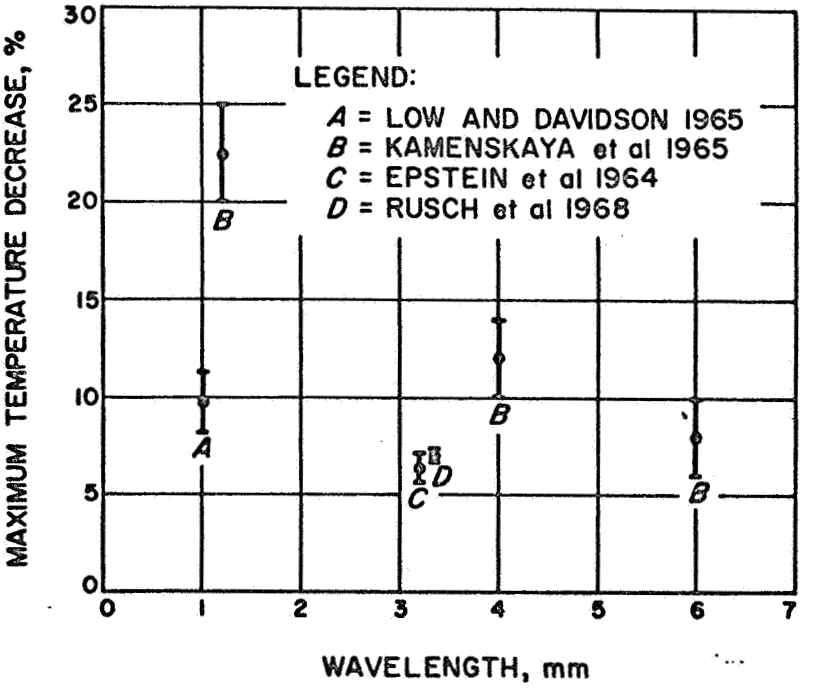

Figure 5-6. Maximum percentage temperature decrease measured during a total lunar eclipse. (cf. Table 5-1)

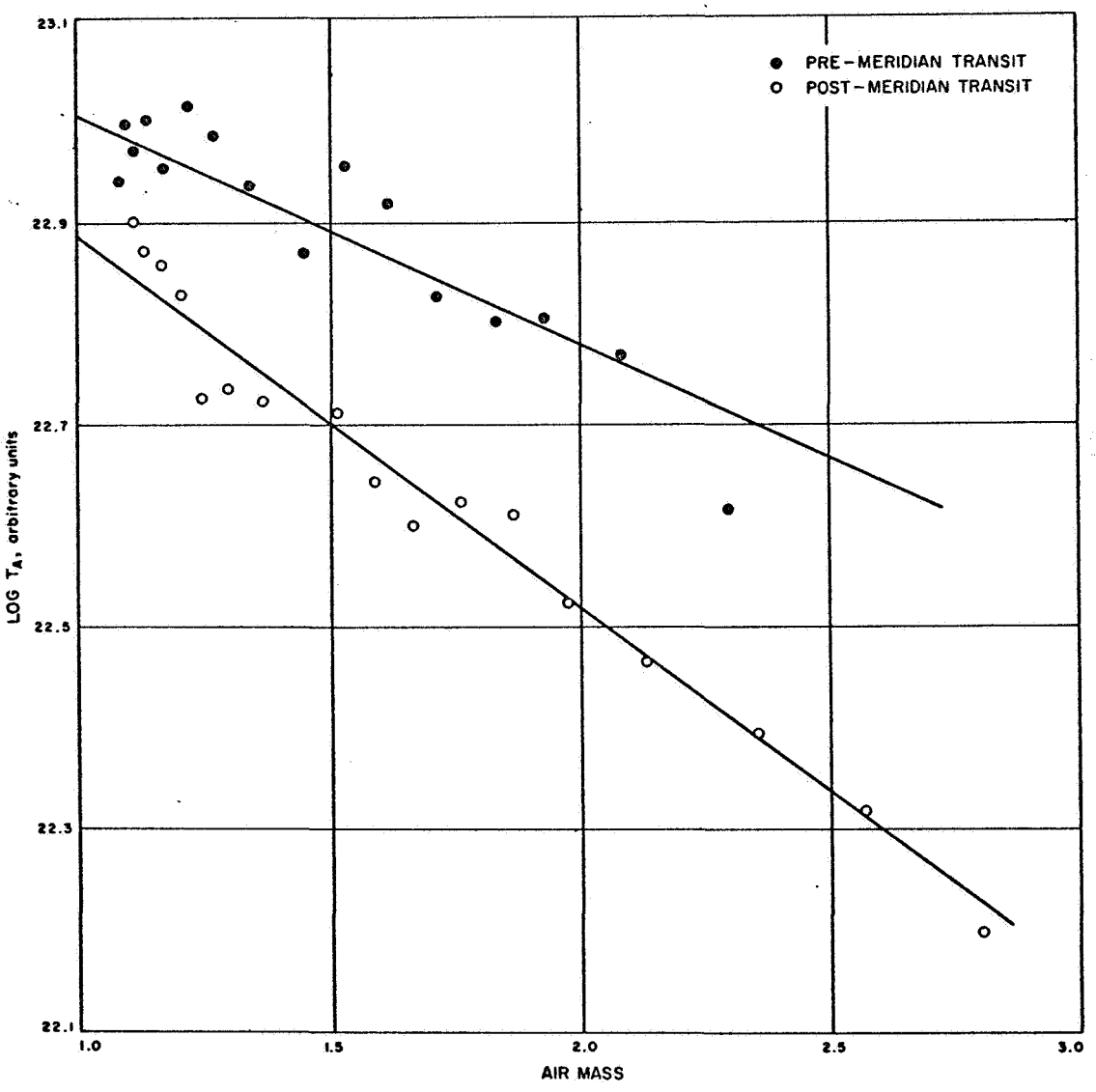

Figure 5-7. Lunar extinction curve during night after eclipse (19 October 1967).

using the Stelzried-Rusch technique described earlier. The data in Figure 5-7 indicate that the atmospheric loss was changing during the seven-hour-long observations.

The observational data from 19 October provided a means to compare the two different baselines: the electronic baseline obtained by deactivating the subdish drive mechanism so that a reference signal was not available for the radiometer, and the sky baseline obtained by switching the NSS between two nearly equal-temperature positions in the sky. Prior to this point in the text all data was reduced using the electronic baseline. However, the low-data-rate sequence used on 19 October enabled both types of baseline to be determined in each of the thirty-three observation cycles.

Comparison of the two baselines is carried out in Table 5-2. In the left-hand column are the results of the data reduced using the electronic baseline for (1) the pre-meridian-transit data on 19 October, (2) the post-meridian-transit data on 19 October, and as a reference, (3) the pre-meridian transit data on 18 October. The two quantities tabulated are T_E, a hypothetical antenna temperature of the Moon extrapolated above the atmosphere but not including certain calibration constants, and L_o, the atmospheric loss. It will be seen that T_E remained essentially unchanged for the three sets of data. The two values of L_o for 19 October were considerably different,

	Electronic Baseline Data Reduction	Sky Baseline Data Reduction
Pre-Transit Data 19 October	$T_E = 213.1 \pm 1.4^{\circ}K$ $L_o = .261 \pm .019$ dB	$T_E = 211.1 \pm 1.3^{\circ}K$ $L_o = .247 \pm .017$ dB
Post-Transit Data 19 October	$T_E = 212.2 \pm 1.0^{\circ}K$ $L_o = .376 \pm .012$ dB	$T_E = 211.8 \pm 1.0^{\circ}K$ $L_o = .394 \pm .012$ dB
Pre-Transit Data 18 October	$T_E = 215.0 \pm 2.0^{\circ}K$ $L_o = .363 \pm .030$ dB	Not available

TABLE 5-2

indicating a changing atmosphere. In the right-hand column are the results of the data reduced using the sky baseline for the two periods on 19 October. The corresponding values of T_E using the two techniques did not differ by more than a percent, and the corresponding values of L_o did not differ by more than .02 dB. Although the measured differences in T_E were within the overlapping probable errors, it was noticed that generally the sky baseline yielded a slightly lower extrapolated Moon temperature than the electronic technique. This effect may have been due to either non-ideal radiometer performance or unequal antenna temperatures seen by the primary and reference beams after the antenna had drifted two degrees east of the Moon. Whatever the cause, however, the data in

Table 5-2 indicates that this effect introduced a possible error in the lunar equivalent disc temperature of no more than one percent.

A second procedure was carried out to evaluate the relative effects of the two different baselines. The data from 18 October were reduced in exactly the same manner described previously with the one exception that the sky baseline was used instead of the electronic baseline. Since sky-baseline information was obtained less frequently, fewer data points could be obtained in this manner. The resulting equilibrium Moon temperature was less than one percent less. A normalized eclipse curve, such as the curve plotted in Figure 5-5, proved to literally overlay the curve derived using the electronic baseline. To indicate the similarity, the data from Figure 5-5 are reproduced identically in Figure 5-8 as circles (o). The normalized data using the sky baseline are superimposed on Figure 5-8 using solid dots. To within the scatter of the data points the two sets of data are identical. Consequently, the conclusions stated in the previous section about the eclipse results appear to be valid for data reduced using either type of baseline.

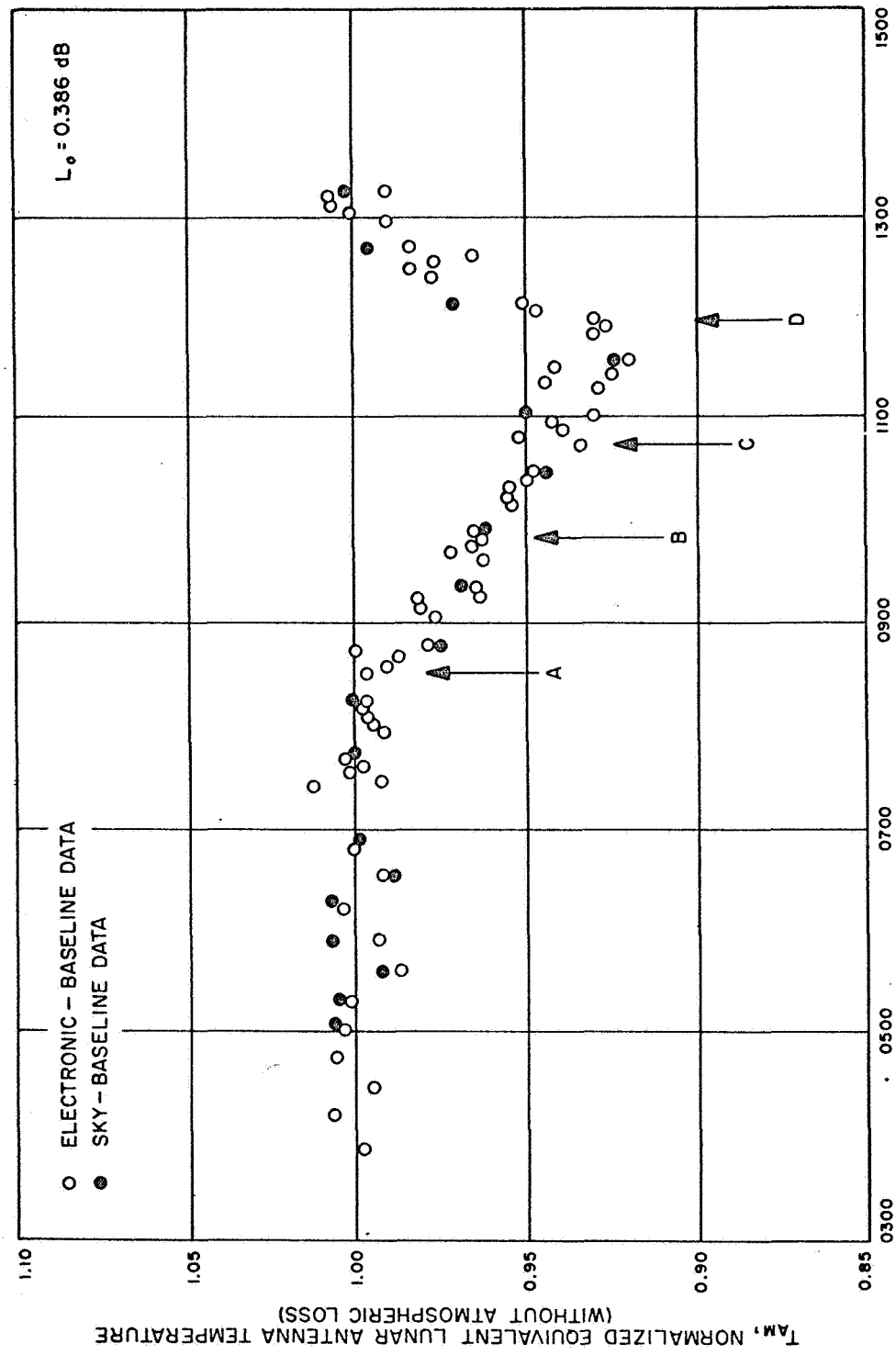

Figure 5-8. Equivalent lunar antenna temperature during night of eclipse, using sky and electronic baselines (L_o = 0.386 dB).

Chapter 6

AREAS FOR FURTHER INVESTIGATION

In the interest of improving the existing nodding subdish system/radio telescope facility and expanding the areas of usefulness of the system, several suggestions may be made regarding areas for future investigation and development.

For radio-astronomical and atmospheric observations, the nodding subdish system (NSS) must operate for long periods of time without mechanical attention. At the present time, the NSS has operated off-and-on for about thirty total hours (approximately 300,000 switching cycles at 2.7 cps), for extended investigations, it may be necessary to operate the NSS for several million switching cycles. It has been noticed that at present there exists a small amount of wear in the cam/cam-follower assembly. This leads to an indefinite positioning of the subdish in one of its tilted positions. The wear is quite small and it is felt that no significant deterioration of the NSS performance exists at the present time, but for the sake of reliability and future operational accuracy, a redesign should be carried out. One solution to the wear problem would be the utilization of a roller cam-follower which would roll instead of scrape against the cam.

In conjunction with the mechanical wear problem noted above, a switching speed problem exists also. As discussed in Chapter 4, the radiometer noise characteristics adversely affect the system performance at low switching speeds (less than 5 cps). A detailed knowledge of the radiometer components' noise characteristics must be known to select an optimum switching frequency, however. It was found during testing of the NSS that the switching frequency of 2.7 cps was a good compromise from both an electronic and mechanical standpoint. It was determined in subsequent electronic tests that low switching rates rapidly compromise radiometer performance. As a first step toward improving the system performance, a higher switching rate should be used, preferably around 7 cps. Since this rate seems to be mechanically risky from the standpoint of NSS longevity and strength, a redesign should be undertaken to solve these problems.

Of primary importance to good radiometer performance is the use of low-noise mixer diodes. Diode improvement will directly improve the sensitivity of the radiometer by reducing the system noise temperature. During the past year or so, semiconductor technology has advanced to the point that Schottky barrier millimeter-wave diodes can be fabricated using planar photolithographic techniques. Such diodes have improved noise figures over conventional silicon or gallium-arsenide point-contact diodes. Plans are being

made to establish a semiconductor laboratory on the USC campus suitable for the fabrication of such Schottky barrier diodes. If it is found that these mixer diodes have noise characteristics superior to those of commercially available diodes, they will be installed and tested in the USC/JPL radio-telescope facility.

In order to acquire large amounts of atmospheric data, USC is developing a semi-automated sun tracking system (STS) consisting basically of the existing 90-GHz radio-telescope, the nodding subdish system, and a suntracking device. The sun will be tracked by allowing the existing sidereal drive to move the antenna in right ascension. A tracking-error sensing device, consisting of a refracting telescope and four photocells upon which the sun's image is projected, will determine pointing errors and thus send an error signal to the track-control equipment. When the sun is centered evenly on the four photocells, the resistances of all cells are equal, and no error signal is produced. If the sun's image should shift, the cells would be illuminated unequally, thereby producing an error signal. Suitable optical filters will be provided to obtain optimum response from the photocells. An electronic system has been designed to convert the error signals from the photocells into control pulses. These control pulses will then be fed into the SLO-SYN stepping motors located on the right ascension and declination axes of the telescope. These motors will redirect the telescope toward

the sun. The photocells controlling the right ascension axis will also control the speed of the sidereal tracking motor.

In conjunction with the above mentioned sun tracking system, a horizontal microwave link should also be established to determine atmospheric attenuation of millimeter waves. In addition, accurate monitoring of meteorological data should be carried out during the period of atmospheric and radio-source observations. Correlations of these sets of data should provide considerable atmospheric information useful in many types of communication systems.

During radio-astronomical observations, when large amounts of data were taken over a period of many hours or days, it became very difficult to record pertinent experimental facts, such as date, time, temperature, digital voltmeter reading, etc. For this reason, a data recording and storage system should be developed to record the important experimental numbers, all of which appear digitally on some electronic output and which could be easily recorded for later processing and analysis. The present method of recording data by hand leads to inaccuracy and tedium, and is subject to the ever present problem of memory loss when old data is reviewed days, months, or even years later. A well-operating data recording and storage system is necessary for the success of large-scale investigations of lunar, solar, and atmospheric properties.

BIBLIOGRAPHY

1. Dicke, R. H., "The Measurement of Thermal Radiation at Microwave Frequencies", The Review of Scientific Instruments, Vol. 17, No. 7, pp. 268-275, July 1946.

2. Steinberg, J. L., and Lequeux, J., Radio Astronomy, McGraw-Hill Book Co., New York, 1960.

3. Rusch, W. V. T., Slobin, S. D., Stelzried, C. T., "Millimeter-Wave Radiometry for Radio Astronomy", Univ. of So. Calif. Electrical Eng. Dept., Report No. USCEE 161, Los Angeles, Calif., February 1966.

4. Rusch, W. V. T., Slobin, S. D., Stelzried, C. T., "Millimeter-Wave Radiometry for Radio Astronomy", Univ. of So. Calif. Electrical Eng. Dept., Report No. USCEE 183, Los Angeles, Calif., December 1966.

5. Rusch, W. V. T., Slobin, S. D., Stelzried, C. T., "Millimeter-Wave Radiometry for Radio Astronomy", Univ. of So. Calif. Electrical Eng. Dept., Report No. USCEE 263, Los Angeles, Calif., March 1968.

6. Viggh, M. E., "Cassegrain Antennas", Elteknik, Vol. 5, pp. 83-87, May 1962.

7. Stacey, J., "Research and Experimentation on Space Applications of Millimeter Waves", Aerospace Corp. Tech. Report TDR-169(3250-41)TN-2, El Segundo, Calif., February 5, 1964.

8. Jacobs, E., and King. H. E., "2.8-Minute Beamwidth Millimeter-Wave Antenna--Measurement and Evaluation", Aerospace Corp. Tech. Report TDR-469(5230-41)-1, El Segundo, Calif., March 26, 1965.

9. Grønlund, M. P. S., Wested, J., Vejgaard-Nielsen, N., "Nutating Subreflector in a Cassegrainian Antenna System", Danish Academy of Technical Sciences, Report No. P2114, Copenhagen, March 1, 1966.

10. Smith, I. D., "Zenith Tracking Radar", U. S. Patent Office disclosure 3,243,805, March 29, 1966.

11. Shimabukuro, F. I., "Propagation Through the Atmosphere at a Wavelength of 3.3 mm", IEEE Transactions on Antennas and Propagation, Vol. AP-14, No. 2, pp. 228-235, March 1966.

12. Baars, J. W. M., "Reduction of Tropospheric Noise Fluctuations at Centimetre Wavelengths", Nature, Vol. 212, pp. 494-495, October 29, 1966.

13. Baars, J. W. M., "Meteorological Influences on Radio Interferometer Phase Fluctuations", IEEE Transactions on Antennas and Propagation, Vol. AP-15, No. 4, pp. 582-584, July 1967.

14. Ananov, N.I., Basharinov, A. Ye., Kirdyasheve, K. P., Kutuza, B. G., "Fluctuations of RF Radiation of a Cloudy Atmosphere in the Millimeter Wavelength Region", Radio Engineering and Electronic Physics, Vol. 10, No. 11, pp. 1659-1664, November 1965.

15. Wulfsberg, K. N., "Atmospheric Attenuation at Millimeter Wavelength", Radio Science, Vol. 2 (New Series), No. 3, pp. 319-324, March 1967.

16. Rusch, W. V. T., "Scattering from a Hyperboloidal Reflector in a Cassegrainian Feed System", IEEE Transactions on Antennas and Propagation, Vol. AP-11, No. 4, pp. 414-421, July 1963.

17. Rusch, W. V. T., "Analytical Study of Wide-Angle and Back Lobe Paraboloidal Antennas", Jet Propulsion Lab., Pasadena, Calif., Research Summary 36-8, pp. 35-39, May 1, 1961.

18. Silver, S., Microwave Antenna Theory and Design, M.I.T. Rad. Lab Series, Vol. 12, McGraw-Hill Book Co., Inc., New York, N.Y., 1949.

19. Sancer, M.I., "An Analysis of the Vector Kirchhoff Equations and the Associated Boundary-Line Charge", Radio Science, Vol. 3 (New Series), No. 2, pp. 141-144, February 1968.

20. Love, A.W., "The Diagonal Horn Antenna", Microwave Journal, Vol. V, No. 3, pp. 117-122, March 1962.

21. Hannan, P. W., "Microwave Antennas Derived from the Cassegrain Telescope", IRE Transactions on Antennas and Propagation, Vol. AP-9, No. 2, pp. 140-153, March 1961.

22. Rusch, W. V. T., "Phase Error and Associated Cross-Polarization Effects in Cassegrainian-Fed Microwave Antennas", IEEE Transactions on Antennas and Propagation, Vol. AP-14, No. 3, pp. 266-275, May 1966.

23. Holt, F. S., "Application of Geometrical Optics to the Design and Analysis of Microwave Antennas", Air Force Cambridge Research Laboratories, Report No. AFCRL-67-0501, L. G. Hanscom Field, Bedford, Mass., September 1967.

24. Lo, Y. T., "On the Beam Deviation Factor of a Parabolic Reflector", IRE Transactions on Antennas and Propagation, Vol. AP-8, No. 3, pp. 347-349, May 1960.

25. Sandler, S. S., "Paraboloidal Reflector Patterns for Off-Axis Feed", IRE Transactions on Antennas and Propagation, Vol. AP-8, No. 4, pp. 368-379, July 1960.

26. Isber, A. M., "Obtaining Beam-Pointing Accuracy with Cassegrain Antennas", Microwaves, Vol. 6, No. 8, pp. 40-44, August 1967.

27. Reed, H. H., "Communication Satellite Ground Station Antennas", Microwave Journal, Vol. 10, No. 7, pp. 63-69, June 1967.

28. Strum, P., "Consideration in High-Sensitivity Microwave Radiometry", Proceedings of the IRE, Vol. 46, No. 1, pp. 43-53, January 1958.

29. Rusch, W. V. T., and Stelzried, C. T., "Observations of the Lunar Eclipse of December 19, 1964, at a Wavelength of 3.3 MM", The Astrophysical Journal, Vol. 148, No. 1, pp. 255-259, April 1967.

30. Coates, R. J., "Measurements of Solar Radiation and Atmospheric Attenuation at 4.3-Millimeters Wavelength", Proceedings of the IRE, Vol. 46, No. 1, pp. 122-126, January 1958.

31. Stelzried, C. T., and Rusch, W. V. T., "Improved Determination of Atmospheric Opacity from Radio Astronomy Measurements", Jour. Geophys. Research, Vol. 72, No. 9, pp. 2445-2447, January 1, 1967.

32. Low, F. J., and Davidson, A. W., "Lunar Observations at a Wavelength of One Millimeter", Astrophysical Journal, Vol. 142, pp. 1278-1282, 1965.

33. Kamenskaya, S. A., et al, "Observation of Radio Eclipses of the Moon at Millimeter Wavelengths", Izvestiya VUZ, Radiofizika, Vol. 8, No. 2, pp. 219-228, 1965.

34. Epstein, E. E., et al, "The Total Lunar Eclipse of December 30, 1963: Observations at 3.2 Millimeters", Aerospace Corporation, Report No. TDR-269(4250-41)-4, 1964.

35. Rusch, W. V. T., Slobin, S. D., Stelzried, C. T., and Sato, T., "Observations of the Total Lunar Eclipse of October 18, 1967 at a Wavelength of 3.33 MM", to be published in the Astrophysical Journal, March 1969.

APPENDIX A

Tilted Hyperboloid Scattering Computer Program Listing

```
C     SCATTERING FROM A TILTED HYPERBOLOID
C
//SLOBIN JOB -YAT001R1,30,50-,OSLOBINO,MSGLEVEL 1
//       EXEC FORTRAN
//FORT.SYSIN DD *
      DIMENSION SUM(4),SUMT(4),DATE(18)                                 00000020
C     DIMENSION SUM(4),SUMT(4),DATE(18)                                 00000030
1     READ (5,1000,END=500) DATE
      READ (5,1001)LOOPA,LOOPB,IPRNT                                    00000050
      READ (5,1002)THES,DELTHE,THENUM                                   00000060
      READ (5,1002)PHIS,DELPHI,PHINUM                                   00000070
      READ (5,1002)THEO,CEP,E,ALPHA,CAYX,CAYZ,CAYOF                     00000080
      LPRNT=0                                                           00000090
      LOOPA=(LOOPA/2)*2                                                 00000100
      LOOPB=(LOOPB/2)*2                                                 00000110
      PI=3.14159265                                                     00000120
      PI2=6.2831853                                                     00000130
      PIH=1.5707963                                                     00000140
      DEG=.174532925E-01                                                00000150
      RAD=57.2957795                                                    00000160
      WRITE (6,4000)DATE                                                00000170
      WRITE (6,5000)                                                    00000180
      WRITE (6,5001)THES,DELTHE                                         00000190
      WRITE (6,5002)PHIS,DELPHI                                         00000200
      WRITE (6,5003)THEO,CEP,E,ALPHA                                    00000210
      WRITE (6,5004)CAYX,CAYZ,CAYOF                                     00000220
      ALPHA=ALPHA*DEG                                                   00000230
      THES=THES*DEG                                                     00000240
      DELTHE=DELTHE*DEG                                                 00000250
      PHIS=PHIS*DEG                                                     00000260
      THEO=THEO*DEG                                                     00000270
      DELPHI=DELPHI*DEG                                                 00000280
      DELTH3=(PI-THEO)/FLOAT(LOOPA)                                     00000290
      TEMP=DELTH3*RAD                                                   00000300
      WRITE (6,5005)DELTH3,TEMP                                         00000310
      SINA=SIN(ALPHA)                                                   00000320
      COSA=COS(ALPHA)                                                   00000330
      R1=DELTH3/3.0                                                     00000340
      JFK=THENUM                                                        00000350
      LBJ=PHINUM                                                        00000360
      A=LOOPA                                                           00000370
      B=LOOPB                                                           00000380
      DEL=(B-4.0)/A                                                     00000390
      LOOPA=LOOPA+1                                                     00000400
      DO 900 L=1,LBJ                                                    00000410
      PHI=PHIS+DELPHI*FLOAT(L-1)                                        00000420
      TEMP=PHI*RAD                                                      00000430
      WRITE (6,6000)PHI,TEMP                                            00000440
      WRITE (6,6001)                                                    00000450
      WRITE (6,6002)                                                    00000460
      SINP=SIN(PHI)                                                     00000470
      COSP=COS(PHI)                                                     00000480
      DO 800 K=1,JFK                                                    00000490
      THE=THES+DELTHE*FLOAT(K-1)                                        00000500
      SINT=SIN(THE)                                                     00000510
      COST=COS(THE)                                                     00000520
      CTCP=COST*COSP                                                    00000530
      DO 30 I=1,4                                                       00000540
   30 SUMT(I)=0.0                                                       00000550
      CTSP=COST*SINP                                                    00000560
      IF(IPRNT)34,35,34                                                 00000570
```

APPENDIX A (cont.)

```
 34 LRUN=1                                                                  00000580
    WRITE (6,7000)LRUN,SINA,SINP,SINT,CTSP,COSA,COSP, COST,CTCP,THE,DE00000590
   1L                                                                       00000600
 35 LL=1                                                                    00000610
    DO 600 J=1,LOOPA                                                        00000620
    FLOT=J-1                                                                00000630
    THE3=THEO+DELTH3*FLOT                                                   00000640
    NN=B+0.5-DEL*FLOT                                                       00000650
    NN=(NN/2)*2                                                             00000660
    DELPH3=PI2/FLOAT(NN)                                                    00000670
    R2=DELPH3/3.0                                                           00000680
    NN=NN+1                                                                 00000690
    SINT3=SIN(THE3)                                                         00000700
    COST3=COS(THE3)                                                         00000710
    T1=1.0+E*COST3                                                          00000720
    CAYRO3=-CEP/T1                                                          00000730
    CAYZ3=CAYRO3*COST3                                                      00000740
    ECOST3=E+COST3                                                          00000750
    SAECT3=SINA*ECOST3                                                      00000760
    FTHETA=SINT3/(T1*T1)                                                    00000770
    R3=FTHETA*R2                                                            00000780
    R4=R3*2.0                                                               00000790
    R5=R3*4.0                                                               00000800
    DO 40 I=1,4                                                             00000810
 40 SUM(I)=0.0                                                              00000820
    IF(IPRNT)41,42,41                                                       00000830
 41 LRUN=2                                                                  00000840
    TEMP=DELPH3*RAD                                                         00000850
    WRITE (6,7001)LRUN,THE3,T1,CAYRO3,R3,SINT3,ECOST3, CAYZ3,R4,COST3,00000860
   1SAECT3,FTHETA,R5,DELPH3,TEMP                                            00000870
 42 KK=1                                                                    00000880
    DO 400 I=1,NN                                                           00000890
    PHI3=DELPH3*FLOAT(I-1)                                                  00000900
    SINP3=SIN(PHI3)                                                         00000910
    COSP3=COS(PHI3)                                                         00000920
    ST3CP3=SINT3*COSP3                                                      00000930
    ST3SP3=SINT3*SINP3                                                      00000940
    CAYX3=CAYRO3*ST3CP3                                                     00000950
    CAYY3=CAYRO3*ST3SP3                                                     00000960
    CAYX1=CAYX3*COSA-CAYZ3*SINA-CAYX                                        00000970
    CAYY1=CAYY3                                                             00000980
    CAYZ1=CAYX3*SINA+CAYZ3*COSA-CAYZ                                        00000990
    T2=CAYX1**2+CAYY1**2                                                    00001000
    CAYRO1=SQRT(T2+CAYZ1**2)                                                00001010
    T3=SQRT(T2)                                                             00001020
    THE1=PI-ATAN(T3/ABS(CAYZ1))                                             00001030
    PHI1=ARCOS(ABS(CAYX1)/T3)                                               00001040
    IF(CAYX1)70,50,50                                                       00001050
 50 IF(CAYY1)60,100,100                                                     00001060
 60 PHI1=PI2-PHI1                                                           00001070
    GO TO 100                                                               00001080
 70 IF(CAYY1)80,90,90                                                       00001090
 80 PHI1=PI+PHI1                                                            00001100
    GO TO 100                                                               00001110
 90 PHI1=PI-PHI1                                                            00001120
100 CAYX2=CAYX1                                                             00001130
    CAYY2=CAYY1                                                             00001140
    CAYZ2=CAYZ1+CAYOF                                                       00001150
    CAYRO2=SQRT(T2+CAYZ2**2)                                                00001160
    IF(CAYZ2)110,130,120                                                    00001170
110 THE2=PI-ATAN(T3/ABS(CAYZ2))                                             00001180
```

APPENDIX A (cont.)

```
      GO TO 140                                                          00001190
  120 THE2=ATAN(T3/CAYZ2)                                                00001200
      GO TO 140                                                          00001210
  130 THE2=PIH                                                           00001220
  140 PHI2=PHI1                                                          00001230
      CC=COSA*ST3CP3-SINA*ECOST3                                         00001240
      DD=ST3SP3                                                          00001250
      EE=SINA*ST3CP3+COSA*ECOST3                                         00001260
      SINT1=SIN(THE1)                                                    00001270
      COST1=COS(THE1)                                                    00001280
      SINP1=SIN(PHI1)                                                    00001290
      COSP1=COS(PHI1)                                                    00001300
      FF=(1.0+COST1)*SINP1*COSP1                                         00001310
      GG=COST1*SINP1*SINP1-COSP1*COSP1                                   00001320
      HH=-SINT1*SINP1                                                    00001330
      T4=DD*HH-EE*GG                                                     00001340
      T5=EE*FF-CC*HH                                                     00001350
      T6=CC*GG-DD*FF                                                     00001360
      AM=T4*CTCP+T5*CTSP-T6*SINT                                         00001370
      AN=T5*COSP-T4*SINP                                                 00001380
      LMAG=0                                                             00001390
      CALL OPTION(THE1,ANS,L,LMAG)                                       00001400
      AA=ANS                                                             00001410
      LMAG=1                                                             00001420
      CALL OPTION(THE1,ANS,L,LMAG)                                       00001430
      BB=ANS                                                             00001440
      T7=CAYR03/CAYR01                                                   00001450
      G1=T7*AM                                                           00001460
      G2=T7*AN                                                           00001470
      T8=COS(PHI-PHI2)                                                   00001480
      T9=SINT*SIN(THE2)                                                  00001490
      S1=COST*COS(THE2)                                                  00001500
      H=CAYR02*(T9*T8+S1)-CAYR01                                         00001510
      SINH=SIN(H)                                                        00001520
      COSH=COS(H)                                                        00001530
      S2=AA*COSH-BB*SINH                                                 00001540
      S3=BB*COSH+AA*SINH                                                 00001550
      IF(I-LOOPB)170,200,170                                             00001560
  170 GO TO(200,220,240),KK                                              00001570
  200 SUM(1)=SUM(1)+G1*S2                                                00001580
      SUM(2)=SUM(2)+G1*S3                                                00001590
      SUM(3)=SUM(3)+G2*S2                                                00001600
      SUM(4)=SUM(4)+G2*S3                                                00001610
      KK=3                                                               00001620
      GO TO 300                                                          00001630
  220 SUM(1)=SUM(1)+G1*S2*2.0                                            00001640
      SUM(2)=SUM(2)+G1*S3*2.0                                            00001650
      SUM(3)=SUM(3)+G2*S2*2.0                                            00001660
      SUM(4)=SUM(4)+G2*S3*2.0                                            00001670
      KK=3                                                               00001680
      GO TO 300                                                          00001690
  240 SUM(1)=SUM(1)+G1*S2*4.0                                            00001700
      SUM(2)=SUM(2)+G1*S3*4.0                                            00001710
      SUM(3)=SUM(3)+G2*S2*4.0                                            00001720
      SUM(4)=SUM(4)+G2*S3*4.0                                            00001730
      KK=2                                                               00001740
  300 IF(IPRNT)305,400,305                                               00001750
  305 LRUN=3                                                             00001760
      WRITE (6,7002)LRUN,PHI3,THE1,SINT1,CAYX1,SINP3,THE2, COST1,CAYY1,C00001770
     1OSP3,PHI1,SINP1,CAYZ1                                              00001780
      WRITE (6,7003)ST3CP3,PHI2,COSP1,T2,ST3SP3,CAYX3, CAYY3,T3,T4,T5,T600001790
```

APPENDIX A (cont.)

```
     1,T7                                                                    00001800
      WRITE (6,7004)T8,T9,S1,S2,S3,CAYX2,CAYRO1,AA,H, CAYY2,G1,BB            00001810
      WRITE (6,7005)SINH,CAYZ2,G2,CC,COSH,AM,AN, DD,EE,FF,GG,HH,CAYRO2       00001820
      WRITE (6,7006)SUM(1),SUM(2),SUM(3),SUM(4), SUMT(1),SUMT(2),SUMT(3)     00001830
     1,SUMT(4)                                                               00001840
      LPRNT=LPRNT+1                                                          00001850
      IF(LPRNT-IPRNT)400,400,310                                             00001860
  310 IPRNT=0                                                                00001870
  400 CONTINUE                                                               00001880
      IF(J-LOOPA)420,440,420                                                 00001890
  420 GO TO(440,460,480),LL                                                  00001900
  440 SUMT(1)=SUMT(1)+SUM(1)*R3                                              00001910
      SUMT(2)=SUMT(2)+SUM(2)*R3                                              00001920
      SUMT(3)=SUMT(3)+SUM(3)*R3                                              00001930
      SUMT(4)=SUMT(4)+SUM(4)*R3                                              00001940
      LL=3                                                                   00001950
      GO TO 600                                                              00001960
  460 SUMT(1)=SUMT(1)+SUM(1)*R4                                              00001970
      SUMT(2)=SUMT(2)+SUM(2)*R4                                              00001980
      SUMT(3)=SUMT(3)+SUM(3)*R4                                              00001990
      SUMT(4)=SUMT(4)+SUM(4)*R4                                              00002000
      LL=3                                                                   00002010
      GO TO 600                                                              00002020
  480 SUMT(1)=SUMT(1)+SUM(1)*R5                                              00002030
      SUMT(2)=SUMT(2)+SUM(2)*R5                                              00002040
      SUMT(3)=SUMT(3)+SUM(3)*R5                                              00002050
      SUMT(4)=SUMT(4)+SUM(4)*R5                                              00002060
      LL=2                                                                   00002070
  600 CONTINUE                                                               00002080
      DO 650 I=1,4                                                           00002090
  650 SUMT(I)=SUMT(I)*R1                                                     00002100
      TEMP=THE*RAD                                                           00002110
      CALL PHASE(SUMT(1),SUMT(2),TEMS)                                       00002120
      CALL PHASE(SUMT(3),SUMT(4),TEMT)                                       00002130
      T1=SQRT(SUMT(1)**2+SUMT(2)**2)                                         00002140
      T2=SQRT(SUMT(3)**2+SUMT(4)**2)                                         00002150
      WRITE (6,6003)TEMP,SUMT(1),SUMT(2),T1,TEMS, SUMT(3),SUMT(4),T2,TEM    00002160
     1T                                                                      00002170
  800 CONTINUE                                                               00002180
  900 CONTINUE                                                               00002190
      GO TO 1                                                                00002200
 1000 FORMAT(18A4)
 1001 FORMAT(14I5)                                                           00002220
 1002 FORMAT(7F10.0)                                                         00002230
 4000 FORMAT(1H1,30X,18A4)                                                   00002240
 5000 FORMAT(39HOINPUT PARAMETERS AND CONTROL CONSTANTS)                     00002250
 5001 FORMAT(7HOTHETA=F12.5,8H DEGREES,10X,10HINCREMENT=F12.5)               00002260
 5002 FORMAT(5H PHI=F12.5,8H DEGREES,12X,10HINCREMENT=F12.5)                 00002270
 5003 FORMAT(10HOTHETA(0)=F12.5,10X,3HKEP,6X,1H=,F12.5,10X,1HE,8X,1H=,       00002280
     1F12.5,10X,10HALPHA     =F12.5)                                         00002290
 5004 FORMAT(3H KX,6X,1H=F12.5,10X,2HKZ,7X,1H=F12.5,10X,3HKOF,6X,            00002300
     11H=F12.5)                                                              00002310
 5005 FORMAT(21HOOUTER INTEGRAL STEP=F12.5,10H RADIANS =F12.5,8H DEGREES00002320
     1)                                                                      00002330
 6000 FORMAT(5H1PHI=F12.5,9H RADIANS=F12.5,8H DEGREES)                       00002340
 6001 FORMAT(7HO THETA,28X,7HE THETA,50X,5HE PHI)                            00002350
 6002 FORMAT(8HODEGREES,2(8X,4HREAL,8X,9HIMAGINARY,6X,9HMAGNITUDE,          00002360
     16X,6HPHASE ))                                                          00002370
 6003 FORMAT(F8.3,2(3F15.8,F11.3))                                           00002380
 7000 FORMAT(1HO,I2,4X,7HSINA  =F15.8,8X,7HSINP  =F15.8,8X,7HSINT  =F15.00002390
     18,8X,7HCTSP  =F15.8/7X,7HCOSA  =F15.8,8X,7HCOSP  =F15.8,8X,7HCOST 00002400
```

APPENDIX A (cont.)

```
     2 =F15.8,8X,7HCTCP  =F15.8/7X,7HTHE   =F15.8,8X,7HDEL   =F15.8)     00002410
 7001 FORMAT(1HO,I2,4X,7HTHE3  =F15.8,8X,7HT1    =F15.8,8X,7HCAYRO3=F15.00002420
     18,8X,7HR3    =F15.8/7X,7HSINT3 =F15.8,8X,7HECOST3=F15.8,8X,7HCAYZ300002430
     2 =F15.8,8X,7HR4    =F15.8/7X,7HCOST3 =F15.8,8X,7HSAECT3=F15.8,8X, 00002440
     37HFTHETA=F15.8,8X,7HR5    =F15.8/7X,7HDELPH3=F15.8,8X,7HIN DFG=F1500002450
     4.8)                                                               00002460
 7002 FORMAT(1HO,I2,4X,7HPHI3  =F15.8,8X,7HTHE1  =F15.8,8X,7HSINT1 =F15.00002470
     18,8X,7HCAYX1 =F15.8/7X,7HSINP3 =F15.8,8X,7HTHE2  =F15.8,8X,7HCOST100002480
     2 =F15.8,8X,7HCAYY1 =F15.8/7X,7HCOSP3 =F15.8,8X,7HPHI1  =F15.8,8X, 00002490
     37HSINP1 =F15.8,8X,7HCAYZ1 =F15.8)                                 00002500
 7003 FORMAT(7X,7HST3CP3=F15.8,8X,7HPHI2  =F15.8,8X,7HCOSP1 =F15.8,8X,7H00002510
     1T2    =F15.8/7X,7HST3SP3=F15.8,8X,7HCAYX3 =F15.8,8X,7HCAYY3 =F15.800002520
     2,8X,7HT3     =F15.8/7X,7HT4     =F15.8,8X,7HT5     =F15.8,8X,7H16     00002530
     3=F15.8,8X,7HT7     =F15.8)                                        00002540
 7004 FORMAT(7X,7HT8     =F15.8,8X,7HT9     =F15.8,8X,7HS1     =F15.8,8X,7H00002550
     1S2     =F15.8/7X,7HS3     =F15.8,8X,7HCAYX2 =F15.8,8X,7HCAYRO1=F15.800002560
     2,8X,7HAA     =F15.8/7X,7HH      =F15.8,8X,7HCAYY2 =F15.8,8X,7HG1     00002570
     3=F15.8,8X,7HBB     =F15.8)                                        00002580
 7005 FORMAT(7X,7HSINH  =F15.8,8X,7HCAYZ2 =F15.8,8X,7HG2     =F15.8,8X,7H00002590
     1CC     =F15.8/7X,7HCOSH  =F15.8,8X,7HAM     =F15.8,8X,7HAN     =F15.800002600
     2,8X,7HDD     =F15.8/7X,7HEE     =F15.8,8X,7HFF     =F15.8,8X,7HGG     00002610
     3=F15.8,8X,7HHH     =F15.8/7X,7HCAYRO2=F15.8)                      00002620
 7006 FORMAT(7X,7HSUM  1=F15.8,8X,7HSUM  2=F15.8,8X,7HSUM  3=F15.8,8X,7H00002630
     1SUM  4=F15.8/7X,7HSUMT 1=F15.8,8X,7HSUMT 2=F15.8,8X,7HSUMT 3=F15.800002640
     2,8X,7HSUMT 4=F15.8)                                               00002650
500   STOP
      END                                                               00002660

      SUBROUTINE PHASE(A,B,C)                                           PHAS0020
      C=0.0                                                             PHAS0030
      IF(A)20,5,20                                                      PHAS0040
    5 IF(B)75,100,100                                                   PHAS0050
   20 TEMP=B/A                                                          PHAS0060
      C=ATAN(ABS(TEMP))*57.2957795                                      PHAS0070
      IF(TEMP)30,60,70                                                  PHAS0080
   30 IF(B)50,50,40                                                     PHAS0090
   40 C=180.0-C                                                         PHAS0100
      GO TO 100                                                         PHAS0110
   50 C=360.0-C                                                         PHAS0120
      GO TO 100                                                         PHAS0130
   60 IF(A)75,100,100                                                   PHAS0140
   70 IF(B)75,75,100                                                    PHAS0150
   75 C=180.0+C                                                         PHAS0160
  100 RETURN                                                            PHAS0170
      END                                                               PHAS0180

      SUBROUTINE OPTION(THE1,ANS,L,LMAG)
      ANS=0.0
      IF(LMAG)5,5,30
    5 X=SIN(THE1)
      Y=13.375*X
      Z=SIN(Y)*COS(Y)
      V=(1.0-72.48*X*X)*Y
      ANS=Z/V
   30 RETURN
      END

/*
//GO.SYSIN DD *
/*
/*
```

APPENDIX A (cont.)

Definitions used in scattering calculations

Following Equations (2-32), the following definitions may be made:

$$f(\theta_3) = \frac{\sin \theta_3}{(1+e \cos \theta_3)^2}$$

$$g_1(\theta_3,\varphi_3) = \frac{\rho_3}{\rho_1} \cdot M(\theta_3,\varphi_3)$$

$$g_2(\theta_3,\varphi_3) = \frac{\rho_3}{\rho_1} \cdot N(\theta_3,\varphi_3)$$

$$h(\theta_3,\varphi_3) = k\rho_2\left[\sin\theta \sin\theta_2 \cos(\varphi-\varphi_2) + \cos\theta \cos\theta_2\right] - k\rho_1$$

Equations (2-32) then become:

$$E_\theta = \int_{\theta_o}^{\pi} f(\theta_3) \int_o^{2\pi} (A+jB) g_1(\theta_3,\varphi_3) e^{jh(\theta_3,\varphi_3)} d\varphi_3 \, d\theta_3$$

$$E_\varphi = \int_{\theta_o}^{\pi} f(\theta_3) \int_o^{2\pi} (A+jB) g_2(\theta_3,\varphi_3) e^{jh(\theta_3,\varphi_3)} d\varphi_3 \, d\theta_3$$

The real and imaginary parts of E_θ and E_φ become:

$$Re[E_\theta] = \int_{\theta_o}^{\pi} f(\theta_3) \int_o^{2\pi} g_1(\theta_3,\varphi_3)\left[A \cosh(\theta_3,\varphi_3) - B \sinh(\theta_3,\varphi_3)\right] d\varphi_3 \, d\theta_3$$

APPENDIX A (cont.)

Definitions (cont.)

$$\mathrm{Im}[E_\theta] = \int_{\theta_o}^{\pi} f(\theta_3) \int_o^{2\pi} g_1(\theta_3,\varphi_3)\left[B\cosh(\theta_3,\varphi_3) + A\sinh(\theta_3,\varphi_3)\right] d\varphi_3\, d\theta_3$$

$$\mathrm{Re}[E_\varphi] = \int_{\theta_o}^{\pi} f(\theta_3) \int_o^{2\pi} g_2(\theta_3,\varphi_3)\left[A\cosh(\theta_3,\varphi_3) - B\sinh(\theta_3,\varphi_3)\right] d\varphi_3\, d\theta_3$$

$$\mathrm{Im}[E_\varphi] = \int_{\theta_o}^{\pi} f(\theta_3) \int_o^{2\pi} g_2(\theta_3,\varphi_3)\left[B\cosh(\theta_3,\varphi_3) + A\sinh(\theta_3,\varphi_3)\right] d\varphi_3\, d\theta_3$$

Glossary of Terms

SINA = $\sin\alpha$

CØSA = $\cos\alpha$

SINP = $\sin\varphi$

CØSP = $\cos\varphi$

SINT = $\sin\theta$

CØST = $\cos\theta$

CTSP = $\cos\theta \sin\varphi$

CTCP = $\cos\theta \cos\varphi$

THE = θ

ALPHA = α

APPENDIX A (cont.)

Glossary (cont.)

DEL = Δ, used to control decreasing step size for inner integral

THE3 = θ_3

SINT3 = $\sin \theta_3$

CØST3 = $\cos \theta_3$

DELPH3 = $\Delta\varphi_3$, inner integral step size

T1 = $1 + e \cos \theta_3$

ECØST3 = $e + \cos \theta_3$

SAECT3 = $\sin \alpha (e + \cos \theta_3)$

FTHETA = $\sin \theta_3 / (1+e \cos \theta_3)^2$

R3 = FTHETA $\cdot$ $(\Delta\varphi_3/3)$, for Simpson's Rule

R4 = 2 (R_3), for Simpson's Rule

R5 = 4 (R_3), for Simpson's Rule

CAYRØ3 = $-kep/(1+e \cos \theta_3)$

CAYZ3 = $\cos \theta_3 [-kep/(1+e \cos \theta_3)]$

PHI3 = φ_3

SINP3 = $\sin \varphi_3$

CØSP3 = $\cos \varphi_3$

ST3CP3 = $\sin \theta_3 \cos \varphi_3$

ST3SP3 = $\sin \theta_3 \sin \varphi_3$

APPENDIX A (cont.)

Glossary (cont.)

THE1 = θ_1

THE2 = θ_2

PHI1 = φ_1

PHI2 = φ_2

SINT1 = $\sin \theta_1$

CØST1 = $\cos \theta_1$

SINP1 = $\sin \varphi_1$

CØSP1 = $\cos \varphi_1$

CAYX1 = kx_1

CAYY1 = ky_1

CAYZ1 = kz_1

CAYX2 = kx_2

CAYY2 = ky_2

CAYZ2 = kz_2

CAYX3 = kx_3

CAYY3 = ky_3

CAYZ3 = kz_3

T2 = $(kx_1)^2 + (ky_1)^2$

T3 = $[(kx_1)^2 + (ky_1)^2]^{\frac{1}{2}}$

CAYRØ1 = $[(kx_1)^2 + (ky_1)^2 + (kz_1)^2]^{\frac{1}{2}} = k\rho_1$

APPENDIX A (cont.)

Glossary (cont.)

$CAYR\phi 2 = [(kx_1)^2 + (ky_1)^2 + (kz_2)^2] = k\rho_2$

$CC = \cos\alpha(\sin\theta_3 \cos\varphi_3) - \sin\alpha(e + \cos\theta_3)$

$DD = \sin\theta_3 \sin\varphi_3$

$EE = \sin\alpha(\sin\theta_3 \cos\varphi_3) + \cos\alpha(e + \cos\theta_3)$

$FF = (1 + \cos\theta_1) \sin\varphi_1 \cos\varphi_1$

$GG = \cos\theta_1 \sin^2\varphi_1 - \cos^2\varphi_1$

$HH = -\sin\theta_1 \sin\varphi_1$

$T4 = (DD)(HH) - (EE)(GG)$

$T5 = (EE)(FF) - (CC)(HH)$

$T6 = (CC)(GG) - (DD)(FF)$

$AM = (T4)\cos\theta\cos\varphi + (T5)\cos\theta\sin\varphi - (T6)\sin\theta$

$AN = (T5)\cos\varphi - (T4)\sin\varphi$

$AA = A(\theta_1)$, real

$BB = A(\theta_1)$, imaginary

$T7 = k\rho_3/k\rho_1$

$T8 = \cos(\varphi - \varphi_2)$

$T9 = \sin\theta \sin\theta_2$

$S1 = \cos\theta \cos\theta_2$

$G1 = AM(\rho_3/\rho_1)$

APPENDIX A (cont.)

Glossary (cont.)

$G2 = AN(\rho_3/\rho_1)$

$H = k\rho_2[T9 \cdot T8 + S1] - k\rho_1$

SINH = sin H

CØSH = cos H

$S2 = AA \cdot \cos H - BB \cdot \sin H$

$S3 = BB \cdot \cos H + AA \cdot \sin H$

Input Cards

Card 1 - any information whatsoever; for printout only

Card 2 - LØØPA - number of intervals, outer integral (θ_3), integer ending in column 5

LØØPB - number of intervals, inner integral, initially (φ_3), integer ending in column 10

IPRNT - number of diagnostic printouts within inner integral, or zero if none wanted, integer ending in column 15

Card 3 - THES - initial value of θ parameter, decimal number, columns 1 - 10

DELTHE - θ parameter interval, decimal number, columns 11-20

THENUM - number of θ's desired, integer ending in column 30

Card 4 - PHIS - initial value of φ parameter, decimal number, columns 1 - 10

DELPHI - φ parameter interval, decimal number, columns 11-20

APPENDIX A (cont.)

Input Cards (cont.)

PHINUM - number of φ's desired, integer ending in column 30

Card 5 - THEO - θ_o, lower limit of integration, outer integral, decimal number, columns 1-10

CEP - kep, decimal number, columns 11-20

E - e, hyperboloid eccentricity, decimal number, columns 21-30

ALPHA - α, hyperboloid tilt angle, decimal number, columns 31-40

CAYX - kX, decimal number, columns 41-50

CAYZ - kZ, decimal number, columns 51-60

CAYØF - $k\overline{OF}$, decimal number, columns 61-70

APPENDIX B

Geometrical Equivalence Between Intersection and Phase Center of Adjacent Reflected Rays

It is desired to show that the intersection and phase center of reflected rays are coincident in the limit of adjacent rays.

Consider Figure B-1 in which incident Rays 1 and 2 are reflected from the surface S_o. Rays 1' and 2' are the reflected rays. Point P is the intersection of the virtual rays. $\overline{BC} \perp$ Ray 2', and $\overline{AD} \perp$ Ray 1. For adjacent rays, $\overline{AC}$ is small, $\overline{PC} \approx \overline{PB}$, and point P may be regarded as the phase center of the reflected waves if it can be shown that the reflected waves have the same phase at point B and C; i.e., that $\overline{QAB} = \overline{QC}$.

$$\overline{QAB} = \overline{QA} + \overline{AB}$$
$$\overline{QC} = \overline{QD} + \overline{DC} \qquad \text{(B-1)}$$

As $\overline{AC} \rightarrow 0$, $\overline{QA} \rightarrow \overline{QD}$. Therefore if $\overline{AB} = \overline{DC}$, then $\overline{QAB} = \overline{QC}$ (from Equation B-1).

If Rays 1 and 2 are close together, then angle CAD = angle of incidence of Ray 1, and angle ACB = angle of reflection of Ray 2. As $\overline{AC} \rightarrow 0$, angle CAD $\rightarrow$ angle ACB. Similarly, it is seen that angle ACD $\rightarrow$ angle CAB. Therefore in the limit of very close rays,

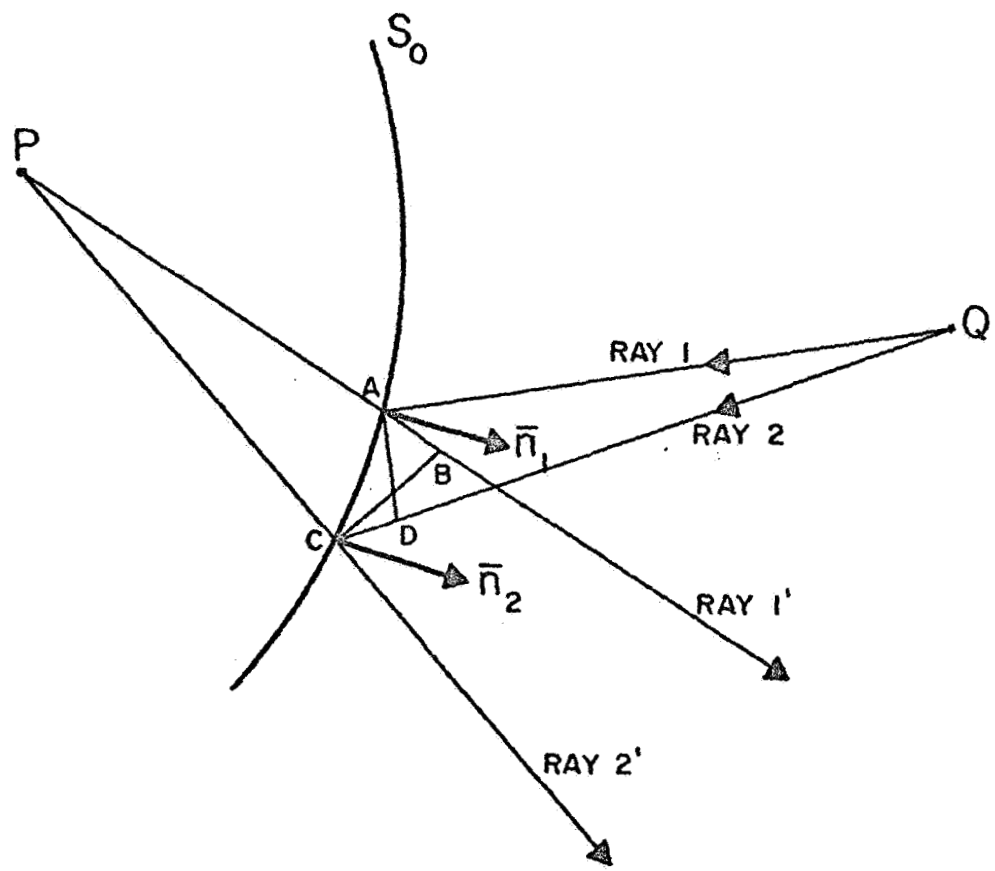

Figure B-1

triangles ABC and ADC are congruent and $\overline{AB} = \overline{DC}$. Therefore, $\overline{QAB} = \overline{QC}$ and P may be regarded as the phase center and intersection of adjacent virtual rays.

APPENDIX C

Caustic Curve Determination Computer Program Listing

```
C    CAUSTIC CURVE AND GEOMETRICAL OPTICS PHASE DETERMINATION
C    IBM 1620
C
C
C    DESCRIPTION OF POINT ON SURFACE OF HYPERBOLOID AND DERIVATIVES
C    RS MEASURED PERPENDICULAR TO Z-AXIS, PHI AROUND Z-AXIS
       RS=0.0
       PHI=0.0
       P=PHI*(3.14159/180.0)
C
C    A AND C ARE CONSTANTS OF THE HYPERBOLOID
       A=9.63107
       C=12.8
C
    10 XS=RS*COS(P)
       YS=RS*SIN(P)
       ZS=C-A*SQRT(1.0+(RS*RS)/(C*C-A*A))
       RRS = SQRT(XS*XS + YS*YS + ZS*ZS)
       DXSDR=COS(P)
       DYSDR=SIN(P)
       DZSDR=-0.5*A*(1.0/SQRT(1.0+(RS*RS)/(C*C-A*A)))*((2.*RS)/(C*C-A*A))
       DXSDP=-RS*SIN(P)
       DYSDP=RS*COS(P)
       DZSDP=0.0
C
       AXS=XS/SQRT(RS*RS+ZS*ZS)
       AYS=YS/SQRT(RS*RS+ZS*ZS)
       AZS=ZS/SQRT(RS*RS+ZS*ZS)
C
C    DESCRIPTION OF SOURCE POSITION AND DERIVATIVES
       XQ=0.82762
       YQ=0.0
       ZQ=25.58512
C    RSQ IS DISTANCE BETWEEN SOURCE AND POINT ON HYPERBOLOID
       RSQ=SQRT((XS-XQ)*(XS-XQ)+(YS-YQ)*(YS-YQ)+(ZS-ZQ)*(ZS-ZQ))
       DXQDR=0.0
       DYQDR=0.0
       DZQDR=0.0
       DXQDP=0.0
       DYQDP=0.0
       DZQDP=0.0
C
C    CONSTANTS ASSOCIATED WITH VARIOUS TERMS
C    C1 AND C2 ARE ASSOCIATED WITH COMPONENTS ALPHA OF REFLECTED RAY
       C1=8.0/((A*A-C*C)*(A*A-C*C))
       C2=8.0/((A*A)*(A*A-C*C))
C    C3 IS ASSOCIATED WITH THE VARIOUS ALPHAS
       C3=(A*A-C*C)/(A*A)
C    C4 AND C5 ARE CONSTANTS ASSOCIATED WITH NORMAL TO HYPERBOLOID
       C4 = (2.0)/(C*C-A*A)
       C5=(2.0)/(A*A)

C
```

APPENDIX C (cont.)

```
C   COMPONENTS OF THE NORMAL TO HYPERBOLOID AND DERIVATIVES
      XNORM=C4*XS
      YNORM=C4*YS
      ZNORM=C5*(C-ZS)
      DXNDR=C4*DXSDR
      DYNDR=C4*DYSDR
      DZNDR=-C5*DZSDR
      DXNDP=C4*DXSDP
      DYNDP=C4*DYSDP
      DZNDP=-C5*DZSDP
C
C   G1 OCCURS IN EACH COMPONENT ALPHA OF THE REFLECTED RAY
      G1=XS*XS+YS*YS-XS*XQ-YS*YQ+C3*ZS*ZS-C3*ZS*ZQ-C3*ZS*C+C3*ZQ*C
      DG1DR=2.0*XS*DXSDR+2.0*YS*DYSDR-XS*DXQDR-XQ*DXSDR-YS*DYQDR-
     1 YQ*DYSDR+2.0*C3*ZS*DZSDR-C3*ZS*DZQDR-C3*ZQ*DZSDR-C3*C*DZSDR+
     2 C3*C*DZQDR
      DG1DP=2.0*XS*DXSDP+2.0*YS*DYSDP-XS*DXQDP-XQ*DXSDP-YS*DYQDP-
     1 YQ*DYSDP+2.0*C3*ZS*DZSDP-C3*ZS*DZQDP-C3*ZQ*DZSDP-C3*C*DZSDP+
     2 C3*C*DZQDP
C   DG2 IS DENOMINATOR OF G2
      DG2=XNORM*XNORM+YNORM*YNORM+ZNORM*ZNORM
C   G2 IS THE SQUARE OF THE NORMALIZING FACTOR OF THE NORMAL
      G2=1.0/DG2
      DDG2DR=2.0*XNORM*DXNDR+2.0*YNORM*DYNDR+2.0*ZNORM*DZNDR
      DDG2DP=2.0*XNORM*DXNDP+2.0*YNORM*DYNDP+2.0*ZNORM*DZNDP
      DG2DR=-(1.0)*(DDG2DR)/(DG2*DG2)
      DG2DP=-(1.0)*(DDG2DP)/(DG2*DG2)
      G3=1.0/RSQ
      DRSQDR=((XS-XQ)*(DXSDR-DXQDR)+(YS-YQ)*(DYSDR-DYQDR)+(ZS-ZQ)*
     1 (DZSDR-DZQDR))/(RSQ)
      DRSQDP=((XS-XQ)*(DXSDP-DXQDP)+(YS-YQ)*(DYSDP-DYQDP)+(ZS-ZQ)*
     1 (DZSDP-DZQDP))/(RSQ)
      DG3DR=-DRSQDR/(RSQ*RSQ)
      DG3DP=-DRSQDP/(RSQ*RSQ)
C
C   AX,AY,AZ ARE COMPONENTS OF THE REFLECTED RAY
      AX=G3*(XS-XQ-C1*G2*XS*G1)
      AY=G3*(YS-YQ-C1*G2*YS*G1)
      AZ=G3*(ZS-ZQ-C2*G2*(ZS-C)*G1)
C   DERIVATIVES OF COMPONENTS OF REFLECTED RAY WITH RESPECT TO R AND PHI
      DAXDR=G3*DXSDR+XS*DG3DR-G3*DXQDR-XQ*DG3DR-C1*DG3DR*G2*XS*G1
     1 -C1*G3*DG2DR*XS*G1-C1*G3*G2*DXSDR*G1-C1*G3*G2*XS*DG1DR
      DAYDR=G3*DYSDR+YS*DG3DR-G3*DYQDR-YQ*DG3DR-C1*DG3DR*G2*YS*G1
     1 -C1*G3*DG2DR*YS*G1-C1*G3*G2*DYSDR*G1-C1*G3*G2*YS*DG1DR
      DAZDR=G3*DZSDR+ZS*DG3DR-G3*DZQDR-ZQ*DG3DR-C2*DG3DR*G2*(ZS-C)*G1
     1 -C2*G3*DG2DR*(ZS-C)*G1-C2*G3*G2*DZSDR*G1-C2*G3*G2*(ZS-C)*DG1DR
      DAXDP=G3*DXSDP+XS*DG3DP-G3*DXQDP-XQ*DG3DP-C1*DG3DP*G2*XS*G1
     1 -C1*G3*DG2DP*XS*G1-C1*G3*G2*DXSDP*G1-C1*G3*G2*XS*DG1DP
      DAYDP=G3*DYSDP+YS*DG3DP-G3*DYQDP-YQ*DG3DP-C1*DG3DP*G2*YS*G1
     1 -C1*G3*DG2DP*YS*G1-C1*G3*G2*DYSDP*G1-C1*G3*G2*YS*DG1DP
      DAZDP=G3*DZSDP+ZS*DG3DP-G3*DZQDP-ZQ*DG3DP-C2*DG3DP*G2*(ZS-C)*G1
     1 -C2*G3*DG2DP*(ZS-C)*G1-C2*G3*G2*DZSDP*G1-C2*G3*G2*(ZS-C)*DG1DP
C
C   DERIVATIVES OF POSITION OF A POINT ON SURFACE OF HYPERBOLOID
      DRXDR=COS(P)
      DRYDR=SIN(P)
      DRZDR=(-0.5)*A*SQRT((A**2-C**2)/(A**2-C**2-RS**2))*
     1 ((-2.0*RS)/(A**2-C**2))
      DRXDP = -RS*SIN(P)
      DRYDP = RS*COS(P)
      DRZDP=0.0
```

APPENDIX C (cont.)

```
C
C    ELEMENTS OF EQUATION SOLVING FOR BETA1 AND BETA2
       E=DAXDR*DAXDR+DAYDR*DAYDR+DAZDR*DAZDR
       F=DAXDR*DAXDP+DAYDR*DAYDP+DAZDR*DAZDP
       G=DAXDP*DAXDP+DAYDP*DAYDP+DAZDP*DAZDP
       EE=DRXDR*DAXDR+DRYDR*DAYDR+DRZDR*DAZDR
       FF1=DRXDR*DAXDP+DRYDR*DAYDP+DRZDR*DAZDP
       FF2=DRXDP*DAXDR+DRYDP*DAYDR+DRZDP*DAZDR
       GG=DRXDP*DAXDP+DRYDP*DAYDP+DRZDP*DAZDP
C
       FA = E*G-F*F
       FB = E*GG- 2.0*F*FF1+G*EE
       FC = EE*GG-FF1*FF1
       DISCR = FB * FB - 4.0*FA*FC
       BETA1 = (-FB+SQRT(ABS(DISCR)))/(2.0*FA)
       BETA2 = (-FB-SQRT(ABS(DISCR)))/(2.0*FA)
C
C    COMPONENTS OF CAUSTIC POINT POSITION ON VIRTUAL RAYS
       QX1=XS + BETA1*AX
       QY1=YS + BETA1*AY
       QZ1=ZS + BETA1*AZ
       QX2=XS + BETA2*AX
       QY2=YS + BETA2*AY
       QZ2=ZS + BETA2*AZ
C    POSITION OF CAUSTIC POINTS Q1 AND Q2
       RQ1=SQRT(QX1**2+QY1**2+QZ1**2)
       RQ2=SQRT(QX2**2+QY2**2+QZ2**2)
C    PHI COORDINATES OF Q1 AND Q2
       PRQ1=ATANF(QY1/QX1)
       PRQ2=ATANF(QY2/QX2)
C    THETA COORDINATES OF Q1 AND Q2
       X = (SQRT(QX1**2+QY1**2)/(RQ1))
       ASINX = ATANF(X/SQRT(1.0-X*X))
       TRQ1 = ASINX
       Y = SQRT(QX2**2+QY2**2)/(RQ1)
       ASINY = ATANF(Y/SQRT(1.0-Y*Y))
       TRQ2 = ASINY
C
C    SEE FIGURE C-1 FOR DESCRIPTION OF FOLLOWING ANGLES
       ANORM = ATANF(XNORM/ZNORM)*(180.0/3.14159)
       AINC = ATANF((XS-XQ)/(ZQ-ZS))*(180.0/3.14159)
       AREFL=ATANF(AX/AZ)*(180.0/3.14159)
       AORIGN = ATANF(RS/ZS)*(180.0/3.14159)
       ANGINC=AINC+ANORM
       ANGREF=AREFL-ANORM
C
C    COORDINATE TRANSFORMATION TO UNTILTED COORDINATE SYSTEM
       FPT = 2.56893
       ALPHA = (2.06)*(3.14159/180.0)
       XX= FPT * SIN(ALPHA)
       ZZ= FPT * (1.0 - COS(ALPHA))
       XP1 = QX1 * COS(ALPHA) - QZ1 * SIN(ALPHA) + XX
       YP1 = QY1
       ZP1 = QX1 * SIN(ALPHA) + QZ1 * COS(ALPHA) + ZZ
       XP2 = QX2 * COS(ALPHA) - QZ2 * SIN(ALPHA) + XX
       YP2 = QY2
       ZP2 = QX2 * SIN(ALPHA) + QZ2 * COS(ALPHA) + ZZ
```

APPENDIX C (cont.)

```
C
C    COMPUTATION OF GEOMETRICAL OPTICS PHASE
       QS=RSQ
       RHO = SQRT((XS*XS)+(YS*YS)+(ZS*ZS))
       T1 = ATANF(AX/AZ)
       T1DEG = T1*(180.0/3.14159)
       T2DEG = T1DEG
       T3 = ATANF(XS/ZS)
       PHDEG = (QS-RHO*COS(T1-T3))*(360.0/0.131)
       PHDEGP = PHDEG - 52500.0
C
C    COMPUTATION OF GEOMETRICAL OPTICS FIELD AND WEIGHTING SEE FIGURE C-2
       XT=0.0
       ZT= 2.56893
       THETA2=ATANF((XQ-XT)/(ZQ-ZT))
       THETA3=ATANF((XQ-XS)/(ZQ-ZS))
       THETA1 = THETA2-THETA3
C    ANS = FEED FUNCTION
       XXX = SIN(THETA1)
       YYY = 13.375*XXX
       ZZZ = SIN(YYY)*COS(YYY)
       VVV = (1.0-72.48*XXX*XXX)*YYY
       ANS = ZZZ/VVV
       ER = ANS/QS
       PP = 4.35
       EP = ER * (1.0/PP)*SQRTF(BETA1*BETA2)
       WT = EP * 100.0
C
       PRINT 100,XS,YS,ZS,AX,AY,AZ,AXS,AYS,AZS
  100  FORMAT (5X,9F10.5)
       PRINT 200,ANORM,AINC,AREFL,AORIGN,ANGINC,ANGREF
  200  FORMAT (5X,6F10.5)
       PRINT 300, BETA1, BETA2, QX1, QY1, QZ1, QX2, QY2, QZ2
  300  FORMAT (5X,8F10.5)
       PRINT 400,RQ1,RQ2,PRQ1,PRQ2,TRQ1,TRQ2,RRS
  400  FORMAT (5X, 7F10.5)
       PRINT 500, E, F, G, EE, FF1, FF2, GG
  500  FORMAT(5X,7F10.5)
       PRINT 600, DISCR
  600  FORMAT(5X,E13.6)
       PRINT 700, XP1, YP1, ZP1, XP2, YP2, ZP2
  700  FORMAT(5X,6F10.5)
       PRINT 800,RS,T2DEG,PHDEGP,WT,PHI
  800  FORMAT (5X,5F20.5)
       PRINT 900, ER,EP
  900  FORMAT (5X,2F20.5)
       PRINT 925, FA, FB, FC
  925  FORMAT (5X,3F13.6)
       PRINT 950, T2DEG,PHDEGP,WT
  950  FORMAT (5X,3F10.5,///)
C
       RS = RS + 0.067
       IF(RS-3.9)10,10,20
   20  STOP
       END
```

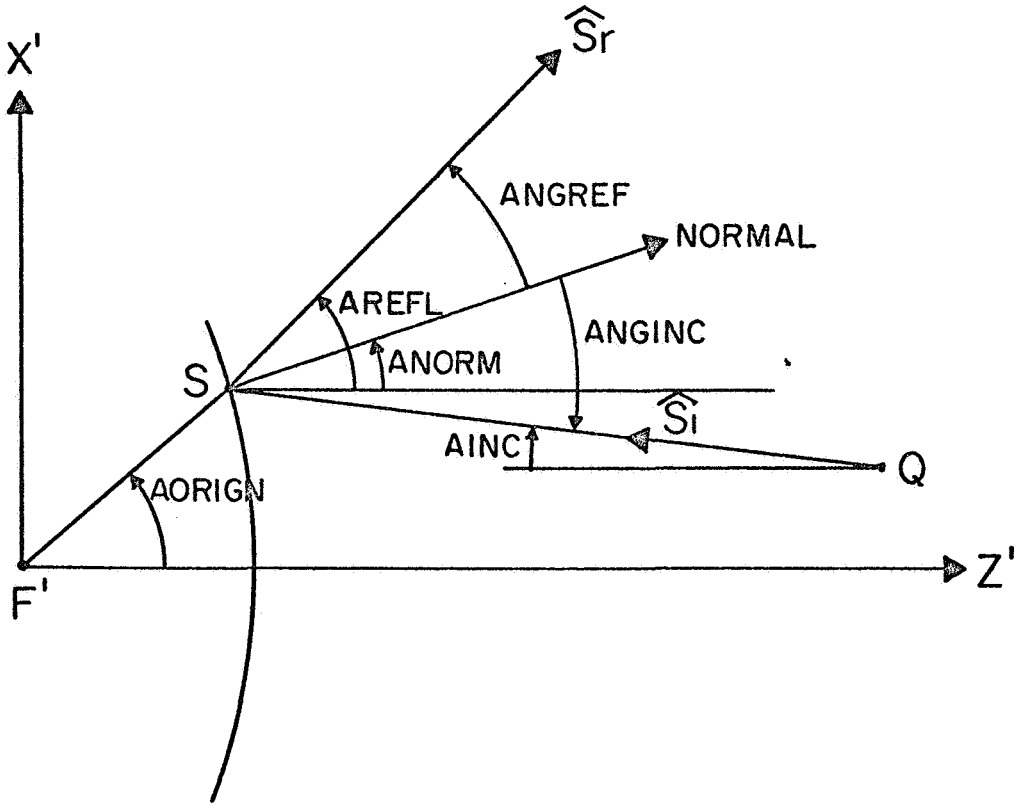

Figure C-1

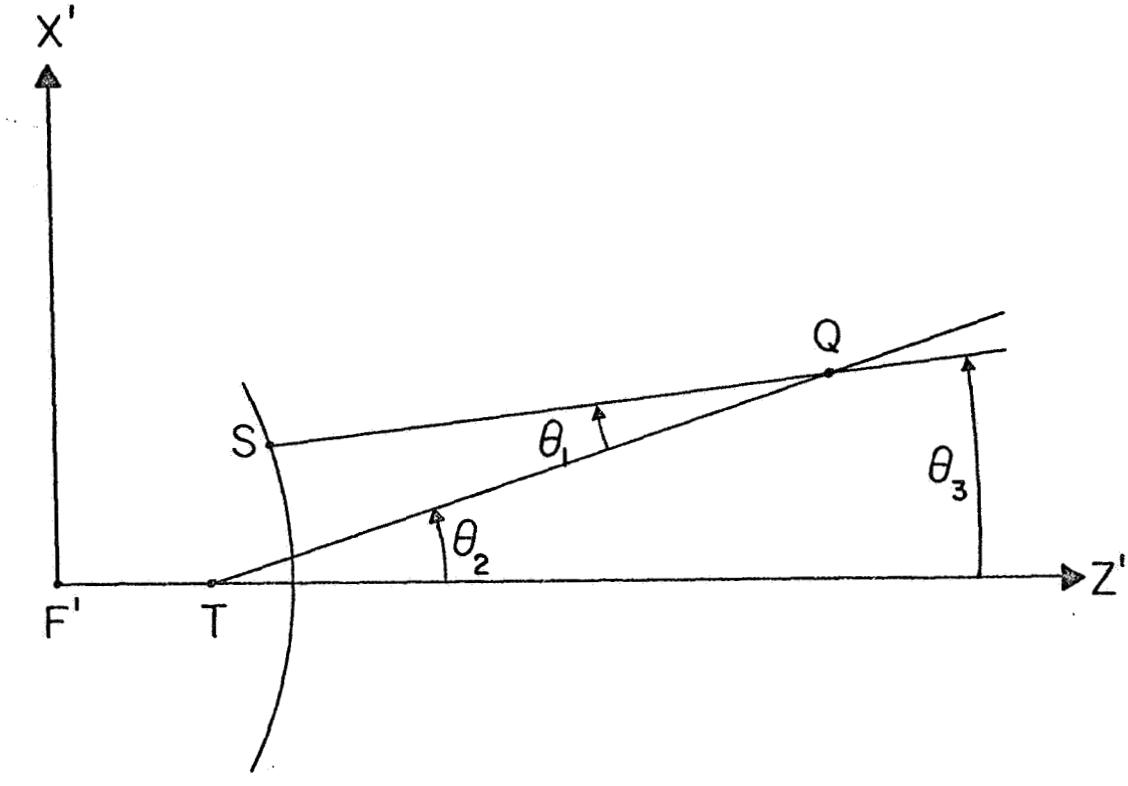

Figure C-2